ISAS - INTERNATIONAL SCHOOL FOR ADVANCED STUDIES

High Energy Processes in Seyfert Galaxies

by

Francesco Haardt

Thesis submitted for the degree of "Doctor Philosophiæ"

Astrophysics Sector

SUPERVISOR

Prof. Aldo Treves

October 1994

SISSA - SCUOLA INTERNAZIONALE SUPERIORE DI STUDI AVANZATI
TRIESTE
Strada Costiera 11

TRIESTE

a Oscar

"And my ties are severed clean,
The less I have the more I gain.
Off the beaten path I reign.
Rover wanderer nomad vagabond,
Call me what you will.
But I'll take my time anywhere,
I'm free to speak my mind anywhere,
And I'll take my find anywhere.
Anywhere I roam,
Where I lay my head is home.
Carved upon my stone:
My body lie but still I roam."

- James Hetfield -

"I have just come back from the land beyond the mountains.
There's a man with wounds I did see.
Said: I do not want to escape from reality,
I want reality to escape from me."

- Tom Rapp -

"Vedo gente, faccio cose."

- A girl in a Moretti's movie -

Abstract

In this thesis the problem of the origin of the X–rays in radio quiet Active Galactic Nuclei (AGNs) is discussed. The possible connection with Galactic Black Holes (GBHs) is also pointed out. In Chapter 1 the main observational constraints are reviewed and a contribution to the popular unified scheme for Seyfert galaxies is presented in. I show that the presence of a molecular torus embedding the active nucleus can mimic the reflection features expected from an accretion disk. In Chapter 2 a technique to solve the Comptonization problem is developed and an iterative solution of the kinetic equation is given. In Chapter 3 the *microphysics* of the X–ray source is discussed. I discuss the physics of thermal $e^{\pm}$ pair plasmas, introducing a "quasi–thermal" model for the plasma clouds responsible of the emission of the high energy radiation in AGNs and GBHs. Chapter 4 is devoted to model the *macrophysics* of the X–ray source. The formation of the high energy spectrum is also discussed in the framework of a "two phase model", exploring the possibility that the X–ray corona is formed by many active flaring events. The "blobby disk" is found to be an attractive scenario in explaining the high energy emission from AGNs and GBHs.

Acknowledgments

In the last three years I have been living for different periods in four towns scattered in three different countries in two continents. In each place very special persons helped and supported me in many ways and, more important, they still do it.

Trieste: my deep thanks are due to Aldo Treves, my supervisor, for constant encouragement, stimulating discussions, moral (and financial) support in many occasions. I wish also to thank Dennis Sciama, head of the Astrophysical sector of SISSA, always ready to help me whenever I need. I am also in debt with him for having addressed recently my attention to a (for me) new exciting field of research (which is not the topic of this thesis).

Milano: I am delighted to thank Laura Maraschi for putting me on my way to research, for teaching me most of the things I know about AGNs and for constant support. I am deeply in debt with Gabriele Ghisellini (actually in Torino), a kind of scientist every graduate should meet and a kind of friend.

Leicester: I would like to thank Chris Done for patiently struggling with my English and my laziness, and Giorgio Matt (once in Cambridge and now in Roma), another disillusioned AC Milan fan.

Baltimore: Piero Madau is a real good tutor, and a real friend. A common "taste for the paradox" made me enjoy well beyond the working hours the time spent there.

I also thank the Astrophysical Sector of the University of Milano, the X-ray group in Leicester, the Observatory of Torino and the USB branch of STScI for hospitality, facilities (and money).

Finally, during the last three years lot of friends shared with me good time, fun and love. The list is long and boring, so thanks, you know who you are! Nevertheless a

mention is deserved by the following guys: Chus for table always laid for three, Ba for loving the alien, Enzino for long cold winters, Jackson for being the way he want to be, Jeanga for sharing the weight, and Paolina for nicotine, lagers and flat tires.

I send my love to my family, Alessandra and little Gabriele.

Table of Contents

1. **Facts & the Big Picture** 7

1.1 Introduction 7

1.2 Spectral features 8

1.2.1 Seyfert 1 8

1.2.2 QSOs 11

1.2.3 Seyfert 2 12

1.3 X–ray variability 13

1.3.1 Seyfert 1 13

1.3.2 Seyfert 2 15

1.4 AGNs and GBHs 16

1.5 The Big Picture 17

1.6 Disk and/or torus reprocessing? 19

1.6.1 Motivation 19

1.6.2 Shape of the primary continuum 20

1.6.3 Torus reflection in Seyfert 1 spectra 24

1.6.4 Seyfert 2 spectra 31

1.6.5 Seyfert 2 and the XRB 36

2. **Comptonization in 1–D** 37

2.1 Basic equations of Compton scattering 37

2.2 Comptonization 38

2.3 Iterative solution: formal method 39

2.4 Iterative solution: relevant formulae 42

2.4.1 Isotropic kernel of single scattering 42
2.4.2 Radiation transfer in spherical geometry 44
2.4.3 Radiation transfer in plane parallel geometry 47
2.5 Anisotropic IC emission 49
2.5.1 Anisotropy coefficients 50
2.5.2 Anisotropic first scattering distribution 51
2.6 Numerical computations 52

3. Physics of Thermal Pair Plasmas 56
3.1 Introduction 56
3.2 Physical processes in compact sources 58
3.2.1 Cooling processes 58
3.2.2 Pair balance 60
3.3 Thermal Comptonization and pair production 62
3.3.1 Solution of the equations 62
3.3.2 Mapping 66
3.3.3 Comparison with observations 69
3.4 Quasi–thermal plasmas 72
3.4.1 Thermal vs non–thermal Comptonized spectra 72
3.4.2 Quasi–thermal pair cascade 74

4. Two Phase Models 84
4.1 Introduction 84
4.2 X–rays from extended coronae 85
4.2.1 Model outline 85
4.2.2 Solution of the balance equations 88
4.2.3 Main results 94
4.3 An example: Cygnus X–1 95

4.3.1 Cygnus X–1 in brief 95
4.3.2 Reflection features in GBHs 96
4.3.3 The model 97
4.3.4 Result of model fits 98
4.3.5 The γ–ray spectrum 101
4.3.6 Conclusion 103
4.4 X–rays from flaring coronae 105
4.4.1 Structured corona: phenomenology 107
4.4.2 Estimate of the form factor 108
4.4.3 Structured corona: a simple model 113
4.4.4 Number and luminosity of active loops 115
4.4.5 Reprocessed radiation 117
4.4.6 Time averaged Comptonized spectrum 118
4.4.7 Correlated variability 121

Conclusion 125

References 127

Chapter 1

Facts & the Big Picture

"THE REST IS SILENCE." – W.SHAKESPEARE

1.1 Introduction

Typical AGNs are known to emit the bulk of their electromagnetic energy across a broad spectral range covering seven decades in photon energy, from the far ifrared to the hard X-rays. The origin of the enormous luminosity observed in AGNs is not completely understood. In the so far more common scenario (we could call it "the" paradigm) the AGN phenomenon is due to matter accretion onto a supermassive black hole lying at the center of an otherwise normal host galaxy. One of the defining characteristic of the AGN phenomenon is the intense X–ray emission. In addition, the X–ray emission usually shows the most rapid variability in any of the frequency ranges which indicates that the X–ray production region is small, possibly very near to the central black hole. This alone can explain the crucial role played by X–ray spectroscopy, imaging and timing observations in our attempt in understanding the AGN phenomenon.

Far to be unique, classification within the AGN family reflects on one hand the great variety of features involved, on the other hand the lack of a global, well defined and solid model for the whole phenomenon. However the most basic possible distinction between radio loud (blazars, BL Lacs, OVV) and radio quiet objects (Seyfert 1 and 2 galaxies, QSO) beside being extremely useful, is probably physically meaningful. Two recent findings concerning the high energy radiation properties of AGNs set strong

constraints on any plausible model for the high energy radiation production in these objects. Discovery of breaks or cut–offs in the soft γ–ray spectra of Seyfert galaxies, and discovery of huge emission of hard γ–rays from blazars indeed indicate that radio quiet objects and radio loud objects are definitely two separated classes also in the high energy domain, and that different high energy radiation processes are taking place in their active core. In turn this would suggest that a genuine difference holds in the central power station of these two classes of objects.

In the following, I will concentrate on the high energy emission from radio quiet objects only, and the term AGN will be used to indicate this class of objects. It is worthwhile noting that, as pointed out by Svensson (1994) in a recent review, radio quiet objects can be referred as $\gamma-$ ray weak AGNs, as well as radio loud objects can be referred as $\gamma-$ ray loud AGNs. The present dissertation concerns *the high energy emission from γ–ray weak AGNs.*

In this first Chapter I discuss the main features observed in the X–ray spectra of AGNs which *do not* depend on a specific model for the generation of the primary X–rays. Thus for the moment we can think the X–ray continuum as produced by some unspecified mechanism. Having this in mind, first I review the main results of high energy (and some UV) observations of AGNs, following in part the recent review by Mushotzky et al. (1993). After a brief discussion comparing the high energy emission of AGNs and Galactic black holes, the so called Big Picture of the inner region of Seyfert galaxies and QSOs is outlined. Finally I discuss an original contribution to the Big Picture (Ghisellini et al. 1994) alternative in some aspects to the common view.

1.2 Spectral features

1.2.1 Seyfert 1

The 2–20 keV spectrum. Over the 2–20 keV range Seyfert 1 galaxy simple fits give power law spectra with energy index narrowly distributed around the average value $\alpha_x \simeq 0.7$ (Mushotzky 1984; Halpern 1982; Turner & Pounds 1989; Awaki et al. 1991; Nandra 1991; Nandra & Pounds 1994, hereafter NP94). In a recent analysis of 60 spectra of 27 Seyfert 1, NP94 find $\alpha_x = 0.73 \pm 0.05$, pointing out that the fits with a single power law are in general *statistically unacceptable.* The excess of χ^2 mainly arises because of both line and continuum features in the 2–20 keV emission. GINGA observations (Pounds et al. 1989, 1990; Matsuoka et al. 1990; Awaki et al. 1991; Nandra et al. 1991) have shown that fluorescence of cold iron resulting in an emission line at ~ 6.4 keV is common in Seyfert 1 spectra. The equivalent width of the Fe line in the sample of NP94 is found to be EW$= 140 \pm 20$ eV when the continuum is fitted with a single power law. The mean energy of the line is 6.37 ± 0.07, consistent with fluorescence of cold iron, and inconsistent with emission from thermally ionized iron. The iron line is in general quite broad, $\sigma \sim 0.7$ keV. Seyfert 1.5 NGC 4151, one of the most studied object, is an exception to the above general picture, as no broad iron line has been detected so far. A narrow component (FWHM < 7500 km/sec) has been observed by BBXRT (Weaver et al. 1992).

As mentioned above, other significant deviations from a power law exist in many spectra of Seyfert 1. Pounds et al. (1990) found that in the coadded spectrum of 12 Seyfert 1 observed with GINGA there was a decrement between 7–8 keV, and a flattening of the spectrum for energies above 10 keV. In IC4329A the flattening above 10 keV has been observed by Piro et al. (1990). The features at 7–8 keV has been interpreted (e.g. NP94) as absorption from a partially ionized medium in the line of sight, while the flattening above 10 keV is consistent with reprocessing of the X–rays by cold material out of the line of sight subtending a substantial solid angle at the X–ray source. Lightman & White (1988) and Guilbert & Rees (1988) pointed out that *reflection* of X–rays by an extended cold medium would result in a broad reflected spectrum peaking around 30 keV. Photons below 10 keV are effectively destroyed by

bound–free absorption, while photons above 100 keV are downscattered because of electron recoil. True absorption by iron ions also gives rise to a pseudo–absorption edge, that can account for part of the observed decrement around 7–8 keV. NP94 find that good fits to the observations are obtained if the cold material subtends a solid angle $\Omega/2\pi = 1$ at the X–ray source. Moreover, they point out that a second source of absorption (this must be in the line of sight) is required by the data.

One has to consider that data are also consistent with partial covering of the X–ray source by cold, dense material in the line of sight (Matsuoka et al. 1990, Piro et al. 1990). In this model all the observed distortions in the X–ray spectra are due to *transmission* of (part) of the X–rays through cold matter. In any case the inclusion of the features due to X–ray reprocessing, whatever the physical model is, has important consequences, the main being the revision of the mean spectral index of the 2–20 keV X–ray spectrum. In fact, when the effects of reflection and ionizing absorption (or of partial covering) are accounted for, the underlying mean X–ray continuum slope is found to be $\alpha_x = 0.95$ with a small but significant dispersion.

Finally it must be considered that during the writing of this thesis, the ASCA satellite is collecting data in the 1–10 keV range with a spectral resolution much better than any previous flying experiment.

The soft $\gamma-$ray spectrum. Recently, the OSSE instrument on the Compton Gamma Ray Observatory has detected several Seyfert galaxies above 60 keV (Cameron et al. 1993). If fitted with a power law, the derived energy spectral index is steep, with an average value of $\alpha_x = 1.7$, but the observations are also consistent with an exponential cut–off with e–folding energy around 50–200 keV (e.g., Madejski et al. 1994). The spectra resemble those from GBH observed by OSSE and SIGMA which show a thermal cutoff at high ($\sim$50–100 keV) energies (see, e.g., Sunyaev et al. 1991). Electron–positron annihilation lines have not been detected so far.

The spectrum below 2 keV. Emission below 2 keV exceeding that expected from a simple

power law occurs in ~ 30 % of all hard X-ray selected AGNs (Turner & Pounds 1989). The so called soft excess is typically modelled with a black body with temperature ~ 150 eV (Urry et al. 1989), although a steep power law (energy index > 2) or a free–free emission spectrum ($kT \sim 500$ eV) can fit the data as well. Recent ROSAT observations (Turner et al. 1993) have revealed the presence of line features in the soft X–ray spectra of several Seyfert galaxies.

The origin of the soft excess is not clear. The main pending question is whether the excess is or is not the high energy continuation of the UV bump observed in Seyferts and QSOs, which is usually interpreted as emission from the accretion disk. Walter & Fink (1993) analyzed ROSAT and IUE spectra of 58 Seyfert 1, and found a correlation of the soft X–ray slopes with the ratio between the UV flux and the flux at 2 keV. They use this correlation to support the picture in which the soft excess is the high frequency tail of the UV bump. On the other hand, recently Czerny & Zycki (1994) analyzed a sample of Seyfert 1 concluding that there is no need for an ultraviolet–to–soft X–ray bump as proposed by Walter & Fink (1993). Czerny & Zycki (1994) finds that the soft X–ray spectra of their sample are consistent with the hypothesis that the soft X–rays are due to reprocessing of the hard X–rays by partially ionized material. Here we note that in the X–ray illumination picture previously discussed only 10–30 % of the X–ray luminosity is actually reflected, the remaining being deposited and possibly thermalized in the cold reflecting layers, eventually producing a broad thermal emission in the soft X–rays. Detailed calculations of X–ray illuminated atmospheres (Ross & Fabian 1992) indicate that the observed soft excess is consistent with the reflection/reprocessing scenario. As we will see later, further support to this picture comes from variability observations.

1.2.2 QSOs

The 2–20 keV spectrum. QSOs are believed to be the high luminosity counterpart of Seyfert 1, with X–ray luminosity typically $> 6 \times 10^{44}$ erg/sec. The 2–20 keV continuum

spectra from GINGA (Williams et al. 1992) and EXOSAT (Comastri et al. 1992, Lawson et al. 1992) show a power law shape with energy index α_x somewhat steeper than 1, partially consistent with the mean value of Seyfert X–ray spectral index. The spread around the mean value is wider than that observed in Seyfert galaxies. Detections of iron line features are not in general significant, apart 3C273 and 1E1821+653 (Turner et al. 1990, Kii et al. 1991). The $\sim$ 6.7 keV rest frame energy of the line in 1E1821+653 is not consistent with most of Seyfert 1 observations (Kii et al. 1992). As well as the iron line, the existence of a Compton reflection component is uncertain.

The soft excess. QSOs show a rise in the X–ray spectrum at low energies similar to the soft excess seen in Seyfert 1. A power law fit of the excess gives an index ranging from 2.7 to 4.2. A black body fit gives temperatures in the range 40–80 eV (Comastri et al. 1992).

1.2.3 Seyfert 2

The 3–20 keV spectrum. Seyfert 2 galaxies show a 3–20 keV spectrum similar to that of Seyfert 1, except for the different absorption by cold material. Very few Seyfert 1 show significant absorption above the Galactic value, while almost all the Seyfert 2 detected in X–rays show evidence of strong photoelectric absorption (Awaki et al. 1991). Present X–ray data of Seyfert 2 indicate absorbing column densities in the range 10^{22}–10^{24} cm^{-2}, and at least one object, NGC 1068, with $N_H \gtrsim 10^{25}$ cm^{-2} (e.g. Mulchaey et al. 1992). Note that in NGC 1068 is actually *the absence* of absorption that constrains in the unified model the column density to be very high.

Strong Fe K lines have been observed in most of the X–ray detected Seyfert 2, with equivalent widths up to 2 keV in the case of NGC 1068 (Koyama et al. 1989, Awaki et al. 1990, Marshall et al. 1992).

The 0.1–3 keV spectrum. The 0.1–3 kev spectrum of Seyfert 2 is clearly a different

component from the heavily absorbed 3–20 keV spectrum, as the large column density would completely hide any intrinsic low energy emission. In the extreme case of NGC 1068 the lack of absorption in the overall X–ray spectrum can be explained assuming that we are actually observing the scattered primary radiation, without any contribution of radiation transmitted through the torus. For less extreme Seyfert 2 the same argument is valid for the soft X–ray spectrum.

1.3 X–ray variability

1.3.1 Seyfert 1

Flux variability. X–ray flux variability is pretty common in Seyfert 1 galaxies. Large amplitude variations ($\delta F/F > 1$) on time scales of days have been observed since the ARIEL–V sky survey (Marshall et al. 1981), and have been confirmed by the EXOSAT observatory (McHardy 1988, Pounds & McHardy 1988, McHardy 1990). Shorter term variability of timescale of less of one day has been found by Grandi et al. (1992) in ~ 40 % of the AGN observed with EXOSAT. The short term variability is usually of small amplitude ($\delta F/F < 1$).

There are indications (Zamorani et al. 1984, Barr & Mushotzky 1986, McHardy 1988) that more luminous sources exhibit slower variability. This is supported by works by Wandel & Mushotzky (1986) and Padovani & Rafanelli (1988) who found a correlation between the two folding time scale (i.e. the timescale in which a source doubles or halves its luminosity in a given band) and dynamical estimates of the central black hole mass (i.e. measuring optical line velocities).

Fourier analysis revealed that most Seyfert 1 have a power spectrum with a mean slope of roughly -1.2 in the 2–10 keV range (McHardy 1988). No characteristic time scale has been found so far. However it is not clear if X–ray variability in Seyfert galaxies

is linear and truly stochastic. Recently Letho et al. (1992) claimed that some AGNs observed with EXOSAT show stochastic variability, but alternative methods of analysis appropriate for non stochastic variability (e.g. fractal analysis) have been pursued by e.g. McHardy & Czerny (1988).

Spectral variability. The common trend in 2–10 keV spectral variability is a softening of the spectrum with increasing intensity, i.e. the power law steepens as the source gets brighter (Halpern 1985, Branduardi–Rymont 1986, Morini 1986, Perola et al. 1986, Matsuoka et al. 1990, Nandra et al. 1990, Maraschi et al. 1990, Nandra et al. 1991, Yaqoob & Warwick 1991, Grandi et al. 1992, Kinieda et al. 1992, Fiore et al. 1992, Yaqoob et al. 1993, Grandi et al. 1994). The inclusion of the reflected component previously discussion casts doubts on the genuine variability of the intrinsic power law. For example, EXOSAT and GINGA observations of NGC 5548 show the photon index increasing with increasing hard X–ray flux if the data are modelled with a single power law. When reflection is accounted for, the same data can be explained by variations in the flux ratio of a constant power law and a Compton reflection hump (Nandra et al. 1991). Seyfert 1.5 NGC 4151 seems however to show real variations of the underlying continuum (Perola et al. 1986, Yaqoob & warwick 1991, Yaqoob et al. 1993), as no evidence of reflection component exists in the data (Maisack & Yaqoob 1991, Yaqoob & Warwick 1991, Yaqoob et al. 1993, Titarchuk & Mastichiadis 1994). In this source any variation of the spectrum has then to be ascribed to the primary X–rays.

Correlation with variability in the UV band. As seen before, the deviations observed in the 2–20 keV spectra of Seyfert 1 galaxies suggest that part of the primary X–rays are reprocessed by cold matter. Another argument in favour of reprocessing is the correlation on time scales of weeks of the UV and the X–rays observed in NGC 5548 and NGC 4151 (Perola et al. 1986, Clavel et al. 1992). This led to the suggestion that in these two sources the UV is due to reprocessing of the higher frequency radiation, which is consistent with the comparable luminosities in the two bands. However variations up

to 30% (Nandra et al. 1990) in the X–rays on time scales of hours are not accompanied by similar variations in the UV. Furthermore Perola et al. (1986) and Clavel et al. (1992) pointed out that the correlation between X–rays and UV breaks down for large UV fluxes. A recent IUE campaign with time resolution of 90 minutes and an HST monitoring of NGC 4151 seem to indicate that UV variations of few percent occur on the shortest time scales, while variations greater than 20–30 % occur on time scales of few days (Korista 1994, private communication). A further problem with a pure reprocessing scenario is the wide spread of the UV to X–ray luminosity ratio measured by Walter & Fink (1993) for a sample of 58 AGNs, the ratio ranging from 0.1 up to 10. The authors claimed that anisotropic inverse Compton emission (Ghisellini et al. 1990, Haardt 1993) together with geometrical effects due to different inclination can account for the measured UV to X–ray luminosity ratios. However, if the cut–off in the soft γ–ray spectrum is a property common to Seyfert galaxies as a class, the emitting particle temperature may not be high enough to produce substantial anisotropy in the X–ray spectrum. Pure inclinations effects are unlikely to reproduce the observations. This point will be discussed later in some detail.

1.3.2 Seyfert 2

X–ray variability of Seyfert 2 galaxies seem to be similar to that observed in type 1 objects, except for the fact that obscured objects vary more slowly for their dynamical mass than unobscured type 1 sources (Wandel & Mushotzky 1986). This is consistent to a systematic underestimate of the optical–UV luminosity in Seyfert 2 as implied by the unification scheme (Mulchaey 1992). Slow soft X–ray variability is observed in NGC 1068, consistent with the hypothesis that the soft X–rays are indeed scattered primary radiation (Monier & Halpern 1987). NGC 4549 has a similar frequency dependant variability pattern, the hard X–rays showing rapid variations while little if any variability is observed below 5 keV (Iwasawa et al. 1993).

1.4 AGNs and GBHs

The X–ray spectrum of GBHs is remarkably similar to that of AGNs, despite the 6 orders of magnitude difference in mass of the central object. Typical spectra are steep in the soft X–rays, flat in the hard X–rays, and show a clear cut-off above 100 keV. The range of the power law spectral slopes is fairly consistent with that observed for Seyfert 1, and evidence of Compton reflection have been found (Ebisawa 1991; Done et al. 1992; Ueda et al. 1994). X–ray flux variations as the low frequency noise observed in the power density spectrum of Cygnus X–1 seem to be consistent with a re-scaling of the mass with respect to the AGN power density spectra.

For the above reasons there is a general consensus that GBHs are basically powered by the same mechanism powering AGNs and that the primary X–rays have the same origin. However, although the similarity could hold for a region within 20 Schwarzschild radii of the black hole, it does not hold for larger scale structures, e.g. the broad and narrow line regions and the molecular torus. Furthermore, non–transient GBHs, as Cygnus X–1 tend to switch from a so called soft high state to a so called hard low state (the adjectives "low" and "high" are somewhat confusing as the integrated X–ray luminosity can be higher in the low state than that in the high state). The soft state usually shows a prominent thermal emission at $\sim$ 1 keV and a very weak power law in the hard X–rays. In the low state a single power law fits the spectra from 1 keV to 100 keV, where a cut–off is usually present (see, e.g., Grebenev et al. 1993).

Another class of GBHs, the transient sources (e.g. Nova Muscae), show (in the "on" state) an average spectral shape similar to the soft state of non transient sources, but with a much more luminous hard tail resembling the hard X–ray power law observed in the low state of non transient GBHs. In the "off" state X–rays are simply not radiated. A distinctive feature of GBHs is quasi periodic oscillations (QPOs). They have been observed in the power density spectra of GX 339–4 (period $\sim$ 0.8 Hz, Grebenev et al. 1993), Cygnus X–1 and Nova Persei ($\sim$ 0.04 Hz and $\sim$ 0.035 – 0.28 Hz respectively,

Vikhlinin et al. 1992; Kouveliotu et al. 1992) and Nova Muscae ($\sim$ 10 Hz, Grebenev et al. 1992; Tanaka et al. 1991). No one of the above behaviors has a clear counterpart in the X–ray light curves of Seyfert galaxies.

1.5 The Big Picture

Based on the observational results outlined above, in the last ten years a general picture of the central region of radio quiet AGNs has been developed. A main contribution is the unified model for Seyfert 1 and Seyfert 2 (see Antonucci 1993 for a detailed description). This model assumes that the different properties of the two classes are simply due to an inclination effect (e.g. Lawrence & Elvis 1982; Antonucci & Miller 1985; Krolik & Begelman 1988; see also Antonucci 1993 for a review). Thus in the unified model there are no differences in the production mechanism of the primary X–rays in Seyfert 1 and Seyfert 2, as the two classes have the same intrinsic high energy continuum. In this model, a geometrically and optically thick torus is supposed to surround the active nucleus absorbing its optical/UV and soft X–ray radiation, including the broad emission lines. If the inclination of the system is such that the nucleus is hidden to us by the torus, the source is classified as Seyfert 2, otherwise as Seyfert 1.

Several observations support the idea of inclination being the main discriminating parameter: the presence of broad lines in the polarized light of Seyfert 2 (Antonucci & Miller 1985; Miller & Goodrich 1990; Tran et al. 1992), which is explained as due to the scattering into the line of sight of the hidden Seyfert 1 nucleus radiation by warm material outside the absorbing torus; the anisotropic continuum emission implied by the ionization cones (e.g. Pogge 1989; Tadhunter & Tsvetanov 1989; Haniff et al. 1991); the energy and photon budget in the ionization cones (e.g. Wilson 1992); the large Seyfert 2 X–ray column densities (e.g. Awaki et al. 1991; Mulchaey, Mushotzky & Weaver 1992; NP94).

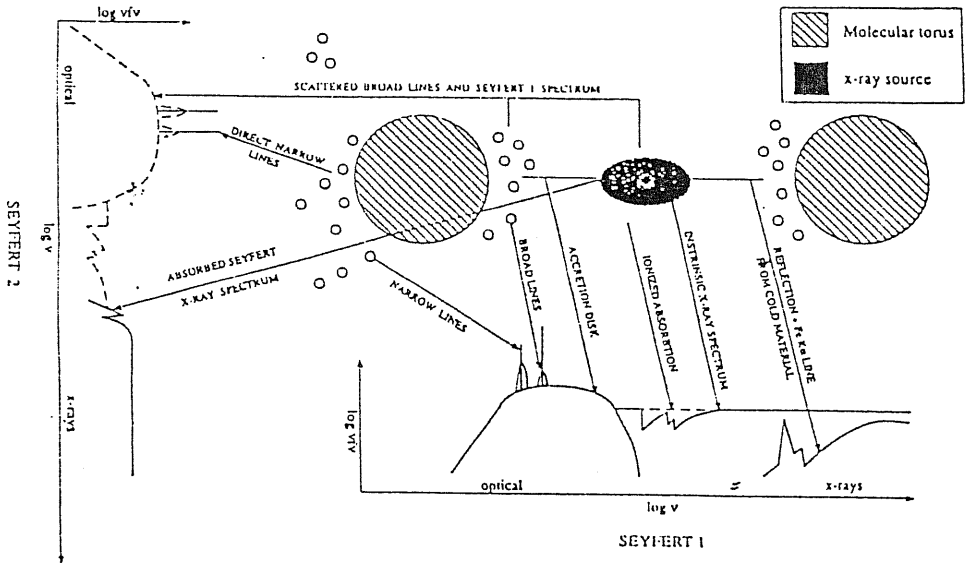

Fig. 1: The Big Picture. The X–ray source is close to the central black hole, and illuminates an optically thick accretion disk giving rise to reflection features. Further out are the broad line clouds, and further out still is the molecular torus, and outside that are the narrow line clouds. The funnel of the torus is filled with ionized material. If the X–ray source is observed directly through the funnel the source is classified as a Seyfert 1; if the line of sight intercept the torus, as a Seyfert 2 (from Mushotzky et al. 1993).

Having in mind the unified scheme depicted above we can now sketch the presently favoured model of the inner region of a Seyfert galaxy (Fig. 1). A massive black hole ($M = 10^{6 \div 7} M_{\odot}$; 2 order of magnitude more for a QSO) lies at the center of the active nucleus. The unspecified primary high energy continuum is originated within 20 Schwarzschild radii of the black hole. Accreting matter forms in the innermost part a Keplerian or quasi–Keplerian optically thick accretion disk. The infalling matter emits UV radiation, and is responsible of the Compton reflection component, as well as of

the cold iron line at 6.4 keV. At several light days (in case of a Seyfert galaxy) are the broad line clouds. Further out is the molecular torus obscuring the line of sight to the central black hole in Seyfert 2, and accounting for the high column density in the X–rays observed in these objects. At scales of several hundreds parsecs lies the narrow line region, from which optical and UV narrow lines generate. Finally the whole "machine" is thought to be immersed in an electron scattering cloud responsible for the reflected component observed in the Seyfert 2 continuum.

1.6 Disk and/or torus reprocessing?

1.6.1 Motivation

As we have seen, the main effect of the molecular torus is to absorb the soft X–ray primary radiation in Seyfert 2 spectra. We have also seen that the torus may be optically thick to Thomson scattering. As a consequence, there is the need for a detailed model of the contribution that the torus can give to the spectrum of Seyfert 1 by scattering part of the incident primary radiation into the line of sight. This radiation could in principle mimic the reflection bump observed in the majority of Seyfert 1 (NP94 and references therein), which is interpreted in the Big Picture as due to reflection from the accretion disk (Lightman & White 1988; George & Fabian 1991; Matt et al. 1991, hereafter MPP).

If the torus is Compton thick, Seyfert 2 should be dimmer than Seyfert 1 even at high X–ray energies, because most of the high energies photons are Compton downscattered, and can eventually be absorbed or emerge at lower energies, possibly out of the line of sight. This of course bears important consequences for the detectability of Seyfert 2 by OSSE. At very large energies, the decline of the Klein–Nishina cross section allows an increasing fraction of primary photons to pass the torus unscattered. Not only the

total flux, but also the spectral shape will therefore be a function of the optical depth of the torus.

The present section is the result of a collaboration of myself with G. Ghisellini and G. Matt (Ghisellini et al. 1994). First Monte Carlo results on this subject have been presented by Awaki et al. (1991). Similar work on the subject has been done by Krolik et al. (1994), which independently confirmed some of our following results.

1.6.2 Shape of the primary continuum

In Fig. 2 I sketch the adopted geometry: the primary X–ray source is located close to a (cold) accretion disk, and is assumed to emit a spectrum

$$F(E) \propto E^{-\alpha_x} \exp(-E/E_c). \tag{1.1}$$

This spectral form has been chosen accordingly to SIGMA and OSSE observations of Seyfert 1 (e.g. Jourdain et al. 1992; Maisack et al. 1993; Cameron et al. 1993; Zdziarski et al. 1994). We have used an e–folding energy $E_c = 100$ keV, according to the typical OSSE best–fit results. The index α_x is taken to be 0.9, consistent with the observations of Seyfert 1 below 20 keV (Pounds et al. 1990; Matsuoka et al. 1990; NP94). It is worth noting that the inclusion of the cutoff in the primary spectrum has a negligible effect on the fluorescent iron line intensity (see §[1.6.3]), as the photons effective in producing the line emission are those with energy less than ~50 keV.

We assumed an isotropic primary X–ray. About half of its radiation impinges onto the accretion disk, where it is partly reflected by Compton scattering and fluorescence emission (Lightman & White 1988; George & Fabian 1991; MPP). The shape of the Compton reflection continuum has been calculated following the prescriptions of White, Lightman & Zdziarski (1988) and Lightman & White (1988). The two–stream approximation adopted by these authors allows only to compute the reflected component integrated over the emission angles. Unfortunately, the actual angular behaviour

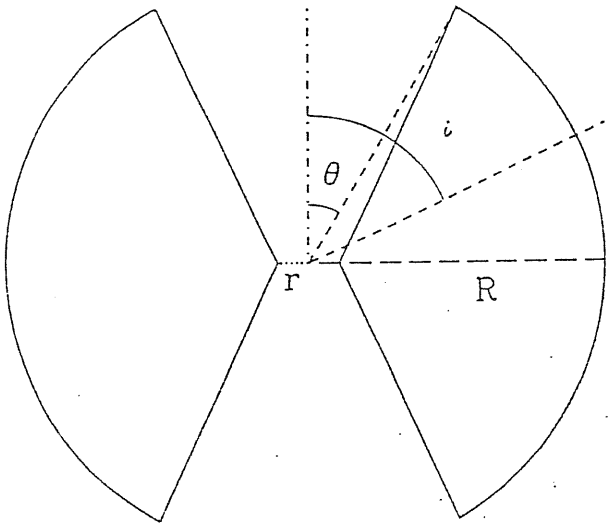

Fig. 2: The geometry assumed for our computations. The source of primary X-ray radiation is located at the center of an obscuring torus with column density N_H along the equatorial plane. This source is assumed isotropic. A cold accretion disk (not shown in the figure) is assumed to intercept half of the primary X-rays and to contribute to the primary spectrum by Compton reflection. The angular dependence of this component is given by eq[1.1]. The torus semiaperture angle is θ, and the viewing angle is i. We always used $r/R = 0.1$ in our calculations (from Ghisellini et al. 1994).

of the Compton hump is complex, and it is a function of the photon energy (George & Fabian 1991; MPP). Only when the scattering can be treated as elastic an analytical estimation can be made. For simplicity, we have used the two–stream approximation results for the shape, multiplied by an angular function to normalize the spectrum at different viewing angles. In such a way, the shape of the Compton reflection spectrum we adopted is of course independent of the emission angle. For $E > 20$ keV this is a

crude approximation, but sufficient for our scope.

In order to compute the angular function, I define as μ' the absolute value of the cosine of the angle of the incident photon with the normal, and μ the cosine of the angle of reflection. With this choice both the cosines are positive. Along the path within the slab the differential absorption probability is

$$dP_{abs} = \mathrm{e}^{-\tau} d\tau, \tag{1.2}$$

where τ is the optical depth for the considered process. Now assume that a photon absorbed in τ is re–emitted along a new direction defined by μ. The integral probability that it can reach the surface of the slab is then

$$p_{esc} = \mathrm{e}^{-\frac{\mu'}{\mu}\tau}. \tag{1.3}$$

Now the total escape probability for photons absorbed along the path defined by μ' and re–emitted in direction μ is

$$P_{esc}(\mu, \mu') = \int_0^\infty dP_{abs}\, p_{esc} = \frac{\mu}{\mu + \mu'}. \tag{1.4}$$

Now assume that the incident flux has an angular distribution given by $F_i(\mu')$. The total escaping flux in direction μ is

$$F_{out}(\mu) = \int_0^1 d\mu'\, F_{in}(\mu') P_{esc}(\mu, \mu') \frac{1}{2\pi} \int_{\omega_m}^{\omega_M} d\omega \frac{d\sigma}{d\omega} K(\mu, \mu', \omega) \tag{1.5}$$

where

$$\omega_m = \mu\mu' - \sqrt{1-\mu^2}\,\sqrt{1-\mu'^2} \tag{1.6}$$

$$\omega_M = \mu\mu' + \sqrt{1-\mu^2}\,\sqrt{1-\mu'^2} \tag{1.7}$$

$$K(\mu, \mu', \omega) = 2(1 - \mu^2 - \mu'^2 + 2\mu\mu'\omega - \omega^2)^{-1/2}. \tag{1.8}$$

Here the integration variable ω is the cosine of the angle of reflection computed with respect to the incident direction. The differential cross section of the process is $d\sigma/d\omega$. The second integral in eq[1.5] takes into account the change of reference frame.

Note that

$$\int_{\omega_m}^{\omega_M} d\omega\, K(\mu,\mu',\omega) = 2\pi. \tag{1.9}$$

Two simple processes can be easily computed: true absorption and re–emission (e.g., the iron line emission), and elastic scattering (e.g., the Compton reflection hump below 20 keV).

In the case of real absorption and re–emission, from

$$\frac{d\sigma}{d\omega} = 1$$

using $F_{in}d\mu = d\mu$ we obtain from eq[1.5]

$$F_{out}(\mu) = 2\mu \ln(1 + 1/\mu). \tag{1.10}$$

In the case of scattering with Rayleigh phase function from

$$\frac{d\sigma}{d\omega} = \frac{3}{4}(1+\omega^2)$$

eq[1.5] gives

$$F_{out}(\mu) = \frac{3\mu}{4}\left[(3 - 2\mu^2 + 3\mu^4)\ln\left(1+\frac{1}{\mu}\right) + (3\mu^2 - 1)\left(\frac{1}{2} - \mu\right)\right], \tag{1.11}$$

From now on, I call 'nuclear' the spectrum resulting from the sum of the primary isotropic X–ray source (emitting the spectrum of eq[1.1]) and the reflected component from the disk. For simplicity we have not included in the latter component the iron line produced by the disk. A fraction of the line emitted by the disk can be reflected by the funnel of the torus; we have evaluated that this effect enhances the EW by no more than about 10 per cent at small inclination angles.

The equatorial plane of the torus has been assumed to be equal to that of the accretion disk. R the distance between the primary source (coincident with the geometrical center of the system) and the outer walls of the torus, and r the distance between the center and the inner wall of the torus in the equatorial plane. We always used $r/R = 0.1$. The half opening angle of the torus, θ, is defined as shown in Fig. 2.

I indicate with N_H the column densities measured in the equatorial plane ($i = 90°$). At a given inclination angle $i > \theta$, the column density along the line of sight is

$$N_H(i) = \frac{1 - k(i)\, r/R}{1 - r/R}\, N_H \tag{1.12}$$

where

$$k(i) = \frac{\cos\theta}{(r/R - \sin\theta)\cos i + \cos\theta \sin i} \tag{1.13}$$

We have assumed interstellar abundances as in Morrison & McCammon (1983). Further details of the adopted atomic data as well as the radiative transfer treatment can be found in MPP and in Ghisellini et al. (1994).

1.6.3 Torus reflection in Seyfert 1 spectra

Continuum. In Fig. 3 I show the spectra calculated for different N_H at the viewing angle $i = 0° - 18°$, i.e. smaller than the torus opening angle.

In this case we see directly the Seyfert 1 nucleus plus the contribution from the radiation scattered by the torus into the line of sight. The warm scattering material may further complicate the spectrum by absorbing and scattering the incident radiation out of the line of sight. Indeed, absorption by warm material seems now to be a common feature in Seyfert 1 (see NP94 and references therein). Hereafter WSM indicates the warm scattering material, and WSC the corresponding scattered continuum. The spectral signature of the WSM for small viewing angles has been qualitatively described by Krolik & Kallman (1987).

For $N_H \ll 10^{24}$ cm^{-2}, the radiation passing through the torus either escapes or is absorbed, while the scattering is negligible ($\tau \ll 1$, where here τ is the electron scattering optical depth) and therefore the torus does not contribute significantly to the spectrum. Instead, for $N_H \gtrsim 10^{24}$ cm^{-2}, when the scattering optical depth is of order unity or greater, an important fraction of the hard X–rays is Compton scattered and reflected by the funnel of the torus, while softer photons are photoabsorbed (Compton

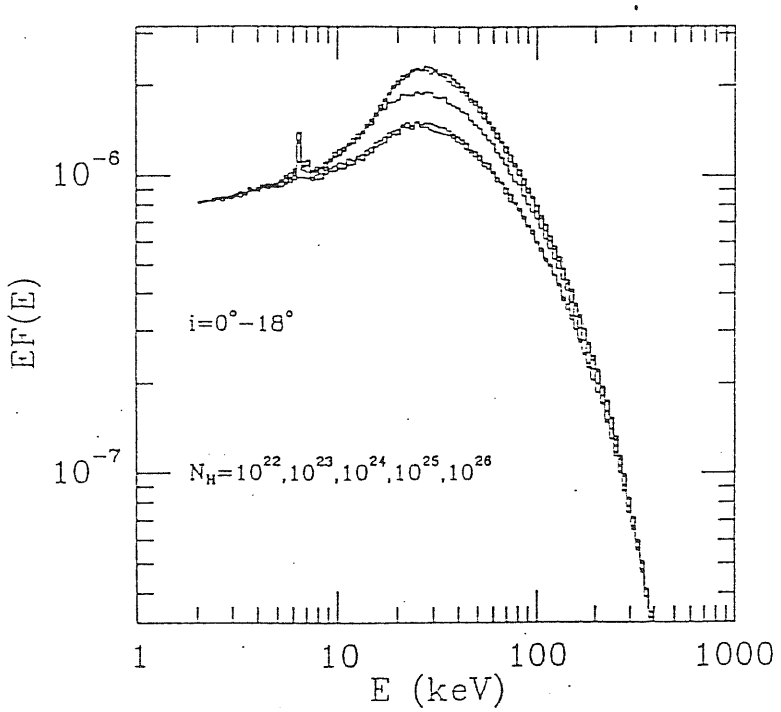

Fig. 3: Spectra computed with different values of N_H (increasing from bottom to top) for an inclination angle 0°–18°. The assumed torus semi-aperture angle is $\theta = 30°$ (from Ghisellini et al. 1994).

scattering and photoabsorption cross section are equal at about 10 keV for neutral matter). Note that the Klein–Nishina decline of the scattering cross section can make the torus optically thin for photons with the highest energies. Increasing N_H there is an increasing contribution, mainly at 10–50 keV, from the funnel, which saturates when the optical depth becomes much larger than unity. Therefore the spectra in Fig. 3 for $N_H \gtrsim 10^{25}$ cm^{-2} overlap.

Note that the spectral shape of the scattered radiation is very similar to that produced by a flat disk, as in both cases the shape is mainly dictated by the atomic processes. With one major difference: here photons can scatter more than once onto the surface of the funnel, when $\tau \gtrsim 1$ (see MPP for a discussion of this effect in geometrically

thick accretion disks). At 30 keV, the relative contribution of the torus to the flux is 29 and 55 per cent for $N_H = 10^{24}$ and 10^{25} cm^{-2}, respectively.

These results have the important consequence to introduce an energy–dependent variability. In the soft X–rays we see only the compact illuminating source, and a rapid variability is expected. At larger ($\gtrsim$ 10 keV) energies and for large column densities the flux from the compact source is diluted by radiation coming from the torus, with a much larger emitting area. Hence the latter fraction of the flux varies with a longer time–scale. Therefore both the amplitude and the time–scale of variability should be frequency dependent, with softer energies being more violently variable. As a consequence, the spectral shape should also vary, pivoting around 20–30 keV.

Of course, similar energy–dependent variability is expected from reflection off an accretion disk. However, in this case the bulk of the reprocessed radiation is expected to come from the inner 50-100 gravitational radii (MPP). So the variability time–scale should be of order hours–days, while the variability time–scale of the radiation from the torus should be of order months–years (the location of the inner surface of the torus is very poorly determined; the constraint that the torus must be located outside the Broad Line Region and inside the Narrow Line Region permits to range between a few light–months and several light–years). Therefore, variability measurements are fundamental in determining the relative amount of reprocessed radiation from the two regions.

Iron fluorescent line.

In Fig. 4 I show the equivalent width of the iron fluorescent line emitted by the torus vs N_H for two values of the half-opening angle ($\theta = 30°$, left hand panel, and $\theta = 45°$, right hand panel) and for three different angular bins (0°–18°, filled squares, 60°–63°, open circles, 81°–84°, crosses).

The results for small viewing angles indicate that the line EW is very small for $N_H \lesssim 10^{23}$ cm^{-2}, but increases to about 70-90 eV for $N_H \gtrsim 5 \times 10^{23}$ cm^{-2}. For very thick tori ($N_H \gtrsim 5 \times 10^{25}$ cm^{-2}), the equivalent width is greater for the 45° case because

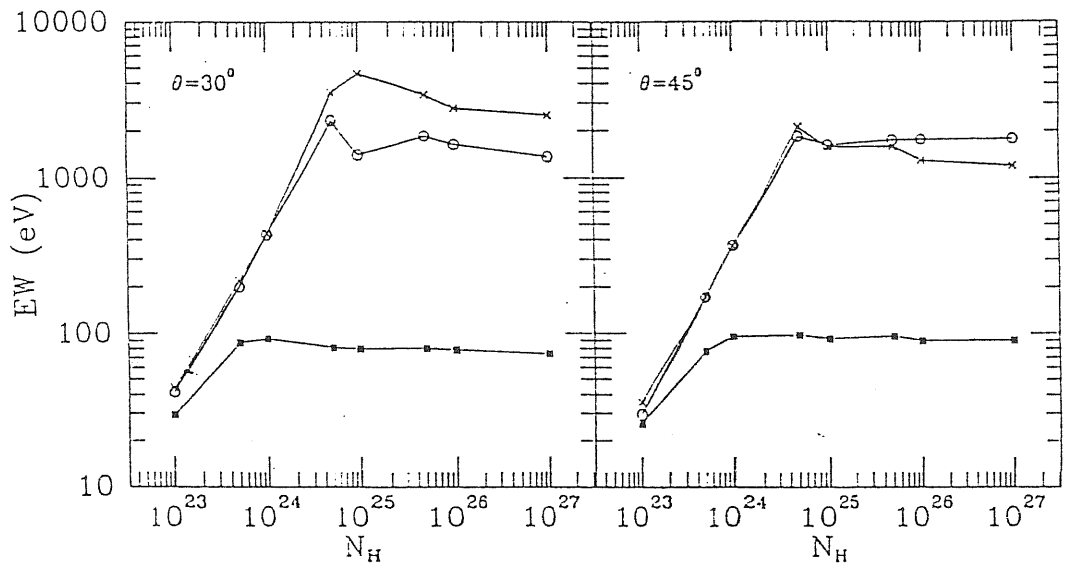

Fig. 4: The equivalent width of the fluorescence iron line produced by the torus as a function of N_H for two values of the half-opening angle ($\theta = 30°$, left hand panel, and $\theta = 45°$, right hand panel), and for three different angular bins ($0°-18°$, filled squares, $60°-63°$, open circles, and $81°-84°$, crosses)(from Ghisellini et al. 1994).

the smaller solid angle subtended by the torus is overcompensated by a greater projected area (see MPP for a detailed discussion of this effect). The question which naturally arises is if this component alone can account for the observed iron lines in Seyfert 1. The mean equivalent width for the sample studied by NP94 (27 sources, mainly Seyfert 1 but including 7 Narrow Emission Line Galaxies, hereafter NELGs) is about 110 eV (fits with the reflection component included; the average EW is 140 eV fitting the continuum with a single power law), but much greater and much lower values are also present. Assuming a dispersion in the iron abundance and its mean value somewhat greater than the solar, the observed results can be explained by the emission from the torus, provided that the

average column density is $\gtrsim 10^{24}$ cm^{-2}.

On the other hand, the observed iron line properties are also in good agreement with the accretion disk reflection hypothesis (e.g. Matt et al. 1992; NP94). The EW is about 150 eV for a face–on disk, and smaller for greater viewing angles (see eq. 3), to give an angle–averaged (between 0° and 90°) value of ~110 eV. If the unification scheme is correct, the range of visible angles appropriate for Seyfert 1 is limited by the aperture of the torus, and the predicted mean value of the EW is consequently larger than the observed 110 eV; but the presence of a few NELGs in the sample and a possible slight iron underabundance could maybe explain the discrepancy. If the torus is Compton thick, however, it contributes significantly to the iron line, bringing the total average EW to about 250 eV, much greater than observed. This argues in favour of small ($N_H \lesssim 10^{23}$ cm^{-2}) column densities, in disagreement with the estimation based on the X–ray background (XRB; but in agreement with observations of an UV–selected sample, Mulchaey et al. 1992). This apparent contradiction can in principle be solved in many ways, for instance by assuming that the iron abundance is smaller than the solar in both the accretion disk and the torus, or that the contribution of one or both the components is reduced in some way (for instance by an anisotropic primary X–ray emission which privileges the small inclinations, or a very sharp inner surface of the torus with consequently small projected area).

All these solutions appear rather unsatisfactory, leading to the suggestion that if the accretion disk emits (exists ?) the torus must be Compton thin (or to not exist at all) while if the torus is Compton thick the disk contribution must be small or absent. Variability and/or high energy resolution measurements are required to solve this problem, as the line emitted by the torus is narrow while that emitted by the disk should be broad and with a well–defined profile due to relativistic effects (e.g. Fabian et al. 1989; Matt et al. 1992; Matt et al. 1993 for a Schwarzschild black hole, and Laor 1991; Kojima 1991 for a Kerr black hole), and should vary with a much smaller time–scale.

While the ultimate solution of this problem seems demanded to the kind of observations just outlined, a deeper look inside the NP94 sample could give some first indications. The line of sight column density of the 7 NELGs is between 4×10^{21} and 10^{23} cm^{-2}, greater than that in our own galaxy, and greater than the mean value of the Seyfert 1 in the sample (which is another confirmation of the unification scheme). The values are not particularly high, but this is not surprising as the sample has been chosen on the basis of the X–ray brightness. With these column densities the predicted EW from the torus is very small at all inclination angles (see Fig. 4), while the observed EWs in these sources range between 70 and 440 eV. The error bars are too large to allow a more detailed analysis; nevertheless, it seems quite clear that another source of iron line photons besides the torus does exist in these objects.

To end this discussion on the iron line emission, it must be recalled that iron fluorescence (or recombination) photons can be emitted by the WSM outside the torus. However, this component, which can dominate the line emission for X–ray absorbed sources, is not very important at small viewing angles, when the nuclear radiation is directly seen. For opening angles such as those considered here, the EW is in fact at most a few tens of eV (Krolik & Kallman 1987).

Summary of main results. As we have seen, 2–D Montecarlo simulations of radiative transfer indicate that the torus may produce observable feature in Seyfert 1 spectra. For small viewing angles, when the observer sees directly the nucleus, the equivalent width of the iron line emitted by the torus is very small for $N_H \lesssim 10^{23}$ cm^{-2} and of order of 70-90 eV for $N_H \gtrsim 5\times10^{23}$ cm^{-2}. The accretion disk can also emit a fluorescent line, with EW up to about 150 eV for a face–on disk (e.g. Matt et al. 1992). A comparison with the observed values (NP94) suggests that the two contributions can hardly be present simultaneously; the presence of the accretion disk requires a Compton thin torus, while if the torus is Compton thick, the accretion disk (if present) can not contribute significantly. The results for the seven NELGs included in the Nandra &

Pounds sample strongly suggest that a line emitting region besides the torus does exist. Anyway, the two contributions can in principle be distinguished by their width (the line emitted by the torus must be much narrower than that emitted by the disk) and by their variability time–scales (that of the disk emission being much smaller than the one of the torus emission). GINGA measurements of the line width are inconclusive (Nandra & Pounds 1993), but much firmer constraints should be put by forthcoming ASCA measurements. With regard to the variability, it is worth noting that the recent discovery that the claimed periodicity in the X–ray emission of NGC 6814 is actually due to a galactic source in the field of view (Madjeski et al. 1993) implies that the most compelling reason to locate the line emitting matter very close to the black hole (Kunieda et al. 1990) is now probably gone away. Nevertheless, it is worth noting that at least another, even if less spectacular, evidence for short time–scales of the reprocessed radiation does exist (NGC 4051, Fiore et al. 1992).

In summary we have found that

1) At small inclination angles Compton thick tori can significantly contribute to the emission at 10–50 keV, resembling the Compton reflection hump produced by cold accretion disks in the vicinity of the primary X–ray source.

2) The torus, for small inclination angles and for $N_H \gtrsim 10^{24}$ cm^{-2}, can produce an iron $K\alpha$ line with EW of $\sim$ 90 keV, not much smaller than the average value observed in Seyfert galaxies. This indicates that a thick torus alone can produce the observed EWs, but in this case the iron line from the disk must be dimmed in some way. Otherwise the torus must be in general Compton thin.

3) The presence of the torus and the WSM introduces a complex pattern for the predicted variability, which can be used to estimate the relative strength of the different components. For $N_H \gtrsim 10^{24}$ cm^{-2}, the soft X–rays of Seyfert 1 should vary more rapidly than the hard X–rays. The spectrum should pivot around 20–30 keV.

1.6.4 Seyfert 2 spectra

As the predicted effects of the molecular torus seem to cause some problem to the standard unified scheme when compared to Seyfert 1 observations, this has been regarded as the main topic of our analysis. Nevertheless it is also interesting to compare simulations with data also in the case of Seyfert 2 objects. Here I present our main results on this subject. For a complete analysis and discussion including computations of the expected polarization in the X–ray spectrum the reader should refer to the published paper (Ghisellini et al. 1994).

Continuum. In Fig. 5 I show the spectra, for different column densities, corresponding to the viewing angle $i = 60° - 63°$, for a half-opening angle of the torus $\theta = 30°$.

Below 10 keV, the spectra are the sum of two components: 1) the radiation transmitted through the torus, and 2) the radiation reflected by that part of the torus inner surface which is directly visible by the observer. For $N_H \lesssim 10^{24}$ cm^{-2} the transmitted component dominates, as indicated by the exponential shape of the spectrum. Viceversa, the reflected component, with a corresponding power law spectrum, dominates for $N_H \gtrsim 10^{26}$ cm^{-2}, when the torus is optically thick to both photoabsorption and scattering; the amount of reflected component depends only on the inclination angle. For intermediate values of the column density the reflected part dominates at energies up to a few keV, while the transmitted part dominates at higher energies; their ratio depends on i.

At high ($\gtrsim$ 20 keV) energies, the spectra for $N_H \lesssim 10^{23}$ cm^{-2} are practically not modified, while for $N_H \gtrsim 10^{24}$ cm^{-2} even hard X–rays are scattered away from the line of sight and softened by Compton recoil.

At energies greater than about 50 keV the Klein–Nishina decline begins to be important, lowering the optical depth. The spectra (above 20 keV) of the radiation passing through the torus without any scattering are shown in Fig. 6 as dashed lines, for $N_H = 10^{24}$ and 10^{25} cm^{-2}. These has been calculated by simply multiplying the

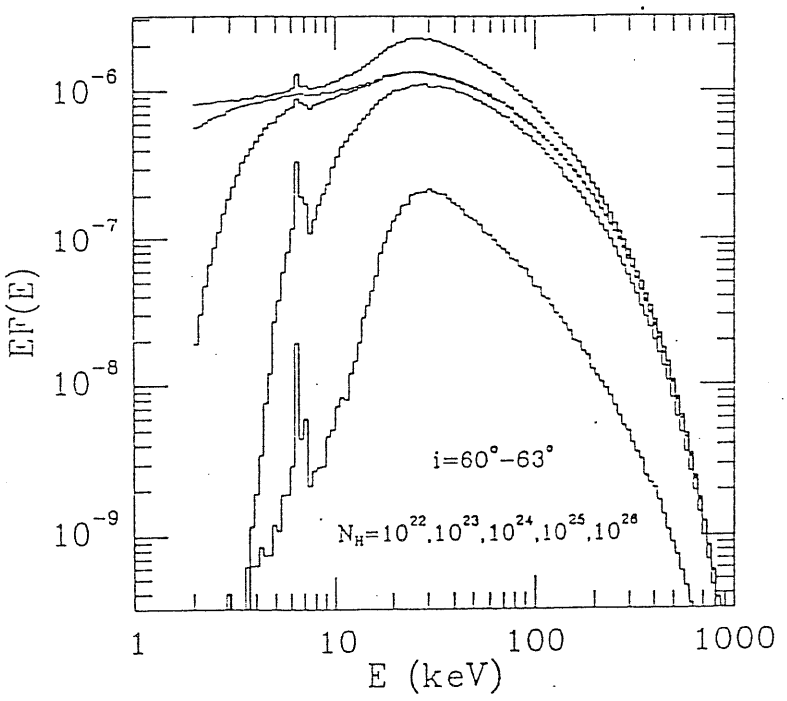

Fig. 5: Spectra computed with different values of N_H (increasing from top to bottom) for an inclination angle 60°–63°. The assumed torus half-opening angle is $\theta = 30°$ (from Ghisellini et al. 1994).

nuclear radiation with the factor $\exp[-\tau(i)\sigma_{KN}(\nu)/\sigma_T]$ where σ_T and $\sigma_{KN}(\nu)$ are the Thomson and Klein–Nishina cross sections, respectively. For $i = 60°$ and $\theta = 30°$ the Thomson optical depths are $\tau(60°) = 0.62$ and 6.2, respectively (eq.[1.12]). We can see that if the torus is moderately thick ($\tau \sim 1$), the unscattered flux can be a substantial fraction of the total, being (for $N_H = 10^{24}$ cm^{-2}) the ~50 per cent between 20 and 50 keV, and more at higher energies, where the scattering cross section is smaller. In the case of $N_H = 10^{25}$ cm^{-2} the main contribution to the total flux comes from (down-)scattered photons up to 400 keV, beyond which the unscattered radiation dominates.

In Fig. 5 the spectra are shown without any contribution from the WSM. If present, this material would intercept the nuclear radiation emitted at small inclination angles:

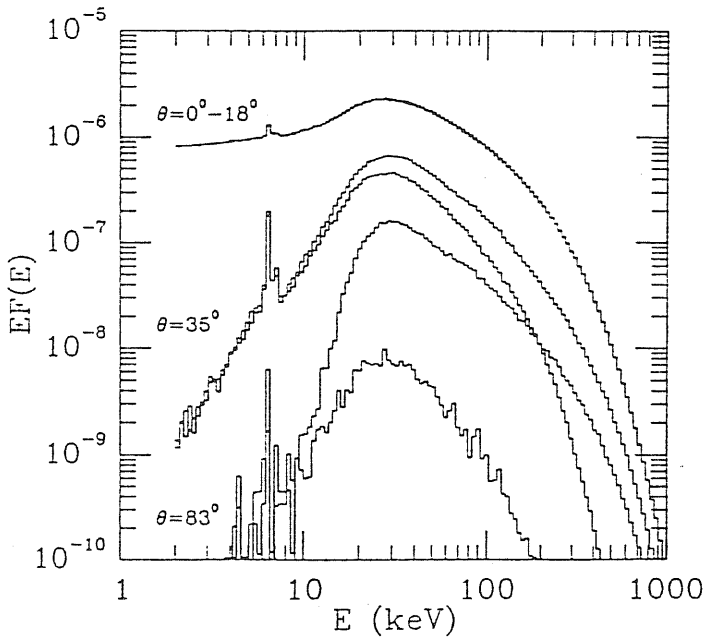

Fig. 6: The upper (overlapping) histograms are the spectra observed at $i = 0°$-$18°$ *for* $N_H = 10^{25}$ *and* $N_H = 10^{26}$ cm^{-2}. *The other histograms are the spectra viewed at* $i = 32°$-$37°$ *and* $81°$-$84°$, *for the same column densities (increasing from top to bottom), appropriate for the Sey 2 galaxy NGC 1068. A fraction f of the upper curves can dilute the shown radiation emerging from the torus at large inclinations. Note that the amount of dilution, f, necessary to hide the rising spectrum and to produce an iron line EW of 1 keV depends on the inclination (from Ghisellini et al. 1994).*

the continuous lines in Fig. 6 take into account this contribution by adding the 0.5 per cent of the radiation emitted along the axis of the torus (consisting of the nuclear component plus the contribution from the torus itself, as shown in Fig. 3). The spectra shown in Fig. 6 refer to the cases with $N_H = 10^{24}$, 10^{25} and 10^{26} cm^{-2}. For lower values of the column density the WSC is unimportant at all energies. The opening angle of the torus and the inclination are the same as Fig. 5.

The WSC can be the only observable one at energies less than a few keV when

$N_H \gtrsim 10^{24}$ cm^{-2}, because the photons impinging onto the torus are photoabsorbed. There is marginal evidence for this in recent ROSAT observations. Mulchaey et al. (1993) find that the continuum shapes of Seyfert 2 below the photoelectric cutoff are identical to those of Seyfert 1. For larger column densities the WSC becomes important also at higher energies, diluting the radiation emerging from the torus. For $N_H \gtrsim 10^{25}$ cm^{-2}, the relative importance of the WSC dilution depends on the portion of the funnel that is visible at a given inclination angle, and therefore on the inclination angle itself.

The sum of different contributions results in a complex variability pattern.

1) For $N_H \lesssim 10^{23}$ cm^{-2}, at all energies photons which are scattered by both the WSM medium and the torus should give a negligible contribution to the total flux. Consequently, the variability is simply that of the nuclear source at all frequencies.
2) For $N_H \sim 10^{24}$ cm^{-2} the dominant contribution to the total flux above 20 keV comes from unscattered photons, while below 10 keV the WSM can dilute the observed continuum. Therefore in this case hard X–rays should vary more rapidly than the soft X–rays, and with a larger amplitude. This is just the opposite behaviour than at small viewing angles.
3) For $N_H \gtrsim 10^{25}$ cm^{-2} the flux is always dominated by scattered photons, either by the WSM (at low energies) or by the surface of the funnel (at high energies). The flux should therefore be steady at all but the highest frequencies, where the decreased scattering cross section allows photons to pass the torus unscattered.

Iron fluorescent line. In Fig. 4 the EW of the iron line produced by the torus is shown vs the column density for two inclination angles greater than the half–opening angle, namely 60°–63° and 81°–84°. As the nuclear radiation is now intercepted by the torus, the equivalent width can be very large (more than 1 keV), provided that the column density is $\gtrsim 10^{24}$ cm^{-2}.

As discussed above for the continuum, the total torus emission is composed by the line photons emitted by the visible part of the inner surface of the torus and those

escaping from its outer surface. The EW of the two components is different: that of the transmitted component is the greatest for $N_H \gtrsim$ a few $\times 10^{24}$ cm^{-2}. Both the equivalent widths (but not the luminosities) are almost independent of the inclination angle. Therefore, for intermediate column densities ($\sim 10^{24.5 \div 25}$ cm^{-2}) the total EW increases with i as the reflected/transmitted ratio diminishes for geometrical reasons. For lower (when the transmitted component dominates) and for greater (when the reflected component dominates) column densities the EW is almost independent of the inclination.

Of course, the EW shown in Fig. 4 can be reduced by dilution with the WSC. The WSM can also produce iron lines by fluorescence and/or recombination processes (Krolik & Kallman 1987) or by resonant scattering of the continuum (Band et al. 1990). These lines should have a total EW with respect to the WSC of order 1 keV, and their energies should be mainly around 6.7–6.9 keV.

The case of NGC 1068. An interesting result of our computations is that the torus can easily account for the cold iron line component observed in NGC 1068 (Marshall et al. 1993), provided that the column density in this source is of order 10^{25}–10^{26} cm^{-2}, as indeed suggested by GINGA and BBXRT observations (Koyama et al. 1989; Marshall et al. 1993; Smith et al. 1993). In fact the iron line in the transmitted spectra has equivalent widths of order a few keV, which can diminishes to the observed $\sim$ 1 keV after dilution with the scattered nuclear radiation.

Assuming for the optical depth of the WSM, τ_{sc}, values consistent with the observations of warm absorbers in Seyfert 1 (e.g. NP94), we are able to say that this source is probably seen at a viewing angle greater than $\sim 50°$, while an independent estimation of τ_{sc} based on an energy budget argument suggests $i \sim 55°$–$70°$. However, such range of inclinations is inconsistent with the value derived from the polarization degree of the broad lines, which is 35°, a value derived by assuming the simplest geometry and an optically thin case. Of course our evaluations are based on rather indirect evidence, and

i can be grossly overestimated.

1.6.5 Seyfert 2 and the XRB

The above results can have important consequences on recent models of the XRB, in which a significant contribution is made by heavily obscured Seyfert 2 galaxies, as firstly suggested by Setti & Woltjer (1989). In these models the column density of the torus required to fit the XRB is $\gtrsim 10^{24}$ cm^{-2} (Madau et al. 1993), or a distribution of values with a significant contribution from sources with $10^{24} \lesssim N_H \lesssim 10^{25}$ cm^{-2} (Matt & Fabian 1993).

These values are somewhat in excess of the constraints posed by our model and by the observations of the EW of the iron line in Seyfert galaxies, which indicate $N_H \lesssim 10^{23}$ cm^{-2}. However, this disagreement is probably not serious, and can be possibly reconciled by exploring a wider range of the space of parameters (Madau et al. 1994) and by considering possible selection effects in the present samples of Seyfert galaxies, which favours the closest Seyfert 1 and the least obscured (and therefore brightest) Seyfert 2.

Chapter 2

Comptonization in 1–D

"NOW YOU LOOK PRETTY COOL." – G.TATE

2.1 Basic equations of Compton scattering

The theory of Compton scattering is well established, and a complete discussion with astrophysical applications can be found for example in Pozdniakov et al. (1983). A basic reference for an overview of the topic in an astrophysical context is Rybicki & Lightman (1979). The complete theory of single Compton scattering can be found in Nagirner & Poutanen (1994).

I just recall that the momentum $\mathbf{x}' \equiv (h\nu'/c)\mathbf{\Omega}'$ of a photon scattered by an electron of momentum $\mathbf{p} \equiv \gamma m_e \mathbf{v}$ is changed into $\mathbf{x} \equiv (h\nu/c)\mathbf{\Omega}$ where

$$\frac{\nu}{\nu'} = \frac{1-\mu'\beta}{1-\mu+(h\nu'/\gamma m_e c^2)(1-\cos\alpha)} \tag{2.1}$$

Here $\beta \equiv v/c$, $v \equiv |\mathbf{v}|$, $\mu \equiv \mathbf{\Omega}\cdot\mathbf{v}/v$, $\mu' \equiv \mathbf{\Omega}'\cdot\mathbf{v}/v$, and the scattering angle $\alpha \equiv \cos^{-1}(\mathbf{\Omega}\cdot\mathbf{\Omega}')$. $\mathbf{\Omega}$ and $\mathbf{\Omega}'$ are unit vectors parallel to the photon momenta. All the other symbols have the standard meaning.

If the photon is scattered by an electron at rest, its frequency changes because of the recoil effect, and in general the electron gains energy. This is often referred as Direct Compton effect. Otherwise, if the electron is moving at high speed, the Doppler effect plays a dominant role, and the photon can gain energy. This effect is called Inverse Compton (IC). This is likely to be the main high energy photon production mechanism

in compact sources (see next Chapter 3).

The differential cross section of this process can be written as

$$\frac{d\sigma}{d\Omega} = \frac{3\sigma_T}{16\pi\gamma^2}\frac{W}{(1-\mu'\beta)^2}\left(\frac{\nu}{\nu'}\right)^2 \tag{2.2}$$

where

$$\begin{aligned} W &\equiv \frac{w}{w'} + \frac{w'}{w} + 2\left(\frac{1}{w'} - \frac{1}{w}\right) + \left(\frac{1}{w'} - \frac{1}{w}\right)^2 \\ w &\equiv \gamma x(1-\mu\beta) \\ w' &\equiv \gamma x'(1-\mu'\beta) \end{aligned} \tag{2.3}$$

Here $x \equiv h\nu/m_e c^2$ and $x' \equiv h\nu'/m_e c^2$.

The total cross section is expressed by the Klein-Nishina formula:

$$\sigma(w) = \frac{3\sigma_T}{8w}\left[\left(1 - \frac{2}{w} - \frac{2}{w^2}\right)\ln(1+2w) + \frac{1}{2} + \frac{4}{w} - \frac{1}{2(1+2w)^2}\right] \tag{2.4}$$

It is important to recall that the *effective* probability of scattering for a photon with a beam of electrons moving at speed v is proportional to

$$\sigma_{\rm eff}(w) \equiv (1-\mu\beta)\sigma(w) \tag{2.5}$$

2.2 Comptonization

The term *Comptonization* generally indicates a situation where multiple scatterings play a major role in forming the resulting radiation spectrum. The evolution of the photon occupation number in the phase space is described by the Boltzmann kinetic equation. The Boltzmann equation may be expanded to second order if the fractional energy transfer per scattering is small. This is the case for nonrelativistic electrons. If the electron distribution is thermal the resulting equation is known as *Kompaneets* equation:

$$\frac{\partial n}{\partial t_c} = \frac{\Theta}{x^2}\frac{\partial}{\partial x}[x^4(n' + n + n^2)] \tag{2.6}$$

where $n' \equiv \partial n/\partial \mathrm{x}$ and $\Theta \equiv kT_e/m_e c^2$. T_e is the electron temperature. The quantity $t_c \equiv (n_e \sigma_T c)t$ is the time in units of mean scattering time. Note that the mean scattering time is the light crossing time R/c divided by the scattering optical depth $\tau \equiv n_e \sigma_T R$ where R is the size of the scattering medium.

A solution to the Kompaneets equation has been obtained by Sunyaev & Titarchuk (1980) in the diffusion approximation. The resulting analytical solutions are valid for $\Theta \lesssim 0.1$, and for optical depth $\tau \gtrsim 3$. This solution is of great importance, as it provides an analytical description of Comptonization. As a result, the Sunyaev & Titarchuk model is widely used in fitting the high energy spectrum of galactic and extragalactic sources. However the problem of Comptonization in rarefied ($\tau < 1$) hot plasmas is of main interest in astrophysics. Mild-relativistic and relativistic IC scattering is thought to be responsible of the X–ray and γ–ray emission observed in GBHs and AGNs (see next Chapters 3 and 4). The lack of a suitable analytical formulation in these situations led to an intense use of numerical simulations (see e.g. Pozdniakov et al. 1983).

An analytical approach can be carried out solving the kinetic equation iteratively, i.e., computing the photon distribution within the medium after each scattering event. Appropriate boundary conditions are then used to evaluate the observed radiation spectrum. In a former paper (Haardt 1993), I considered the problem of anisotropic Comptonization in a plane parallel thermal plasma. A simple kernel was used, neglecting both electron recoil and "Klein–Nishina" effect on the cross section. In the present Chapter I show how the method can be modified considering the full relativistic kernel and different geometries.

2.3 Iterative solution: formal method

Let us consider an initial radiation field described by a specific photon density $I_0(x, \Omega, \mathrm{r})$, being r a point in an 3–D reference frame.

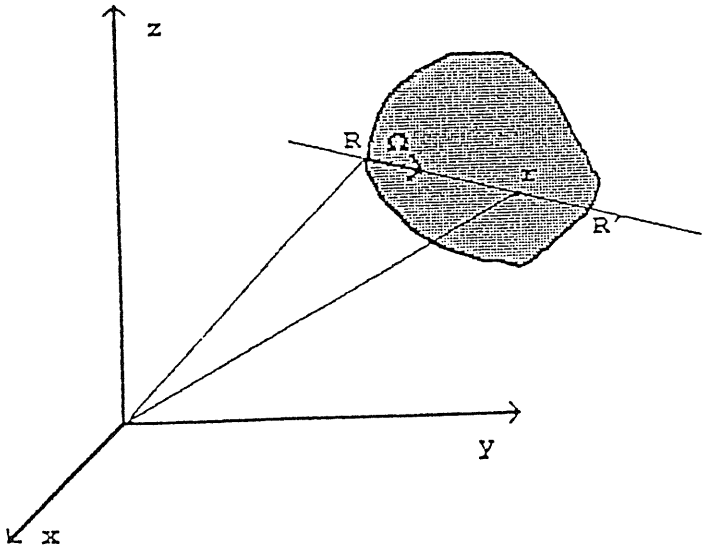

Fig. 1: Sketched geometry of a 3-D scattering cloud.

The specific photon density of photons of momentum $\mathbf{x} = (x, \mathbf{\Omega})$ that suffer a scattering in $\mathbf{r}$ is the sum of the contributions of point–like sources along the path defined by $\mathbf{\Omega}$, starting from the medium boundary $\mathbf{R}$ to $\mathbf{r}$ (see Fig. 1). We calculate the fraction of photons that change their momentum in r according to the scattering laws by means of the *kernel* $K(\mathbf{x}, \mathbf{x}') \equiv P[(x', \mathbf{\Omega}') \rightarrow (x, \mathbf{\Omega})]$ describing the probability that the photon momentum is changed from $\mathbf{x}'$ to $\mathbf{x}$ after the scattering event. Formally

$$I_1 = \mathcal{P}[\mathcal{V}(I_0)] \tag{2.7}$$

The operator $\mathcal{V}$ acts on the spatial coordinate as follows

$$\mathcal{V}(I) \equiv n_e \sigma(x) \int_0^{|\mathbf{r}-\mathbf{R}|} dl\, I(\mathbf{r} - l\mathbf{\Omega}) \mathrm{e}^{-n_e \sigma(x) l} \tag{2.8}$$

The operator $\mathcal{P}$ acts on the photon momentum coordinates as

$$\mathcal{P}(I) \equiv \int d\mathbf{x}'\, K(\mathbf{x},\mathbf{x}')\, I(\mathbf{x}') \tag{2.9}$$

The integral in the above equation is performed over space of photon momenta. The kernel depends also on the electron momentum, albeit not explicitly indicated. Now the argument can be repeated for any successive scattering, i.e.,

$$I_{k+1} = \mathcal{P}[\mathcal{V}(I_k)] \tag{2.10}$$

A great simplification arises assuming if one assumes that the scattering is isotropic *in the laboratory frame.* This is a realistic assumption if the electron momenta are randomly oriented and if the input photons do not have any preferential direction. We call this condition *complete isotropy.* In this case the kernel of single scattering depends only on the photon energies x, x'. Note that, even assuming an isotropic kernel, the observed spectrum *is not* in general independent from direction, as the opacity depends on direction, according to the geometry of the scattering medium. In the problems of interest here, the scattering electrons are generally assumed to have a randomly oriented.

Under the assumption of perfect isotropy, the radiation field evolves as eq[2.7]–[2.10], providing the operator $\mathcal{V}$ is averaged over angles, i.e.,

$$\mathcal{V}(I) \equiv \frac{n_e \sigma(x)}{4\pi} \int d\Omega \int_0^{|\mathbf{r}-\mathbf{R}|} dl\, I(\mathbf{r} - l\Omega) \mathrm{e}^{-n_e \sigma(x) l} \tag{2.11}$$

Now the operator $\mathcal{P}$ acts over the energy coordinates, i.e.

$$\mathcal{P}(I) \equiv \int dx'\, K(x,x')\, I(x') \tag{2.12}$$

The integration limits over the solid angle $d\Omega$ must be specified according to the particular geometry of the medium (see next §[2.4.2] and §[2.4.3]).

Now if we indicate with μ the cosine of the angle of a beam with the normal at the medium surface, the net flux escaping from the medium after k scatterings can be computed as

$$\pi F_k = 4\pi\, \mathcal{V}(\mu I_k) \tag{2.13}$$

where the functions I_k has to be evaluated at the boundary of the source.

It is interesting to consider the special case of Thomson scattering. When the cross section is indeed energy independent, the iterative solution can be carried out much more easily since in eq[2.10] the integral over the space coordinates can be separated from that over the energy. If the initial photon distribution has the factorized form $I_0(x,\mathbf{r}) = X_0(x)J_0(\mathbf{r})$, then the radiation field after $k+1$ scatterings is

$$I_{k+1} = \mathcal{P}(X_k)\,\mathcal{V}(J_k) \tag{2.14}$$

and the net flux escaping from the source at the surface is

$$\pi F_k = 4\pi\, X_k \mathcal{V}(\mu J_k) \tag{2.15}$$

2.4 Iterative solution: relevant formulae

2.4.1 Isotropic kernel of single scattering

The full relativistic kernel has been obtained by Jones (1968). Recently Coppi & Blandford (1990) gave the correct formula of the kernel, as some equations in the Jones paper appear incorrect. This can be written as

$$K(x,x',\gamma) = \int_{z_-}^{z_+} dz\, \frac{dP}{dz} \tag{2.16}$$

The differential reads

$$\begin{aligned}\frac{dP}{dz}(x,x',\gamma) =& \frac{3\sigma_T cx}{16\gamma^4 x'^2 R(x',\gamma)(1-\beta z)(\beta^2+\epsilon^2+2\beta\epsilon z)^{1/2}} \\ &\times \Big[\Big[2y_0k - ak^2 + (1+y_0^2 - 2ay_0k + a^2k^2)(a^2-b^2)^{-1/2} \\ &+ \frac{1}{k^2(1-\beta z)}\Big\{k^2 + k^2\frac{a(2b-a)}{(a-b)}(a^2-b^2)^{-1/2} \\ &+ (a^2-b^2)^{-3/2}[a(1-y_0)^2 + 2kb^2(1-y_0) - ba^2k^2]\Big\}\Big]\end{aligned} \tag{2.17}$$

where $\epsilon = x'/\gamma$, $k = \gamma/x$, $a = 1 - \beta z - (1 - y_0)/k$, $b = \delta/k$ and

$$\begin{aligned} y_0 &= \frac{(\epsilon + \beta z)(\rho + \epsilon\rho - 1 + \beta z)}{\rho(\beta^2 + \epsilon^2 + 2\beta\epsilon z)} \\ \delta &= \frac{\beta(1 - z^2)^{1/2}[\rho^2\beta^2 + 2\rho\epsilon(1 - \rho)(1 - \beta z) - (\rho - 1 + \beta z)^2]^{1/2}}{\rho(\beta^2 + \epsilon^2 + 2\beta\epsilon z)} \end{aligned} \tag{2.18}$$

with $\rho = x/x'$. The integration limits of eq[2.16] are

$$\begin{aligned} z_- &= \max[\![-1, \beta^{-1}\{1 - \rho[d + (d^2 - 1/\gamma^2)^{1/2}]\}]\!] \\ z_+ &= \max[\![+1, \beta^{-1}\{1 - \rho[d - (d^2 - 1/\gamma^2)^{1/2}]\}]\!] \end{aligned} \tag{2.19}$$

where $d = 1 + \epsilon - \epsilon\rho$.

The function R in eq[2.17] is the angle averaged scattering rate, i.e.,

$$\begin{aligned} R(x, \gamma) &\equiv c \int_{-1}^{+1} \frac{d\mu}{2} \sigma(\mu)(1 - \mu\beta) \\ &= \frac{3c\sigma_T}{16\gamma^2\beta x^2} \int_{\gamma x(1-\beta)}^{\gamma x(1+\beta)} dw \left[\left(1 - \frac{2}{w} - \frac{2}{w^2}\right) \ln(1 + 2w) + \frac{1}{2} + \frac{4}{w} - \frac{1}{2(1 + 2w)^2} \right] \end{aligned} \tag{2.20}$$

The kernel is normalized so as

$$\int_0^\infty dx K(x, x', \gamma) = 1 \tag{2.21}$$

The kernel takes a very simple form if one neglect the electron recoil, and if the Thomson approximation is valid in the electron rest frame, i.e., if $x \ll \min(\gamma - 1, 1/\gamma)$. As shown by Rybicki & Lightman (1979):

$$K(x, x', \gamma) = \frac{1}{4x'(\gamma^2 - 1)} \begin{cases} (1 + \beta)\rho - (1 - \beta) & \frac{1-\beta}{1+\beta} < \rho < 1 \\ (1 + \beta) - \rho(1 - \beta) & 1 < \rho < \frac{1+\beta}{1-\beta} \\ 0 & \text{otherwise} \end{cases}, \tag{2.22}$$

It may be easily checked that the kernel has the correct normalization as eq[2.21].

The average fractional energy gain is given by

$$\int_0^\infty dx(x - x')K(x, x', \gamma) = \frac{4}{3}(\gamma^2 - 1)x' \ . \tag{2.23}$$

The approximated eq[2.22] is obtained assuming an isotropic phase function for the scattering. The use of the more correct Rayleigh phase function gives negligible corrections.

In most of the interesting astrophysical situations the scattering electrons are unlikely to be monoenergetic. In this case the kernel needs to be averaged over the actual normalized electron distribution $N(\gamma)$, i.e.,

$$K(x,x') = \int_1^\infty d\gamma K(x,x',\gamma)N(\gamma) \ . \tag{2.24}$$

2.4.2 Radiation transfer in spherical geometry

Let us consider an homogeneous sphere of optical depth τ. Let assume an inner source of soft photons. If the soft photon source has rotational symmetry (e.g., an homogeneous source or a central point–like source) the Comptonized spectrum obviously does not depend on direction. This is the simpler case. In Fig. 2 I sketch the geometry of the problem. We need to compute the contribution from the whole sphere to the radiation field in the point P, lying at a distance R from the center of the sphere O. We first compute the contribution of the radiation field in P from a shell located at a distance r from the center O. This is the integral over all the possible angles ϑ between the ray path and the normal at the sphere surface in P. Second, we integrate over r from the center to the boundary of the sphere.

From Fig. 2 we can see that for any given ϑ there are two point sources (labelled as S_1 and S_2) along the ray path if $r < R$, and one point if $r > R$. I indicate with α the cosine of the angle of OA with OS_1 or OS_2 or OS_3, and with μ the cosine of the emission angle ϑ. Finally I define $PS_1 = l_1$, $PS_2 = l_2$ and $PS_3 = l_3$. It is a simple

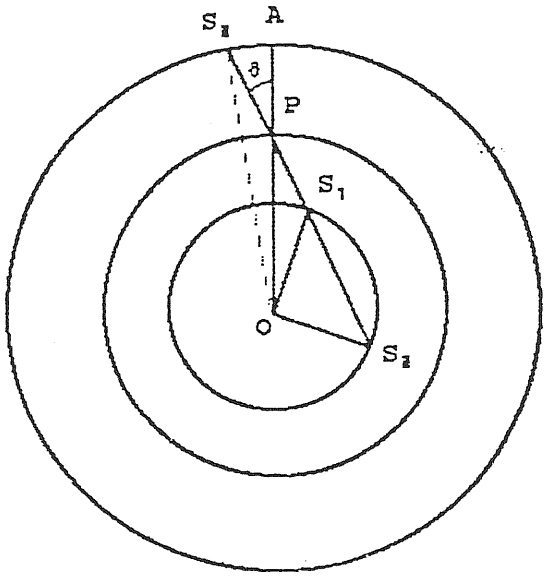

Fig. 2: Section of a spherical cloud. The radiation in P defined by an angle ϑ is computed integrating the contributions of spherical shells over the radius.

matter of elementary trigonometry to see that the following relations are valid:

$$\begin{aligned} l_1 &= R\mu - \sqrt{R^2\mu^2 + r^2 - R^2} \\ l_2 &= R\mu + \sqrt{R^2\mu^2 + r^2 - R^2} \\ l_3 &= -R\mu + \sqrt{R^2\mu^2 + r^2 - R^2} \end{aligned} \tag{2.25}$$

and

$$\alpha = \frac{R}{r}(1-\mu^2) \pm \frac{\mu}{r}\sqrt{R^2\mu^2 + r^2 - R^2} \tag{2.26}$$

Here the sign "−" is appropriate for l_2, the sign "+" otherwise.

The photon distribution $\mathcal{V}(I)$ at point R is then

$$\begin{aligned}\mathcal{V}(I) =& \frac{1}{4\pi}\int_0^R dr\, 2\pi r^2 I(r) \int_{\sqrt{R^2-r^2}/R}^1 d\mu \frac{d\alpha}{d\mu}\left(\frac{\mathrm{e}^{-l_1}}{l_1^2}+\frac{\mathrm{e}^{-l_2}}{l_2^2}\right) \\ &+ \frac{1}{4\pi}\int_R^\tau dr\, 2\pi r^2 I(r) \int_{-1}^1 d\mu \frac{d\alpha}{d\mu}\frac{\mathrm{e}^{-l_3}}{l_3^2}\end{aligned} \tag{2.27}$$

We have implicitly measured the spatial coordinates in units if $n_e\sigma(x)$. Now changing variables from μ to l we obtain

$$\begin{aligned}\mathcal{V}(I) &= \frac{1}{2R}\int_0^\tau dr\, rI(r) \int_{|r-R|}^{r+R} dl \frac{\mathrm{e}^{-l}}{l} \\ &= \frac{1}{2R}\int_0^\tau dr\, rI(r)[\mathrm{E}_1(|r-R|) - \mathrm{E}_1(r+R)]\end{aligned} \tag{2.28}$$

for $R \neq 0$ and

$$\mathcal{V}(I) = \int_0^\tau dr\, I(r)\mathrm{e}^{-r} \tag{2.29}$$

for $R = 0$. Here E_1 is the exponential integral function of first order. Because of the integrable singularity in $r = R$ numerical integrations are easily performed writing eq[2.28] as

$$\begin{aligned}\mathcal{V}(I) =& \frac{I(R)}{2}[2 - \mathrm{E}_2(R) - \mathrm{E}_2(\tau - R)] \\ &+ \frac{1}{2}\int_0^\tau dr \left\{\left[\frac{r}{R}I(r) - I(R)\right]\mathrm{E}_1(|r-R|) - \frac{r}{R}I(r)\mathrm{E}_1(r+R)\right\}\end{aligned} \tag{2.30}$$

The net flux escaping from the sphere surface after k scatterings can be calculated from eq[2.27] substituting R with τ and performing the inner integral over $\mu d\mu$ instead that over $d\mu$. The averaging factor $1/4\pi$ must be neglected too. We then obtain

$$\begin{aligned}4\pi\,\mathcal{V}(\mu I) &= \frac{\pi}{\tau^2}\int_0^\tau dr\, rI(r) \int_{\tau-r}^{\tau+r} dl \left(1 + \frac{\tau^2 - r^2}{l^2}\right)\mathrm{e}^{-l} \\ &= \frac{\pi}{\tau^2}\int_0^\tau dr\, rI(r)\left[\mathrm{e}^{-(\tau-r)} - \mathrm{e}^{-(\tau+r)} + (\tau+r)\mathrm{E}_2(\tau-r) - (\tau-r)\mathrm{E}_2(\tau+r)\right]\end{aligned} \tag{2.31}$$

To check the above formulae we can consider the case on Thomson scattering, in which space and energy integrations are separable as seen in §[2.3], and compute the

escape probability, i.e., the probability for a photon to escape from the source after k scatterings. This is simply the net flux divided the net flux in absence of opacity ,F_{thin}:

$$P_k = \frac{\pi F_k}{\pi F_{thin}} \tag{2.32}$$

Now from

$$\pi F_{thin} = \frac{4\pi}{3}\tau \tag{2.33}$$

we find

$$P_k = \frac{3}{4\tau^3}\int_0^\tau dr\, r J_k(r)\left[\mathrm{e}^{-(\tau-r)} - \mathrm{e}^{-(\tau+r)} + (\tau+r)\mathrm{E}_2(\tau-r) - (\tau-r)\mathrm{E}_2(\tau+r)\right] \tag{2.34}$$

In the case the soft photon source is homogeneously distributed within the sphere, using the appropriate initial condition

$$J_0(r) = 1 \tag{2.35}$$

we can solve for P_0, and we obtain the classical formula for the escape probability of a photon emitted in a spherical homogenous medium (see Zdziarski 1985, hereafter Z85)

$$P_0 = \frac{3}{4\tau^3}\left[\tau^2 - \frac{1}{2} + \left(\tau + \frac{1}{2}\right)\mathrm{e}^{-2\tau}\right] \tag{2.36}$$

2.4.3 Radiation transfer in plane parallel geometry

Another relevant 1-D case is a plane parallel geometry of scattering depth $\tau = n_e\sigma(x)Z$. Respect to the spherical case, a main difference is that even assuming isotropic scattering, the observed spectrum does depend on the viewing angle because of limb darkening effect.

We indicate with z the vertical coordinate along the slab. In a similar way as seen in the previous §[2.4.2] for a spherical geometry, we find the radiation transfer operator $\mathcal{V}$:

$$\mathcal{V}(I) = \frac{1}{2}\int_0^\tau d\xi\, I(\xi)\mathrm{E}_1(|z-\xi|) \tag{2.37}$$

The above expression assumes an isotropic radiation field, i.e.,

$$I_k^+(z,\mu) = I_k^-(z,\mu) = I_k(z) \tag{2.38}$$

for $k \geq 1$.

In the case the source of seed photons is located only on one side of the slab, the first scattering must be computed taking into account the angular dependance of input the radiation field. Given the initial condition $I_0^+(z,\mu)$ and $I_0^-(z,\mu)$ the source function satisfies the following equation:

$$\mathcal{V}(I_0) = \frac{1}{2}\int_0^1 \frac{d\mu}{\mu}\left\{\int_0^z d\zeta\, I_0^+(\zeta,\mu)\exp\left[-(z-\zeta)/\mu\right] + \int_z^\tau d\zeta\, I_0^-(\zeta,\mu)\exp\left[-(\zeta-z)/\mu\right]\right\} \tag{2.39}$$

The escape probabilities $p_k(\mu)$ from the upper ($z = \tau$) and the lower ($z = 0$) surfaces are given by

$$\begin{aligned} p_0(\mu) &= 2\int_0^\tau dz J_0^+(z,\mu)\exp\left[-(\tau-z)/\mu\right] \\ p_k(\mu) &= 2\int_0^\tau dz J_k(\tau-z)\exp\left(-z/\mu\right), \quad \mu > 0, \quad k \geq 1 \\ p_k(\mu) &= 2\int_0^\tau dz J_k(z)\exp\left(-z/|\mu|\right), \quad \mu < 0, \quad k \geq 1\ . \end{aligned} \tag{2.40}$$

The total escape probability is normalized so as

$$\sum_{k=0}^{\infty}\int_{-1}^{1} d\mu p_k(\mu) = 1\ . \tag{2.41}$$

It should be considered that the coordinates z as well as r in the previous §[2.4.2] are energy dependent, as they are in units of $n_e\sigma(x)$. The equations describing the evolution of the source function (both in spherical and plane–parallel geometry) have then different normalizations for different photon energies. It is straightforward to see that the normalization of the source functions results correct for any photon energy if we change the integration variable from from z to $z/\tau(x)$ [or from r to $r/\tau(x)$].

Finally I would like to point out that for the sake of simplicity in the above radiative transfer equations the polarization of the scattered radiation is not taken into account.

The polarization properties of scattering have been computed by Sunyaev & Titarchuk (1985), and Philips & Meszaros (1985) solving the radiative transfer equation for a pure scattering, plane parallel atmosphere by separation of different scattering orders. Due to the forward-backward symmetry of the Rayleigh phase matrix used in the calculations, possible anisotropies in the energy transfer had not been taken into account and results are then fully correct for either cold electrons, or forward-backward symmetric source functions. Recently Poutanen (1994) provided new calculations of Compton scattering, taking into account the anisotropy of the scattering matrix, relativistic corrections and the induced polarization of the scattered radiation field. The photon distributions calculated with the simplified radiative transfer formulae given in this Chapter match well the distributions obtained summing over the polarization states (Poutanen 1994, private communication).

2.5 Anisotropic IC emission

In this Section I recall some of the results described in Haardt (1993).

In the general case, the assumption of complete isotropy is unrealistic because of an anisotropic soft photon input. A typical case is a plane parallel slab with the seed photon source located on the lower surface.

Contrary to the case of complete isotropy, in which the fraction dN of scattered photons per unit solid angle and their mean energy $\langle x \rangle$ are independent on direction, anisotropy implies an explicit dependence of dN and $\langle x \rangle$ on Ω. In the scattering process the electron radiative losses are larger (in the laboratory frame) in the backward direction respect to the incoming photons. Integrating the scattered photon flux over all the emission angles one obtain the results found in the case of complete isotropy. The importance of this effect strongly depends on the electron energy (for a complete discussion see Ghisellini et al. 1991).

2.5.1 Anisotropy coefficients

In order to take into account the anisotropy effects I initially considered a unidirectional radiation beam. I introduced two dimensionless coefficients, $\phi(\omega)$ and $\chi(\omega)$, representing the degree of anisotropy in the scattering event as a function of the cosine of the scattering angle ω. The coefficients are defined by the following relations:

$$dN = (1/4\pi)\phi(\omega)d\omega d\varphi \tag{2.42}$$

and

$$\langle x \rangle = [4/3(\gamma^2 - 1) + 1]\chi(\omega)x' \ . \tag{2.43}$$

By definition

$$\frac{1}{2}\int_{-1}^{1} d\omega\phi(\omega) = 1 \tag{2.44}$$

and, defining $\xi(\omega) = \phi(\omega)\chi(\omega)$,

$$\frac{1}{2}\int_{-1}^{1} d\omega\xi(\omega) = 1 \ . \tag{2.45}$$

The two coefficients depend also on the electron energy.

Then I computed the scattered photon distribution considering electrons joining angle dependent *effective* energy distributions. i.e., the kernel is assumed to have the same form as eq[2.16] or eq[2.22], but the scattering electrons have different energy distributions for different scattering angles, so that the photon number flux and the mean photon energy after the scattering matches eq[2.42] and eq[2.43], respectively.

I defined an effective angle dependent energy distribution N_{eff} such as

$$\left[\int_1^\infty d\gamma(\gamma^2 - 1)N_{eff}(\gamma,\omega) + 1\right]\chi(\omega) = \left[\int_1^\infty d\gamma(\gamma^2 - 1)N(\gamma) + 1\right] \tag{2.46}$$

The averaged anisotropic kernel was written as

$$\tilde{K}(x\omega\mathbf{u}, x'\mathbf{u}) = \phi(\omega)\int_0^\infty d\gamma\, K(x, x', \gamma)\, N_{\rm eff}(\gamma,\omega) \ . \tag{2.47}$$

where $\mathbf{u}$ is a unit vector parallel to the input photon direction.

2.5.2 Anisotropic first scattering distribution

In order to compute the anisotropic photon distribution for a generic axisymmetric input photon distribution, I considered a plane parallel scattering medium. More details can be found in Haardt (1993). In the assumed geometry the anisotropy of the radiation field is forced to produce relevant spectral distortions only in the first scattering distribution (Haardt 1993). Thus I considered only the evolution from $I_0(x\mathbf{\Omega}, z)$ to $I_1(x\mathbf{\Omega}, z)$ although the formalism has a general validity.

In the following we indicate with μ' and μ the cosine of the angles between the reference axis (i.e. the normal at the slab) and the photon direction before and after the scattering, respectively.

As a first step, I computed the distribution $P(\omega, \mu, \mu')$ of the scattering angle in direction μ for a given initial direction μ'. The problem can be solved by means of simple geometrical arguments, noting that

$$\omega = \mu\mu' + \sqrt{1-\mu^2}\sqrt{1-\mu'^2}\cos(\rho - \rho') \ , \tag{2.48}$$

where ρ' and ρ define the azimuthal angle before and after the scattering, respectively. Due to symmetry, we can set $\rho' = 0$, and find

$$d\rho = \pm(1 - \mu^2 - \mu'^2 + 2\mu\mu'\omega - \omega^2)^{-1/2} d\omega \ . \tag{2.49}$$

It is easy to see that

$$P(\omega, \mu, \mu') = 2\left|\frac{d\rho}{d\omega}\right| \tag{2.50}$$

where the factor 2 takes into account the change of sign in $d\rho$. Because of the symmetry of the problem, the distribution P is independent on the azimuthal angle.

Then I computed the anisotropic averaged kernel as

$$\tilde{K}(x\mu\mathbf{u}, x'\mu'\mathbf{u}) \equiv \int_{\omega_m}^{\omega_M} d\omega \, \tilde{K}(x\omega\mathbf{u}, x'\mathbf{u}) P(\omega, \mu, \mu') \tag{2.51}$$

where the two integration limits in ω are given by eq[1.6] and eq[1.7] (Chapter 1).

In practical calculations it is convenient to average the coefficients ϕ and ξ as

$$\phi(\mu,\mu') = \frac{1}{2\pi}\int_{\omega_m}^{\omega_M} d\omega P(\omega,\mu,\mu')\phi(\omega) \tag{2.52}$$

and

$$\xi(\mu,\mu') = \frac{1}{2\pi}\int_{\omega_m}^{\omega_M} d\omega P(\omega,\mu,\mu')\xi(\omega) \tag{2.53}$$

The averaged anisotropic kernel $\tilde{K}(x\mu\mathbf{u}, x'\mu'\mathbf{u})$ was then computed via eq[2.46] and eq[2.47] writing $\chi(\mu,\mu')$ as $\xi(\mu,\mu')/\phi(\mu,\mu')$.

One should take into account that, since a plane parallel scattering medium has a finite vertical extension, photons travelling at grazing angles ($\mu' \sim 0$) have a mean scattering probability higher than photons travelling in the slab along the normal ($\mu' \sim 1$). The angular distribution of the input photons must be weighted by means of the following normalized function

$$f(\mu',z') = \frac{1-\exp[(z'-\tau)/\mu')]}{\int_0^\tau dz' \int_{-1}^{+1} d\mu' f(\mu',z') \int_0^\infty dx' I_0(x'\mu'\mathbf{u},z')} \tag{2.54}$$

The procedure discussed here is valid only for the first order distribution $I_1(x\mu\mathbf{u},z)$. Higher order scatterings can be treated as in the case of complete isotropy. An average isotropic distribution can be used to compute $I_2(x,z)$.

2.6 Numerical computation

In this Section we outline the numerical procedure used to compute the Comptonized spectrum.

Initially, we have evaluated the full relativistic kernel [2.16] over a $100 \times 100 \times 100$ grid for $1 \leq \gamma \leq 10$, and $10^{-6} \leq x, x' \leq 10^2$. The grid has been designed with logarithmic step sizes, and the same sampling has used for x and x'. Of course this calculation is performed just once forever and the file containing the output stored.

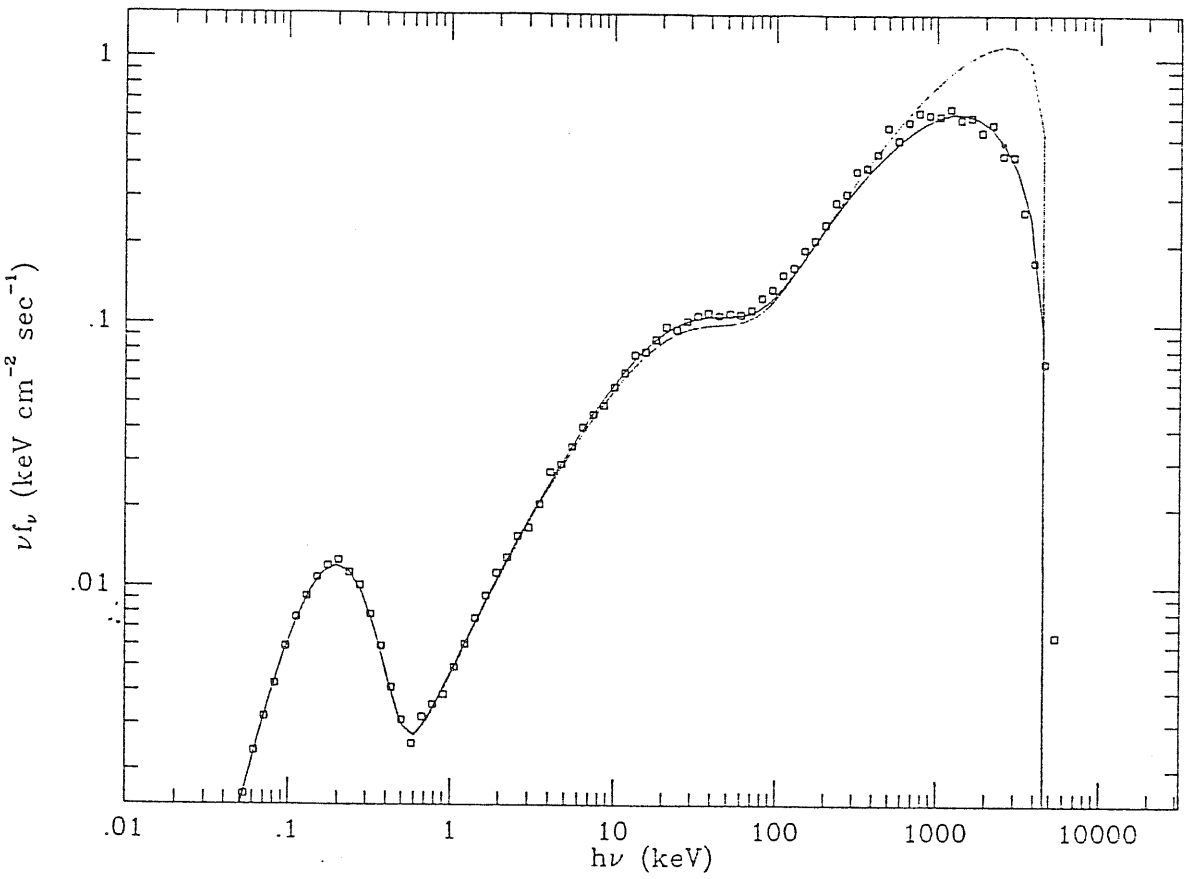

Fig. 3: A semi-analytical calculation (solid line) is compared with an output of a Montecarlo simulation (open squares). A cloud ($\tau = 0.1$) of non-thermal electrons [$N(\gamma) \propto cost$] scatters an homogeneously distributed black body spectrum ($kT_{BB} = 50$ eV). The dotted line is the resulting spectrum assuming a Thomson total cross section. The integral over energy of the photon spectrum ($\propto f_\nu/\nu$) is the same for the two analytical curves. Note that the Klein-Nishina reduction of the total cross section allows more photons to escape from the cloud after a single scattering. This in turn implies that less photons (compared to the Thomson case) are avaliable for a second scattering.

In order to compute an output model, we can proceed as follows:

1) The first step consists in writing the electron Lorentz factor distribution. The normalized distribution is treated as an input array. A single input parameter (the temperature) is sufficient to define it for a thermal plasma, but virtually any distribution can be considered. The electron distribution is sampled in the same one hundred γ points used for the kernel grid.

2) The Thomson scattering optical depth must be specified as an input value.

3) The energy dependent scattering depth is computed averaging the total Klein–Nishina cross section over the electron distribution in each of the one hundred points x'. A gaussian integration routine is used for this purpose.

4) The kernel is averaged over the electron distribution, and reduced to a two dimensional array. I have used a linear interpolation between the γ sampling points.

5) The spectrum computation is performed in a subroutine according to the chosen geometry.

   5.a) The input photon energy distribution (e.g. a black body) is evaluated in the points x of the kernel grid. The input photon distribution is evaluated in a grid of m radial points. The number of points must be chosen accordingly to the value of the Thomson opacity. For low opacity in slab geometry, the successive source functions are quasi–linear in z. I have checked that m=10 gives enough precision for $\tau \lesssim 0.5$. For $\tau \lesssim 0.05$ three sampling points are sufficient. For higher opacity the source functions are no longer quasi–linear in z, and a finer sampling must be used. The same considerations are valid for a spherical source if one consider a change of variable from r to $p \equiv r^2$. The source functions for low τ are then quasi–linear in p.

   5.b) The $(i+1)$–th source function is computed from the i–th source function using the formulae given in §[2.4.2] or §[2.4.3]. We have used simple linear interpolation, and the polynomial approximations for the exponential integral functions given in Gautschi & Cahill (1970). In the case of the slab geometry, the first scattering distribution is anisotropic. In this case the first anisotropic distribution can be computed as shown in Haardt (1993).

Computer time can be saved optimizing the energy integration loops, e.g., estimating at each step the range of energies where the successive source function is different from zero.

In Fig. 3 I show an example of calculation for a somewhat extreme case. A

spherical geometry is adopted. The electrons have a flat power–law energy distribution [$N(\gamma) \propto$cost] extending up to $\gamma = 10$. The Thomson scattering opacity of the cloud is $\tau = 0.1$. The spectrum is computed using the formalism described in this Chapter and compared with a Montecarlo simulation. The effect of neglecting the decrease of the total cross section is also shown. On an DIGITAL DEC 3000 roughly 30 minutes of c.p.u. has been necessary for the Montecarlo simulation, while less than 3 seconds sufficed for the semi–analytical calculation.

Chapter 3

Physics of Thermal Pair Plasmas

"QUANDO IO CREDERÒ IMPARARE A VIVERE, E IO IMPARERÒ A MORIRE". – LEONARDO DA VINCI

3.1 Introduction

In the standard accretion disk scenario (Shakura & Sunyaev 1973), the gravitational energy liberated by accretion is locally emitted by the accreting flow as thermal radiation, which falls in the UV band in the case of AGNs and in the soft–X ray domain for GBHs. The origin of the X-ray and γ–ray emission is still unknown. Successful models should satisfy the observational constraints discussed in Chapter 1. They can summarized as follows:

1)The size of the X-ray production region must be small due to the fast variability, with typical time scales of hours (e.g. McHardy 1989).

2)The observed spectrum in the medium X-ray range (2-20 keV) is close to a power law, with a small dispersion in the values of the spectral index, whose average for Seyfert galaxies is $\simeq 0.7 \pm 0.15$ (Mushotzky 1984, Turner & Pounds 1989).

3) Whatever produces the X-rays is close to cold reflecting matter, as inferred from the presence of fluorescent Fe line emission and of a Compton reflection hump, which has a broad maximum around $\simeq$ 30 keV (Nandra 1991, Williams et al. 1992). In fact after deconvolution of the latter component the spectral index of the underlying power law is revised to $\simeq 0.9 - 1$ (Pounds et al. 1990, NP94).

4) The soft $\gamma-$ray spectrum steepen around 100–200 keV (Jourdain et al. 1992; Cameron et al. 1992; Maisack et al. 1993; Madejski et al. 1994) and no annihilation line or hard $\gamma-$ray tail have been detected so far.

Two classes of models have been proposed to explain the power law shape of the X-ray spectrum. One is based on the production of very high energy primaries and strong reprocessing via electromagnetic cascades leading to the formation of an $e^{\pm}$ pair plasma (e.g. Zdziarski et al. 1990). The second involves multiple Compton scattering (Comptonization) of soft photons on a thermal population of hot electrons (e.g. Walter and Courvoisier 1992). The main difference between thermal and non–thermal models consists in the assumption made on the channelling of the available power. If the power is equally channeled into all the electrons we talk about thermal plasma, while if the power is channeled into a tiny fraction of the electrons we are dealing with non–thermal plasma. Physically, one can think that in a thermal plasma the cooling time is longer than the particle–particle collision time, the contrary for a non–thermal plasmas.

Although the non–thermal pair model (for a review see Svensson 1992, 1994) predicts a steepening of the hard X-ray spectrum, the break cannot be as sharp as the OSSE data simply require. Furthermore, the non–thermal pair model predicts a flattening of the spectrum at $\sim 100 - 200$ keV, and the presence of a conspicuous annihilation line, neither of which is observed. These observations and the upper limits derived by EGRET (Lin et al. 1993) instead can be interpreted in the framework of thermal Comptonization models. If this is the case, also the X–ray background can be best explained as the sum of the emission of Seyfert galaxies, even if it is not yet clear which type of Seyfert galaxies contribute the most (see Madau et al. 1993, 1994 for a model in which Seyfert 2 galaxies are dominant, and Zdziarski et al. 1993 for a model in which Seyfert 1 galaxies form the major contribution).

L. Maraschi and I (Haardt & Maraschi 1991; 1993, hereafter HM93) have proposed a specific thermal model that naturally predicts a power law spectrum of index close to 0.8–1 below 40 keV and steeper above, by assuming that all the power is released

in a hot corona above a relatively cold accretion disk. About half of the radiation emitted by the corona impinges onto the disk: the largest fraction of it is re–emitted as soft thermal radiation, while $\sim$ 10 per cent is Compton scattered to form the so-called Compton reflection hump. The photons reprocessed by the disk are then the seed photons which are thermally Comptonized in the corona. Electron-positron pair production contributes to the optical depth, and limits the minimum possible optical depth and maximum allowed temperature.

Before entering in the details of such a model (this will be done in the next Chapter), I will discuss the role played by $e^{\pm}$ pair production and annihilation in thermal plasmas. For the moment the radiating source is somewhat idealized, in the sense that only the microphysics is considered regardless any macrophysics of the accreting process.

Part of the content of this Chapter has been published in Ghisellini et al. (1993), and in Ghisellini & Haardt (1994). For a complete theory of thermal $e^{\pm}$–pair plasmas the reader should refer to the classical papers by Bisnovatyi–Kogan et al. (1971), Svensson (1982a, 1982b, 1983, 1984), Lightman (1982) and Zdziarski(1985).

3.2 Physical processes in compact sources

3.2.1 Cooling processes

The key parameter describing a compact source emitting a luminosity L within a typical size scale R is the *compactness* (see, e.g., Cavaliere & Morrison 1980; Gulibert et al. 1983) which is defined as

$$\ell \equiv \frac{L}{R}\frac{\sigma_T}{m_e c^3} \simeq 10^4 \times \frac{\mathcal{L}}{r} \tag{3.1}$$

where $\mathcal{L}$ is the total luminosity of the source in Eddington luminosity units, and r is the scale size in units of the Schwarzschild radius $2GM/c^2$. The compactness deter-

mines the most effective cooling mechanism for the radiating particles. The latter are thought to be electrons and/or positrons, the much higher mass of the proton usually meaning that its cooling radiation is negligible. Neglecting radiative processes involving particle–magnetic field interactions (cyclo/synchrotron), the two competing processes are particle–photon (Compton) and particle–particle (bremsstrahlung) interactions. The main difference is that no new photons are create in a scattering process, so that in the case of Compton cooling an external low frequency radiation field (soft photon input) is required.

The free–free cooling time for a population of thermal light particles (electrons or positrons) of temperature T is

$$t_{ff} \approx \frac{\Theta^{1/2}}{n\alpha_f \sigma_T c} \tag{3.2}$$

where α_f and n are the fine structure constant and the particle number density, respectively. The cooling time for particles due to IC scattering on an ambient radiation field of energy density U_{rad} is

$$t_{IC} \approx \frac{3}{8}\frac{m_e c^2}{\sigma_T c U_{rad}} \tag{3.3}$$

For a spherical source of scattering optical depth τ, from

$$U_{rad} \approx \frac{L}{4\pi R^2 c}\max[\tau, 1] \tag{3.4}$$

we derive

$$t_{IC} \approx \frac{3\pi R}{2c\ell}\max[\tau, 1] \tag{3.5}$$

Now we can say that Compton scattering dominates particle cooling when $t_{IC} < t_{ff}$. Working out the formulae given above, this occurs when

$$\ell \gtrsim \frac{0.03}{\sqrt{\Theta}} \tag{3.6}$$

Observationally from the 2–10 keV luminosity and the two folding time–scale (i.e., the time–scale in which a source doubles or halves its luminosity) one can infer a lower limit to ℓ, which for AGNs is between 1 and 100, being $\ell > 10$ in several sources (Done

& Fabian 1989). Recalling that the recent γ–ray observations by OSSE seem to imply $0.1 \lesssim \Theta \lesssim 1$, we see that Compton scattering is probably the dominant cooling process in AGNs and GBHs.

3.2.2 Pair balance

An excellent review of pair processes in astrophysical plasmas is Svensson (1986), and the reader should refer to it for a complete discussion. Here I address the attention to the useful formulae that will be used later.

Photon–photon interactions can create $e^{\pm}$ pairs which in turn can annihilate to produce photons. It was realized by Jelley (1966) and Herterich (1974) that a cloud is optically thick to photon–photon pair production for a photon of energy E if the photon density above the threshold energy $(m_e c^2/E)m_e c^2$ is high enough. The optical depth to photon–photon pair production can be approximated as (see Svensson 1994)

$$\tau_{\gamma\gamma} \sim n_\gamma \sigma_T R \sim \frac{\ell}{4\pi} \tag{3.7}$$

where most of the photons are assumed to be at $E \sim m_e c^2$. The above equation suggests that pair production is an important ingredient in the overall energetics of AGNs and GBHs.

In thermal plasmas new created particles (pairs) are assumed to join the thermal distribution in a time–scale shorter than any other characteristic time–scale. The physical state of the cloud can be solved assuming pair equilibrium, i.e., pairs do annihilate at the same rate at which they are create. Moreover one has to specify the main radiation mechanism operating in the clouds as it determines the photon spectrum which in turn controls the pair production rate. In equilibrium the total optical depth can be written as the sum of the contributions due to pairs and to "normal" plasma electrons, i.e., $\tau = \tau_p + \tau_{e^\pm}$.

In order to find the constraints imposed by the presence of pairs we have to solve

the pair balance equation. Here I recall the basic equations of pair equilibrium following Z85, assuming IC scattering as the main cooling process. The pair balance equation can be written synthetically in the form:

$$\tau_p^2 = \tau^2(1 - \Lambda) \tag{3.8}$$

where

$$\Lambda = \frac{\left(\frac{N_P}{n_e}\right)^2 \left[f_{PP} + \frac{N_W}{N_P} f_{PW} + \left(\frac{N_W}{N_P}\right)^2 f_{WW}\right]}{f_A} \tag{3.9}$$

In writing the above equation no pair escape is allowed beside annihilation. Furthermore for the interested range of temperatures we have considered photon-photon interactions as the main pair production mechanism. Pair escape can be considered by means of a phenomenological escape rate

$$f_{esc} = \frac{\beta_{esc}}{\tau} \tag{3.10}$$

where $\beta_{esc} = v_{esc}/c$. This rate can be simply added to the annihilation rate. In eq[3.9] n_e is the number density of electrons and positrons and N_W and N_P are related to the densities of photons in the Wien and power law portion of the IC spectrum respectively. The terms f_{PP}, f_{PW}, f_{WW} are dimensionless pair production rates from photon photon interaction where the photons belong to the power law (P) and/or Wien (W) portion of the spectrum, while f_A is the annihilation rate.

In view to write N_P/n_e in pair equilibrium equation we approximate the Compton spectrum as a power-law with an exponential cut-off at $x = \Theta$, superposed with a Wien spectrum at $x = 3\Theta$ (Z85):

$$N_\gamma(x) = \frac{1}{2} N_P \left(\frac{x}{\Theta}\right)^{-\alpha_x} \frac{\mathrm{e}^{-x/\Theta}}{x} + \frac{1}{2} N_W \left(\frac{x}{\Theta}\right)^3 \frac{\mathrm{e}^{-x/\Theta}}{x} \tag{3.11}$$

The density ratio between power law photons and Wien photons N_P/N_W can be expressed in terms of Gamma functions. Finally N_P and N_W can be normalized to the total photon density N_γ.

For pair production rates involving only Wien photons and for the annihilation rate numerical fits have been performed by Svensson (1984) and Z85:

$$\begin{aligned} f_A &= \frac{\pi}{4}[1+2\Theta^2/\ln(1.1229\Theta+1.3)]^{-1} \\ f_{WW} &= \frac{\pi^2}{8}\Theta^{-3}\mathrm{e}^{-2/\Theta}(1+2.88\Theta^{0.934}), \quad \Theta<1 \\ f_{WW} &= \frac{\pi}{2}\Theta^{-2}\ln(1.1229\Theta+0.38), \quad \Theta>1 \end{aligned} \tag{3.12}$$

Terms f_{PP} and f_{PW} can be obtained by direct integration over the pair production cross section (see Svensson 1984 for details):

$$\begin{aligned} f_{PP} &= \frac{\pi}{4}\Theta^{2\alpha_x}\int_1^\infty \phi(s)s^{-\alpha_x-3}\mathrm{K}_0(2\sqrt{s}/\Theta)ds \\ f_{PW} &= \frac{\pi}{2}\Theta^{-3+\alpha_x}\int_1^\infty \phi(s)s^{-(\alpha_x+3)/2}\mathrm{K}_{3+\alpha_x}(2\sqrt{s}/\Theta)ds \end{aligned} \tag{3.13}$$

The function $\phi(s)$ is proportional to the pair production cross section averaged over angles.

3.3 Thermal Comptonization and pair production

3.3.1 Solution of the equations

Thermal Comptonization has been extensively studied in the past (see e.g. Sunyaev & Titarchuk 1980, Pozdnyakov et al. 1983). As discussed before, in the compact emission regions of AGNs Comptonization is likely the most efficient radiation mechanism.

We assume that soft photons are homogeneously distributed throughout a sphere of radius R with a diluted black body spectral distribution of dimensionless temperature Θ_{BB}. The sphere is homogeneously filled with hot plasma, with dimensionless temperature Θ, producing, via Comptonization, a luminosity L_h corresponding to a compactness ℓ_h. Analogously, ℓ_s is the compactness of the soft photon source.

The scattering optical depth, τ, and the temperature, Θ, of the hot plasma uniquely determine the Comptonized photon energy distribution, characterized by a power law and a cut–off at $x \sim \Theta$. Therefore the temperature Θ and the spectral index α_x (instead of Θ and τ) can be regarded as the two variables.

Although sufficient to completely determine the shape of the Comptonized photons, α_x and Θ do not yield its normalization, but only the amplification factor, i.e. the ratio ℓ_h/ℓ_s. Symbolically:

$$(\alpha_x, \Theta) \rightarrow \ell_h/\ell_s \tag{3.14}$$

Note that the reverse is not true, since the same amplification can be achieved with a range of values of α_x–Θ.

In order to determine the absolute value of ℓ_h and ℓ_s one has to consider the effects of $e^{\pm}$ pair production. The main result of hot plasma studies is that the compactness of a source in equilibrium at a given temperature cannot reach arbitrary large values. In fact, as long as the compactness is very small, an increase in the heating rate corresponds to an increased mean energy per particle, and therefore to an increased temperature. But when the temperature starts to be relativistic pair production is important, and the number of particles in the thermal bath increases. Since the available energy is now shared among more particles, the temperature in this regime decreases as the heating rate (the compactness) increases. The equilibrium and steady state corresponds to pair balance: pairs are destroyed at the same rate at which they are created. For any given temperature there is a *maximum* compactness allowing pair equilibrium, and for any given compactness there is a *maximum* allowed temperature. The precise value of the function $\ell_{h,max}(\Theta)$ depends on the detail of the emission mechanism (bremsstrahlung, Comptonization, cyclosynchrotron, and so on). Hereafter the symbol ℓ_h will be used to indicate the maximum allowed value $\ell_{h,max}$.

If the main radiation mechanism is Comptonization, any pair of values of α_x and

Θ determines the maximum allowed compactness ℓ_h. Symbolically we have:

$$(\alpha_x, \Theta) \iff (\ell_h, \ell_s) \tag{3.15}$$

Note that now there is a one–to–one relation between the physical parameters of the source (ℓ_h and ℓ_s) and the observable quantities (α_x and Θ).

We have repeated the calculation of Z85 for different values of $\alpha - x$ limiting ourselves to temperatures $\Theta < 10$ ($kT < 5$ MeV), where particle–particle and particle–photon pair production processes are less important that photon–photon interactions, and can therefore be neglected.

As previously discussed the Comptonized spectrum is described as the sum of a power law spectrum with an exponential cut–off at Θ and a Wien spectrum at Θ: $\ell_h = \ell_{pl} + \ell_W$. We computed the Comptonized spectra in spherical geometry by means of the full relativistic kernel (Jones 1968, Coppi & Blandford 1990). discussed in Chapter 2. This gives the exact value ℓ_h/ℓ_s for any (τ, Θ). We checked that, with the given τ and Θ, the spectral indices used following the prescription of Z85 were correct. We used $\Theta_{BB} = 2 \times 10^{-5}$ (10 eV) and neglected for simplicity pair escape. Note that in the absence of pair escape there is an absolute maximum in the allowed temperature ($\Theta_{max} = 24$) derived considering particle–particle interactions.

Our calculations are presented in Fig. 1. As can be seen the curves $\ell_h(\Theta)$ have a sort of pivot at $\Theta \sim 1$, being flatter for flatter spectral indices.

To qualitatively understand this behaviour, let consider first a fixed value of Θ in the region corresponding to $\ell_h > 1$. As $\Theta < 1$, the only photons effective in pair production are in the Wien tail of the spectrum (see e.g. Fig. 4a of Z85).

Furthermore, if $\tau > 1$, simple radiative transfer assures that the compactness of the Wien component is fixed (it depends only on Θ) independently of τ. Increasing the total compactness then means to increase the compactness of the power law component. But the two compactnesses are related by the value of τ: their ratio ℓ_{pl}/ℓ_W decreases as τ increases (more photons are driven to the Wien peak). Only a lower τ (i.e. steeper

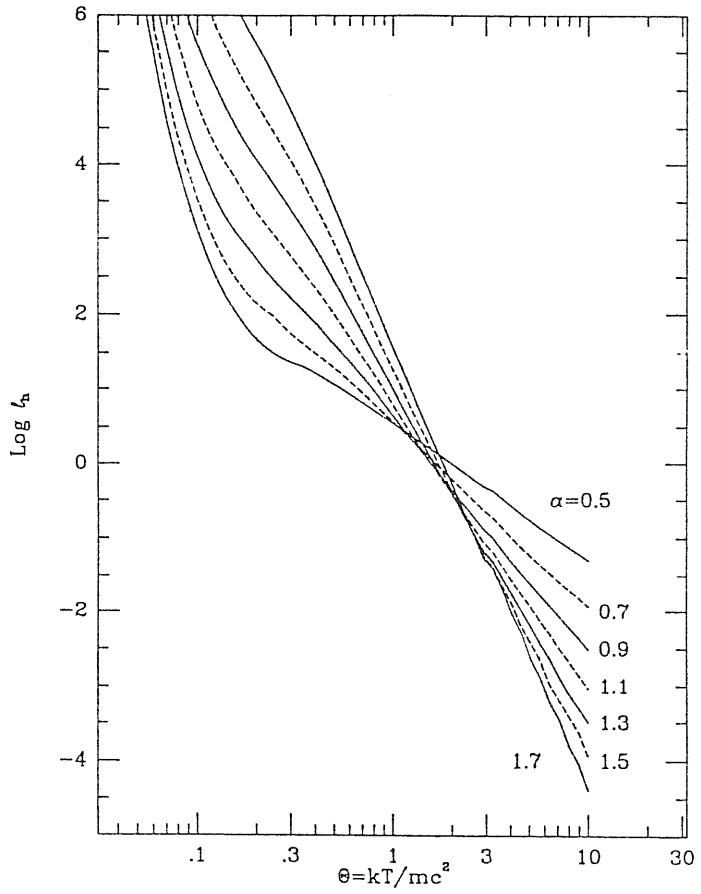

Fig. 1: For any given temperature $\Theta \equiv kT/(m_e c^2)$ there exists a maximum possible compactness ℓ_h of a plasma in pair equilibrium. The exact shape of the function $\ell_h(\Theta)$ depends on the spectral index resulting from the Comptonization process. Flatter spectral indices correspond to flatter $\ell_h(\Theta)$. Note that the curves (the labels indicate the value of the spectral index) cross for $\ell_h \sim 1$. For $\ell_h > 1$, sources with the same compactness have larger temperatures if their spectrum is steeper, and viceversa (from Ghisellini & Haardt 1994).

α_x) therefore allows a greater compactness of the power law component.

Consider now the region corresponding to $\ell_h < 1$. In this case both the total luminosity and the pair production process are determined by ℓ_{pl}, ℓ_W playing no role. For fixed Θ, ℓ_h can increase if:

1) The new equilibrium state yields a greater τ and therefore a flatter spectral index. In this case the luminosity is increased at high energies increasing the pair production rate, which in turn yields the required increased τ.

2) The new equilibrium state yields a much lower value of τ and a much steeper spectrum. In this case the luminosity is increased at low energies and decreased at high energies, the pair production rate is decreased, and the corresponding τ decreases.

The first solution gives $\alpha_x < 1$ while the second one yields $\alpha_x > 1$. Although both these solutions are consistent with pair balance and Comptonization, the latter one exists only in a range of Θ. This range becomes larger for small values of the minimum energy of the Comptonized spectrum x_1 (where most of the luminosity is for $\alpha_x > 1$). For the adopted Θ_{BB} the two solutions exist only in the small range $1 < \Theta < 2$ as shown in Fig. 1.

Fig. 1 shows that in the interesting (from the observational point of view) parameter range $0.1 < \Theta < 1$ pair dominated sources with same compactness should show a clear correlation between the spectral index and the cut–off energy: the flatter the spectral index, the lower the temperature.

Note that, as shown in Fig. 1, the maximum possible compactnesses for $kT \sim 50$ keV are extremely large, but these corresponds to completely pair dominated sources: if the hot emitting plasma has also a 'normal', electron–proton component, the compactness can be smaller (or the temperature can be smaller than shown in Fig. 1 for the same compactness).

3.3.2 Mapping

Thermal Comptonization together with pair plasma theory gives a one–to–one relation between α_x–Θ and ℓ_s–ℓ_h. This means that we can 'map' the plane α_x–Θ into the plane ℓ_s–ℓ_h (or equivalently ℓ_h/ℓ_s–ℓ_h), and viceversa.

This 'mapping' links physical parameters, such as the soft and the hard compactness, which completely characterize the source, with observable quantities, such as the spectral index and cut–off energy.

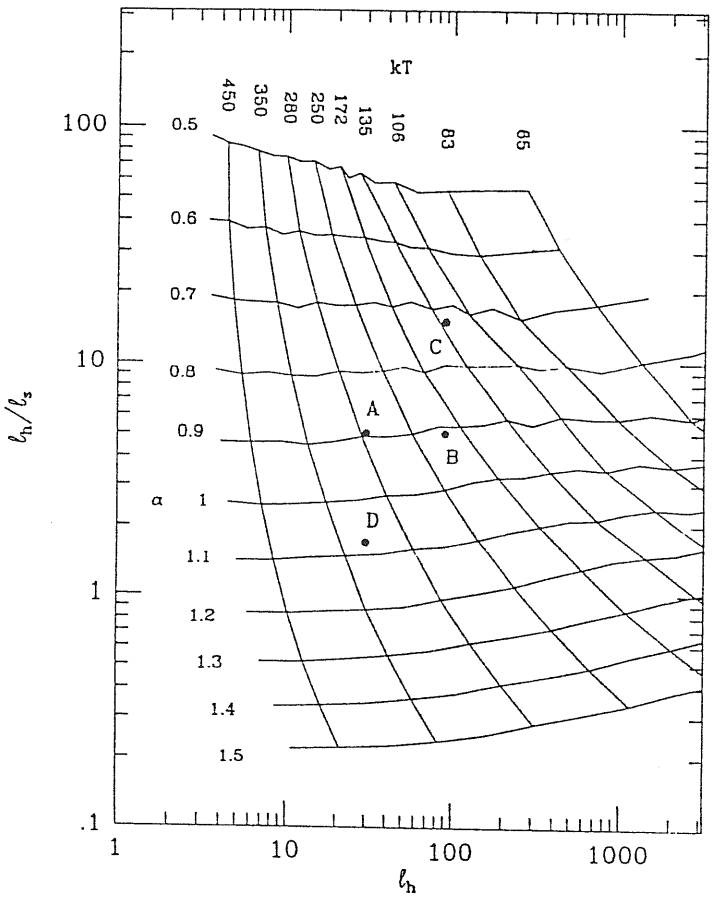

Fig. 2: In the plane ℓ_h/ℓ_s vs ℓ_h (the starvness vs hard compactness plane) we have drawn the curves for constant Θ (solid lines) and for constant α_x (dashed lines). The temperature increases from right to left, α_x increases (the spectrum steepens) from top to bottom, as labelled. As illustration, consider a source, initially in point A, which increases ℓ_h by a factor 3. Its final equilibrium state will be between points B and C, according if ℓ_s remains constant or increases by the same amount of ℓ_h. If instead ℓ_s increases by a factor 3 without variations in ℓ_h, the final equilibrium state will correspond to the point labelled D (from Ghisellini & Haardt 1994).

Fig. 2 shows the results. In the 'starvness–compactness' plane (i.e ℓ_h/ℓ_s–ℓ_h) we have mapped the 'temperature–spectral index' plane, plotting level curves for constant Θ and for constant α_x. We have restricted our analysis to the range which is observationally interesting (i.e. $0.5 < \alpha_x < 1.5$ and $0.1 < \Theta < 1$ corresponding to $51 < kT < 511$ keV).

It can be seen that ℓ_h/ℓ_s is not exactly constant for a given spectral index, but it

has some weak dependence also on the temperature.

Moving along a curve with constant Θ in the direction of steeper α_x we have that ℓ_h/ℓ_s decreases (as expected), while ℓ_h increases (as explained in the previous section §[3.3.1], and also shown in Fig. 1).

In this plane it is very easy to see what the equilibria states are when the source varies. For instance, suppose that a source initially in point labelled A in Fig. 2 increases its power (ℓ_h) by a factor 3. The compactness in soft photons, ℓ_s, can either remain constant or vary together with ℓ_h. The latter case may indicate that there is some feedback between the hot plasma producing the hard luminosity and the relatively cold plasma producing the seed photons, as in a cold disk illuminated by a hot corona.

The final states in the two cases are labelled B and C in Fig. 2. As can be seen, point B corresponds to a temperature lower by a factor 1.5 and slightly steeper spectral index, while point C corresponds to a much lower temperature (factor 2) and a flatter spectral index. All the possible intermediate cases $5 \lesssim \ell_h/\ell_s \lesssim$ are between points B and C.

Another possibility is that the soft compactness varies even without any change in ℓ_h. This is possible only if reprocessing (as a source of soft photons) is not important. Point labelled D corresponds to the final state of the source initially in A after an increase by a factor 3 of ℓ_s. The resulting equilibrium temperature is larger by a factor 1.2, and the spectrum has steepened.

It is worth to stress that the quantity ℓ_s refers to the soft compactness as 'seen' by the hot plasma, which can be different from what we observe (e.g. the UV bump in Seyfert galaxies).

In conclusion, knowing how the spectral index and the temperature change one can know if ℓ_s is bound to follow the variation of ℓ_h. This is extremely important, as we can test models in which an important role is played by reprocessing of the high energy radiation by cold matter located nearby the hot gas.

3.3.3 Comparison with observations

One of the main results of previous studies of hot pair plasmas is that the maximum compactness allowed by pair equilibrium decreases as the temperature increases. This however refers to sources with *fixed* spectral index, which roughly corresponds to fixed ℓ_h/ℓ_s.

The spectral behaviour of a varying X–ray source depends on whether the ratio ℓ_h/ℓ_s or ℓ_s remains constant when ℓ_h varies. If ℓ_h/ℓ_s is constant, the spectral index slightly steepens for increasing hard compactness and the temperature decreases. If ℓ_s remains constant, the spectral index flattens for increasing ℓ_h and the temperature decreases by a larger amount.

Observationally, as discussed in Chapter 1, there are indications that during large variations of the X–ray flux the X–ray spectral index remains approximately constant (e.g. Nandra et al. 1991), or slightly steepens (e.g. Yaqoob & Warwick 1991). This indicates that ℓ_h/ℓ_s is nearly constant during variations, strongly favoring models in which the soft component is dominated by the reprocessed flux (see e.g. Haardt & Maraschi 1991, HM93 and Chapter 4). This in turn would imply the presence of cold matter [cloudlets (Celotti et al. 1992; Sviron & Tsuruta 1993) or a cold accretion disk (Lightman & White 1988; Pounds et al. 1990; George & Fabian 1991; MPP)] very close to the illuminating X–ray source. Moreover, as can be seen from Fig. 2, the "canonical" value $\alpha_x \simeq 1$ roughly corresponds to a ratio ℓ_h/ℓ_s between 2 and 4, according to the absolute value of the compactness. In the next Chapter I will discuss which kind of geometry can give rise to the observed hard–to–soft ratio, and then in turn to the observed power law index. In any case the above conclusions do not depend strictly on the importance of pairs, which instead can fix the temperature and the temperature change during variations of the source.

An interesting result is the possibility to test the importance of pairs in the cooling processes using observations of spectral variability. As an example, Fig. 3 shows OSSE

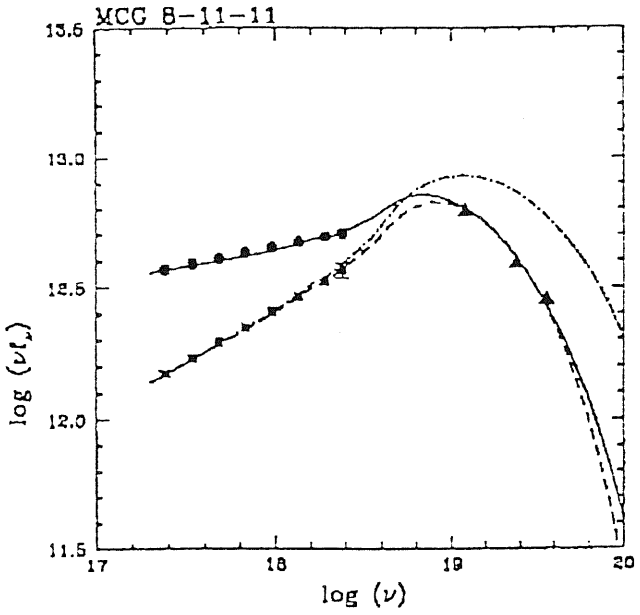

Fig. 3: The flattest and the steepest EXOSAT spectra of MCG+8 − 11 − 11 are shown together the with the OSSE data (Phase 1). The solid curve represents a model fitting the steep X-ray spectrum (i.e. steep photon index) and the OSSE data. The predicted γ-ray spectra corresponding to the flat X-ray case are shown as a dashed curve (pair-dominated source) and as a dot-dashed curve (Compton-cooled source).

data of the MCG+8 − 11 − 11 together with the flattest and steepest X–ray spectra observed with EXOSAT. As in the case of NGC 4151 and IC 4329A the maximum power is emitted around 100 keV. It appears that the X–ray emission varies with a pivoting point in the hard X–ray range. Along with the data, Fig. 3 shows the prediction of the pair–dominated model as discussed here and that of a simpler Compton–cooled model, i.e., assuming that the opacity is constant and is not related to the luminosity through pair production. The latter model may represent a case in which the opacity is mainly due to normal plasma. We assumed that OSSE data correspond to the steeper X–ray

spectrum (solid line, upper spectrum in Fig. 3). In the pair–dominated case a greater temperature would result in an increased compactness violating pair equilibrium. The equilibrium temperature must therefore be slightly lower (see Fig. 2) resulting in an almost identical emission in the OSSE band. On the contrary, in the Compton–cooled case the spectrum corresponding to the flat X–ray state corresponds to a decreased cooling by soft photons, and hence must be characterized by a substantially larger temperature. It is apparent from comparison of the low and high temperature cases (dashed and dot–dashed lines, respectively) that simultaneous ASCA–OSSE observations would be of great importance [our proposed Phase 2 OSSE observation of MCG+8 – 11 – 11 is scheduled for August–September 1995]. Fig. 3 has been produced by G.Ghisellini and myself.

In conclusion, observations of the cut-off energy of the X–ray spectrum is of crucial importance to establish if a source is pair dominated, and directly yield an upper limit on the compactness as illustrated in Fig. 1. In addition, if variations of the the flux corresponds to variations of the high energy cut-off as illustrated in Fig. 2, we can derive the compactness of the source, not only an upper limit, and therefore the size of the emitting region.

If a class of sources, such as Seyfert galaxies, are pair dominated with similar compactnesses there should be a correlation between spectral index and temperature. In the range of compactness between 10 and 100 steeper spectra should correspond to larger temperatures. For $\ell_h = 100$ the maximum temperature is 70, 220 and 450 keV for spectral indices $\alpha_x = 0.5$, 1 and 1.5, respectively.

At present, only two Seyfert galaxies have their spectral index and cut–off energy reliably measured, i.e. NGC 4151 and IC 4329A, and it is encouraging that the differences in their α_x and kT are in the sense discussed here. NGC 4151 has $\alpha_x = 0.5$ and $kT \sim 50$ keV (Maisak et al. 1993), while IC 4329A has $\alpha_x \sim 1$ and $kT \simeq 300$ keV (Zdziarski et al. 1994).

3.4 Quasi–thermal plasmas

We have seen that the steep spectra observed by OSSE can be interpreted on the basis of a thermal model, in which X–rays are due to multiple IC scatterings. In these models a strong constraint is due to the requirement of pair equilibrium (pair production balances annihilation and escape), which limits the possible temperature to a narrow range, which is weakly dependent on the compactness of the source (see Fig. 1). The resulting equilibrium temperature, for ℓ_h = 10–1000, is of the order of 50–100 keV, which is tantalizingly close to the derived value from OSSE data.

However, thermal models have been previously criticized as the root cause of the high energy spectrum of AGN, mainly because of the long thermalization time needed at high temperatures. Observed X-ray variability timescales are often so short, indeed less than the inferred 2-body thermalization timescales, that doubt is cast on the possibility that the plasma can be described by a Maxwellian distribution. There are therefore significant problems with thermal models for the hard X-ray spectra.

3.4.1 Thermal vs non–thermal Comptonized spectra

Guilbert et al. (1982) have shown that rapidly variable sources radiating near their efficiency limit cannot have temperatures greater than 22 keV if the heating is due to ion–electron collisions. Furthermore, thermalization of high energy electrons requires a time which is an increasing function of the temperature, at least for two body interactions (Spitzer 1956, Stepney 1983).

At high temperatures, the electron–electron thermalization timescale, t_{ee}, can be longer than the Compton cooling timescale, t_{IC}, with the consequence that the particle distribution deviates from thermal starting from the highest energies. We can calculate when the deviations from a pure thermal distribution are important by comparing t_{IC} with t_{ee}.

The relativistic form of eq[3.3] reads

$$t_{IC} \simeq \frac{< E >_{Maxw}}{< \dot{E} >_{Maxw}} = \frac{mc^2}{\sigma_T c U_{rad}} \frac{3\Theta(3\Theta+1)/(3\Theta+2)}{(16\Theta^2+4\Theta)} \tag{3.16}$$

where

$$U_{rad} \simeq \frac{9(L_h+L_s)(1+\tau/3)}{16\pi R^2 c} \simeq \frac{9mc^2\ell_h(1+\ell_s/\ell_h)(1+\tau/3)}{16\pi\sigma_T R} \tag{3.17}$$

We checked that $U_{rad} \simeq 9L/16\pi R^2 c$ instead of the usual $U_{rad} \simeq L/4\pi R^2 c$ is a better match to Montecarlo results for a spherical source.

In Comptonization models, the y parameter controls the efficiency of the radiative cooling, allowing the scattering optical depth τ (from which t_{ee} depends) to be expressed in terms of the ratio of the hard to soft photon compactnesses, ℓ_h/ℓ_s. Assuming a fixed ratio of the hard to soft photon compactness allows to relate the scattering optical depth τ to the dimensionless electron temperature Θ:

$$\frac{\ell_h}{\ell_s} \simeq \frac{2}{3}[\exp(y)-1]; \qquad y \simeq (\tau+\tau^2)(16\Theta^2+4\Theta) \tag{3.18}$$

The electron–electron thermalization time–scale is (Stepney 1983)

$$t_{ee} \simeq \frac{R/c}{\tau \ln\Lambda} f_{ee}(\Theta)$$

where

$$\begin{aligned} f_{ee}(\Theta) &\simeq 4\sqrt{\pi}\Theta^{3/2}; \qquad \Theta \leq \pi/4 \\ f_{ee}(\Theta) &\simeq 8\Theta^2; \qquad\quad \Theta \geq \pi/4 \end{aligned} \tag{3.19}$$

Imposing $t_{ee} = t_{IC}$ we obtain

$$\ell_h \simeq \frac{4\pi}{3} \frac{\ln\Lambda}{(1+\ell_s/\ell_h)} \frac{\tau}{(1+\tau/3)} \frac{(3\Theta+1)}{(3\Theta+2)(4\Theta+1)f_{ee}(\Theta)} \tag{3.20}$$

For the electron–proton interaction timescale, the equation reads the same, but now $f_{ep}(\Theta)$ is given by (from eq[4.4] of Stepney 1983)

$$f_{ep}(\Theta) \simeq 2\sqrt{\pi}\frac{m_p}{m_e}\Theta^{3/2} \tag{3.21}$$

We obtain a relation between ℓ_h and the dimensionless electron temperature Θ: for any given Θ, there is a maximum ℓ_h for which $t_{ee} < t_{IC}$. We compared this requirement with the ℓ_h–Θ relation appropriate for steady thermal sources in pair balance (see Fig. 1 in Ghisellini et al. 1993) and we concluded that sources at the pair balance limit, if thermal, require an energy exchange mechanism more efficient than 2–body interactions. As a consequence, it is not clear if the plasma can be described as thermal during rapid variations.

However, if the radiation mechanism is multiple Compton scattering, the overall photon spectrum is made by many overlapping scattering orders and its shape is insensitive to the detailed form of the particle distribution. To show this we compared the spectra obtained by Comptonization of soft photons, distributed as a blackbody at the temperature $kT_{BB} = 50$ eV, by a plasma with different particle distributions. All the used particle distributions yield the same number density and the same value of $< \gamma^2 - 1 >$, so that the average photon energy gain per scattering is the same.

It can be seen (see Fig. 2 of Ghisellini et al. 1993) that the overall spectra are almost indistinguishable. The only slight difference is at low energies, roughly corresponding to the first two scatterings (Fig. 4). In fact the seed photons for the first scattering are narrowly distributed, so that the differences among the various distributions can emerge. For higher order scatterings, the incident photon distributions are broader, making the scattered photon spectra more similar.

3.4.2 Quasi thermal pair cascade

Here I show that intense and repeated heating of a compact emission region results in a pair–rich particle distribution which in turn yields a quasi–thermal emergent photon spectrum (Ghisellini et al. 1993).

We followed the treatment of Done et al. (1990, see also Cavaliere 1982 and Svensson 1987) by assuming that throughout the source energetic particles are injected mo-

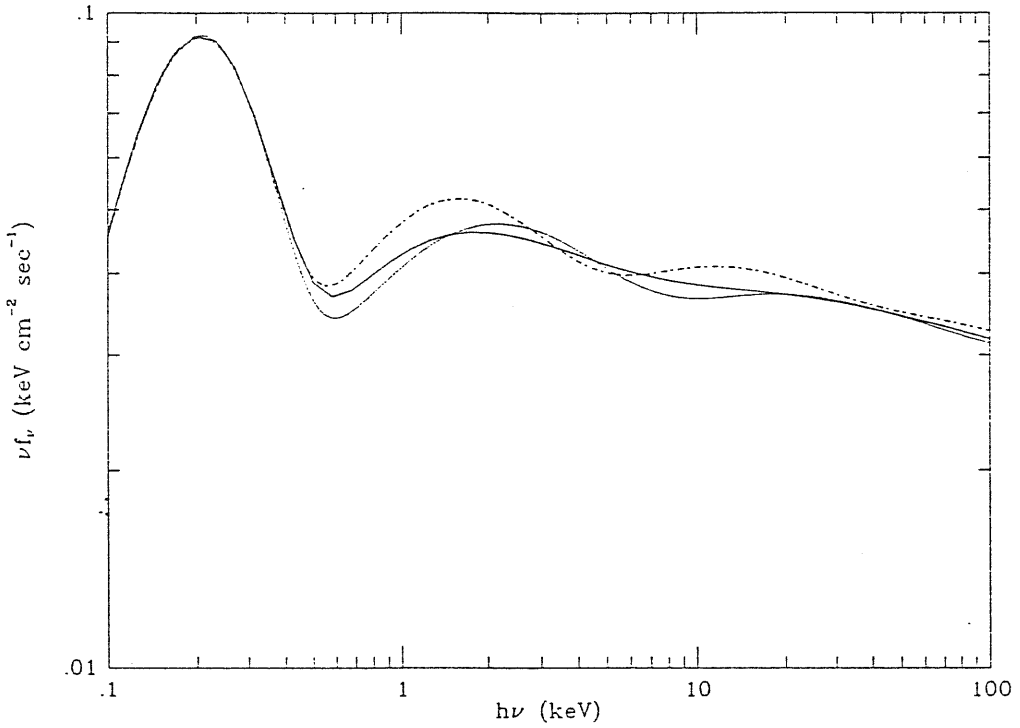

Fig. 4: Comptonization spectra computed using the formalism of Chapter 2 assuming different electron distributions. Solid line: thermal distribution, with $kT = 171$ keV; dashed line: power law distribution, $N(\gamma) \propto \gamma^{-2}$, with $1 < \gamma < 3$; dashed–dotted line: $N(\gamma) = const$, with $1 < \gamma < 2.37$. All models have the same $\tau = 0.35$.

noenergetically at some Lorentz factor γ_0 at a rate corresponding to a hard compactness ℓ_h. Soft (UV) photons are injected at a rate corresponding to a compactness ℓ_s, with a blackbody spectrum of temperature kT_{BB}. The injected particles cool by Compton scattering. Below a critical γ_c particles interact mainly because of Coulomb collisions joining a thermal distribution at some temperature kT, and eventually part of them annihilate, while the remaining are re–accelerated back to γ_0 and re–injected. We assumed that the plasma is pair dominated, i.e. that pairs outnumber protons, and that the plasma is in pair equilibrium, i.e. the rates for pair creation and pair annihilation balance. We also assume that the re–accelerator operates on all particles, once cooled,

on the timescale t_{acc}. The re–acceleration process takes particles of $\gamma \sim 1$ and re–injects them at γ_0. The re–acceleration time is taken to be equal to t_{IC} which in turn is calculated assuming cooling by Compton scattering and Coulomb collisions. In other words, we require that the pairs can cool before being re–accelerated.

The critical value γ_c is computed solving the kinetic equation:

$$\dot{\gamma}_{CC} = \dot{\gamma}_{IC} \tag{3.22}$$

The left–handed term represents the energy variation of particles due to Coulomb collisions, while the right–handed term is the energy variation of particles due to Compton cooling.

The steady state particle distribution is computed imposing number and luminosity conservation. Number density conservation of particles is expressed by

$$\dot{n}_{inj} + \dot{n}_{\gamma\gamma} + \dot{n}_{esc} + \dot{n}_a = 0 \tag{3.23}$$

where I have included contributions from injection, pair production, escape and pair annihilation, respectively. They are given by

$$\begin{aligned}
\dot{n}_{inj} &= \frac{c}{\sigma_T R^2}\frac{3}{4\pi}\frac{\ell_h}{\gamma_0 - 1} \equiv Q_0 \\
\dot{n}_{\gamma\gamma} &= \frac{c}{\sigma_T R^2}\frac{3}{4\pi}\xi\ell_h \\
\dot{n}_{esc} &= -\frac{c}{\sigma_T R^2}\tau\beta_{esc} \\
\dot{n}_a &= -\frac{c}{\sigma_T R^2}\frac{3}{4\pi}\tau^2 f(\Theta)
\end{aligned} \tag{3.24}$$

where $f(\Theta)$ is the dimensionless annihilation rate (eq[3.12]). ξ is the pair yield, i.e., the ratio of the luminosity in pair rest mass to the total injected luminosity. The pair yield measures the efficiency of the source to convert the injected power in pair rest mass.

Working out the above equations we obtain

$$\frac{4}{\pi}\tau^2 f(\Theta) + \frac{16}{3}\tau\beta_{esc} - \frac{4}{\pi}\ell_h\left(\xi + \frac{1}{\gamma_0 - 1}\right) = 0 \tag{3.25}$$

where here τ represents the scattering optical depth *due to thermalized particles only*, i.e.,

$$\tau = N(\gamma)\sigma_T R = N_0 \sigma_T R \int_1^{\gamma_0} d\gamma\, \gamma \sqrt{\gamma^2 - 1}\, \mathrm{e}^{-\gamma/\Theta} \tag{3.26}$$

For the pair yield we have fitted the results by Done & Fabian (1989), deriving the following approximated expression valid for $\ell_h \geq \ell_s$:

$$\xi = 0.01 \left(\frac{\gamma_0}{10}\right)^3 \left(\frac{\ell_h}{\ell_s}\right)^{1/2} \min[(\ell_h/30), 1] \tag{3.27}$$

This is a crude approximation to the exact pair yield, but is sufficient for our scope, since the dependence of the equilibrium γ_0 on ξ is weak. It is correct within few percent for $1 \lesssim \gamma_0 \lesssim 10$.

Finally the assumption of pair equilibrium links the cold particle opacity to the other physical parameters (e.g. Svensson 1987):

$$\tau = \sqrt{\frac{64}{9}\beta_{esc}^2 + \frac{4}{\pi}\ell_h[\xi + 1/(\gamma_0 - 1)]} - \frac{8}{3}\beta_{esc} \tag{3.28}$$

The above eq[3.25] and eq[3.28] suffice to solve for the equilibrium values of τ, γ_0. The resulting scattering optical depth of the relativistic particles is found to be equal to τ, making the total depth equal to twice τ. This is implicit in the assumption $t_{acc} = t_{IC}$.

Once we know γ_0 and τ, we derive the particle distribution assuming cooling by Compton scattering and by Coulomb collisions. At low energies, the latter process establishes a Maxwellian distribution, whose temperature is derived by balancing the heating due to Coulomb collisions of relativistic particles with the cooling due to thermal Comptonization. We require the conservation of the injected luminosity, balancing the different terms contributing to the particle energy spectrum, i.e.,

$$L_{tot} = L_{pl} + L_{Maxw} + L_{esc} \tag{3.29}$$

The three contributions to the total luminosity are the luminosity in cooling particles (forming a power law distribution), the luminosity in thermalized particles (forming

a Maxwellian distribution) and the luminosity lost because of escaping particles. The total available luminosity is

$$L_{tot} = Q_0 V(\gamma_0 - 1)m_e c^2 \tag{3.30}$$

assuming electron injection. V is the source volume. The luminosity in the power law energy spectrum can be written as

$$L_{pl} = V m_e c^2 \int_{\gamma_c}^{\gamma_0} d\gamma \dot{\gamma}_{IC} N(\gamma) = Q_0 V m_e c^2 \int_{\gamma_c}^{\gamma_0} d\gamma \frac{\dot{\gamma}_{IC}}{\dot{\gamma}_{IC} + \dot{\gamma}_{CC}} \tag{3.31}$$

while the luminosity available in the Maxwellian:

$$L_{Maxw} = \frac{2}{3}(e^y - 1)L_S \tag{3.32}$$

Here L_S is the luminosity injected as a soft photon input. The escaping luminosity can be estimated as

$$L_{esc} = V m_e c^2 \int_1^{\gamma_0} d\gamma \dot{(}\gamma - 1)n_{esc} = \frac{V m_e c^2 N_0}{t_{esc}} \int_1^{\gamma_0} d\gamma\, \gamma\sqrt{\gamma^2 - 1}(\gamma - 1)\mathrm{e}^{-\gamma/\Theta} \tag{3.33}$$

Now inserting eq[3.30], [3.31], [3.32] and [3.33] into eq[3.29] we can solve for the Compton paramter y:

$$y = \ln\left[1 + \frac{\ell_h}{\ell_s}\left(1 - \frac{\int_{\gamma_c}^{\gamma_0} d\gamma \frac{\dot{\gamma}_{IC}}{\dot{\gamma}_{IC}+\dot{\gamma}_{CC}}}{\gamma_0 - 1}\right) - \frac{4\pi}{3}\frac{\tau\beta_{esc}}{\ell_s}\langle\gamma - 1\rangle\right] \tag{3.34}$$

and then compare the above eq[3.34] with the definition of y:

$$y = \frac{4}{3}\langle\gamma^2 - 1\rangle\tau(\tau + 1) \tag{3.35}$$

obtaining a single equation for Θ.

The two averages in eq[3.35] are performed over the Maxwellian distribution and can be expressed in terms of modified Bessel functions:

$$\begin{aligned} \langle\gamma - 1\rangle &= 3\Theta + \frac{K_1(1/\Theta)}{K_2(1/\Theta)} - 1 \\ \langle\gamma^2 - 1\rangle &= \frac{12\Theta^2 K_2(1/\Theta) + 3\Theta K_1(1/\Theta)}{2\Theta K_1(1/\Theta) + K_0(1/\Theta)} \end{aligned} \tag{3.36}$$

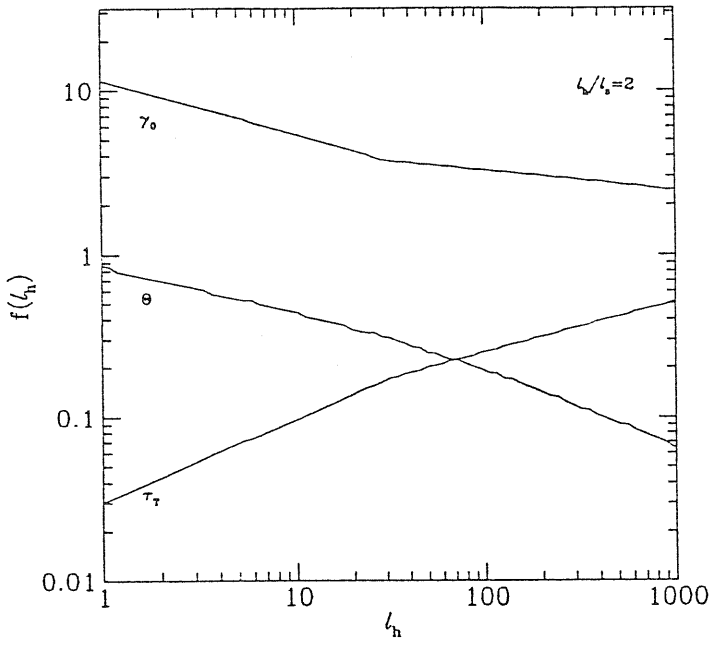

Fig.5: Three parameters of the plasma cloud are shown as functions of the cloud compactness ℓ_h: the maximum Lorentz factor γ_0, the temperature of the thermalized particles Θ and their resulting scattering opacity τ. The cooling is provided by a soft photon input described by a compactness ℓ_s so that $\ell_h/\ell_s = 2$.

In eq[3.31] I used the following expressions for $\dot{\gamma}_{IC}$ and $\dot{\gamma}_{CC}$ (Ghisellini 1987):

$$\begin{aligned} \dot{\gamma}_{IC} &= \frac{1}{3\pi}\frac{\ell_h+\ell_s}{R/c}\left(\frac{1+\tau}{3}\right)(\gamma^2-1) \\ \dot{\gamma}_{CC} &= \frac{3}{4}\frac{\tau}{\beta_{esc}}\frac{1}{R/c}\left[53.6+\ln\left(\gamma\frac{R_{15}}{\tau}\right)\right] \end{aligned} \tag{3.37}$$

where $R_{15} \equiv (R/10^{15}\mathrm{cm})$.

In the cases studied here the equilibrium Θ is found to be always greater than the Compton temperature. This is because of the large energy exchange between relativistic and thermal particles. In other words, Coulomb collisions between the two populations of particles is a more efficient process than the heating due to the collisions of cold

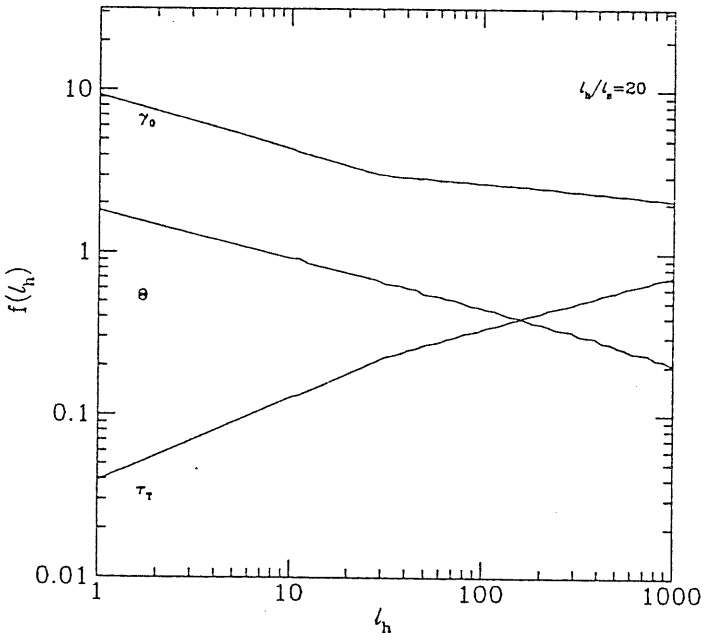

Fig. 6: Same as Fig. 5, but $\ell_h/\ell_s = 20$.

particles with high energy photons. At high energies there is a tail of quasi power–law shape, resulting from injection and cooling, calculated by the continuity equation.

In Fig. 5 and Fig. 6 the values of γ_0, τ and Θ are shown as a function of ℓ_h for two different values of ℓ_h/ℓ_s. The case $\ell_h/\ell_s = 2$ is roughly what it is expected if the X–rays originate in an accretion disk corona (see next Chapter), while the case $\ell_h/\ell_s = 20$ can represent a photon starved source. The most important thing to notice is the always small value of the maximum electron energy, which ensures that the resulting Comptonized photon spectrum is fairly similar to what is formed in the thermal case. Moreover, as expected, the average energy per particle decreases (both in the Maxwellian and in the power law distribution) and the particle density compactness increases. For a fixed value of ℓ_h, Θ and τ are greater in the photon starved case, while γ_0 is lower.

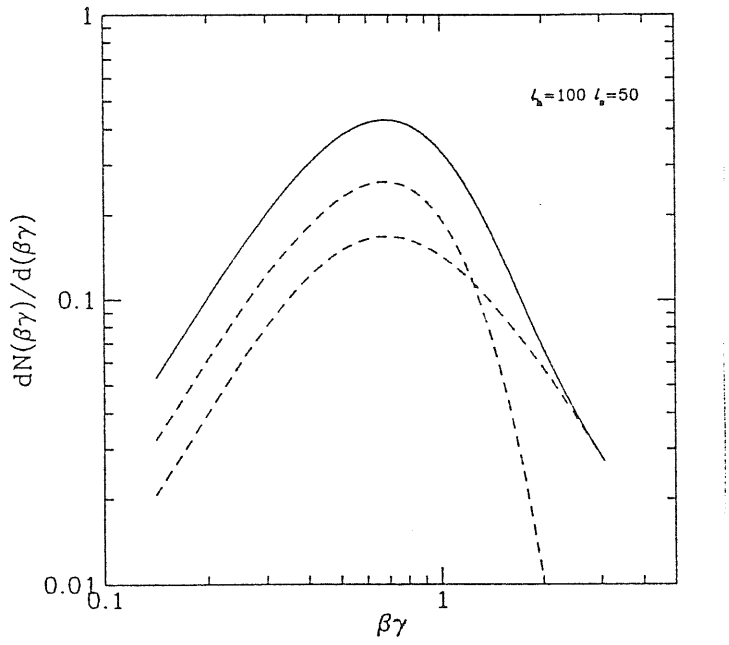

Fig. 7: The particle momentum distribution for $\ell_h = 100$ in the case $\ell_h/\ell_s = 2$. The solid line is the total distribution. The Maxwellian and the power law parts of the distribution are shown also separately (dashed lines).

This is due to the reduced cooling that makes the Coulomb collisions more effective in forming the Maxwellian distribution

In Fig. 6 and Fig. 7 I show examples of the resulting particle momentum distribution ($\ell_h = 100$ and $\ell_h/\ell_s = 2$ and 20). The particle distribution is the sum of a Maxwellian and a cooling power law. In the cases shown here the temperature of the Maxwellian electrons is $\Theta \simeq 0.2$ (0.46 for $\ell_h/\ell_s = 20$), the optical depth due to thermalized electrons is $\tau \simeq 0.25(0.34)$, and the maximum electron Lorentz factor (in the power law) is $\gamma_0 \simeq 3.23(2.7)$.

In conclusion, we gave reasons why the emitting particle energies extend to low values and we calculated in a self consistent way the expected spectrum. This has

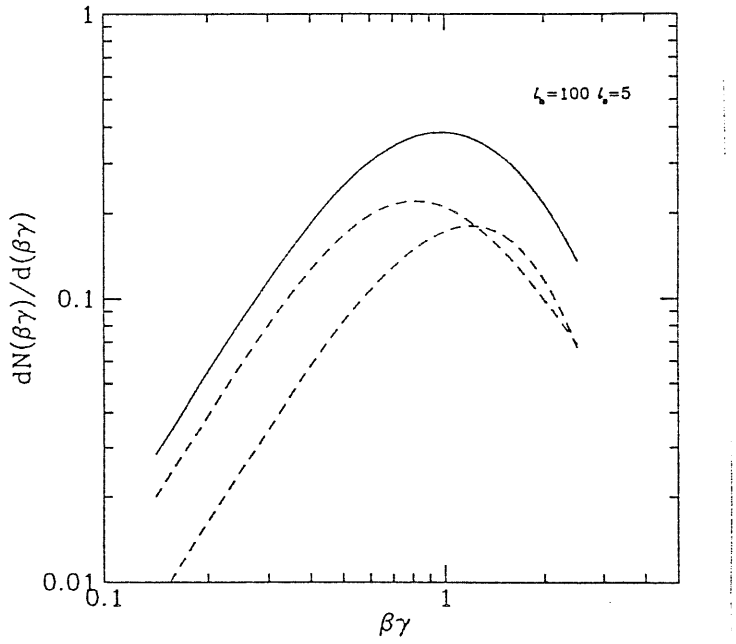

Fig. 8: Same as Fig. 7, but $\ell_h/\ell_s = 20$.

been achieved by assuming a mechanism which re–injects particles, once cold, at some given energy $\gamma_0 m_e c^2$. If γ_0 is initially large, particles emit γ–rays which in turn create pairs, which are then re–accelerated. Assuming that the injected power is constant, the increased number of particles to be re–accelerated means that γ_0 decreases. Equilibrium is reached for $\gamma_0 \sim$ a few, when pair creation balances annihilation so that a constant number of particles is re–accelerated. The equilibrium value of γ_0 is a few, and only weakly dependent on the compactness. With this hypothesis I have derived the entire equilibrium particle and photon distributions, which (as in completely thermal plasmas) are functions only of the compactness of the source.

Our results show what happens if acceleration/heating continues in the emission region and involves *all* the particles present. Standard non–thermal models calculate the

spectrum resulting from a region in which only a small and constant number of particles are accelerated and cool despite the fact that pair production increases the total number of particles present. Standard thermal models assume that all particles are heated and maintained in a Maxwellian distribution at constant temperature (which depends on the particle density), despite the rapid variations in luminosity that are observed. Our model lies between these extremes, since it responds to the varying particle density and allows the particles both to cool and to be non–thermal.

The re–acceleration mechanism here proposed assumes that the plasma is pair dominated. If ambient 'normal' plasma is also present, then the number density of re–accelerated particles would be greater than in the case here studied. Consequently the equilibrium γ_0 would be smaller. The values given here can then be considered as the maximum possible γ_0 at a given compactness. In this sense our results are very similar to the classical results of completely thermal plasmas, where for a given compactness there exists a maximum allowed temperature.

We have also assumed that the re–acceleration mechanism operates on cool particles. In the case of heating of hot particles, the resulting distribution is bound to peak at the energy where heating and cooling balances. Again, if pair equilibrium is required, this energy is small. The exact shape of that distribution depends on the details of the energy exchange process among particles in the peak. But, as shown in Fig. 4, the photon spectrum is very weakly dependent on the exact shape of the particle distribution, as long as the maximum particle energy is small.

Finally, we have checked that the pair yield is always $\ll 1$, making the annihilation line invisible. This has been confirmed by detailed calculations of the emitted spectrum performed by Coppi (1993, private communication).

Chapter 4

Two Phase Models

"TALKING TO YOU IT'S LIKE CLAPPING WITH ONE HAND." – ANTHRAX

4.1 Introduction

In the previous Chapter we have seen that thermal or quasi–thermal mild–relativistic plasmas can explain the main features of the X–ray emission from AGNs. The canonical spectral index $\alpha_x \simeq 1$ implies that the ratio ℓ_h/ℓ_s has values in a narrow range in different sources, while spectral variability seems to indicate that this ratio remains almost constant during variations of the high energy flux in single sources.

Here I discuss a model based on thermal Comptonization, in which a thermal balance equation is introduced for the hot electrons. These are thought to be located immediately above the cold reflecting matter so that the soft blackbody photons emitted by the cold layer provide the main source of cooling for the hot electrons. At the same time the hard photons produced by Compton scattering are an important source of heating for the underlying cold layer which reprocesses them into soft photons.

It is intuitive to predict qualitatively that in such a "balanced" situation the electron temperature will adjust so as to maintain comparable luminosities in the soft and hard components, independently of the optical depth of the hot electrons and of the total luminosity of the source. Thus the model can potentially account for a "universal" spectrum. We will assume that a significant fraction of the gravitational power is dissipated in the hot tenuous layer. This hypothesis may be thought to represent an

accretion disk plus corona system in which the accretion power is dissipated via magnetic processes directly in the corona. In the last part of the Chapter I will discuss in a model for formation of a structured active corona above an accretion disk.

In this Chapter I discuss the subject mainly on the ground of radiative processes and spectral emission mechanisms. Recently Svensson & Zdziarski (1994) calculated in some details the dynamics of a corona–accretion disk system, and the interest reader should refer to their paper, and to references therein.

Part of the content of the present Chapter has been worked out by L.Maraschi, G.Ghisellini and myself (Haardt and Maraschi 1991, HM93; Haardt et al. 1994).

4.2 X–rays from extended coronae

4.2.1 Model outline

I consider the simple idealized case of two homogeneous isothermal layers in a plane parallel geometry. Such a configuration can model an accretion disk with an active corona located above it. A fraction f of the gravitational power P_G is assumed to be directly dissipated in the hot phase of optical depth τ. The rest $(1-f)P_G$ is emitted as local thermal flux by the cold layer. The hot phase is assumed to be tenuous so that the main cooling mechanism is IC emission.

The total luminosity radiated in all directions by the hot phase can be expressed as AL_S where A is the amplification factor due to Comptonization and L_S is the total soft photon luminosity emerging from the cool phase. The hard luminosity added by the Compton process is $L_H = (A-1)L_S$. The hard luminosity L_HC can be broken down into the upward and downward components

$$L_H = L_{uH} + L_{dH}, \tag{4.1}$$

and L_{dH} can be expressed as ηL_H, where the parameter η is a measure of the anisotropy of the IC emission from the corona, $\eta = 0.5$ representing a perfectly isotropic case.

Hard photons directed downwards are partly absorbed and partly reflected by the optically thick underlying layer (Lightman & White 1988, and Guilbert & Rees 1988).

The reflected luminosity can be written as $L_{rfl} = aL_{dH}$, where a is the energy integrated disk albedo, and will add to the upward emitted flux. The absorbed photons will be reprocessed in the cold layer and re–emitted as thermal radiation. Therefore $(1-a)L_{dH}$, will contribute to L_S.

Of course part of the reflected photons suffers further scatterings in crossing the corona. The scattering of the reflected component as a source of further cooling for the hot electrons has been neglected, as the energy density of this component is $\simeq 10\%$ of those of the soft photon input.

The above considerations can be summarized in the following two equations:
Energy balance for the cold phase:

$$(1-f)P_G + (1-a)L_{dH} = L_S \tag{4.2}$$

Energy balance for hot phase:

$$fP_G + L_S = AL_S \tag{4.3}$$

From the energy balance equations we obtain the black body and the Compton luminosities as fractions of the total gravitational power P_G:

$$L_S = (1 - f + f\eta - fa\eta)P_G \tag{4.4}$$

and

$$L_H = fP_G \tag{4.5}$$

We note that the total available power can be written as

$$P_G = L_H + L_S \tag{4.6}$$

where the "Comptonized luminosity" L_C is defined as

$$L_C = fP_G[1-\eta(1-a)] = L_H[1-\eta(1-a)] \tag{4.7}$$

This quantity represents the actual IC luminosity radiated away from the two phase system.

The ratio between the two components of the luminosity, L_S and L_H, does not depend on the actual power of the source. This ratio fixes the amplification factor A required by the balance equations:

$$L_H/L_S = f/(1-f+f\eta-fa\eta) = (A-1) \tag{4.8}$$

Eq[4.8] represents the first important result of the model, which leads to similar broad band spectra for a wide range of powers. It can be written in terms of the observed hard luminosity as:

$$L_H/L_S = (A-1-f)/f \tag{4.9}$$

For low f the amplification factor is simply $\sim 1+f$, and the actual values of a and η are irrelevant. In this case the luminosity from the hot corona is small compared to the thermal luminosity of the thick phase, the coupling between the two phases is unimportant and the present treatment unnecessary.

Observationally however a large fraction of the bolometric luminosity is in the hard component supposedly associated with the hot phase. This corresponds to values of f approaching unity, that is to the bulk of the gravitational power being dissipated in the corona. We have then

$$(A-1) = 1/[\eta(1-a)] \tag{4.10}$$

In order to derive the physical parameters of a corona which satisfy the above equation, we need to express A, η and a as a function of τ and Θ through the theory of Comptonization. Although the albedo from the cold phase at a given energy does not depend on the coronal parameters, the value of the integrated albedo depends on the incident spectrum and therefore on τ and Θ.

It is worth noting that the spectral index of the Comptonized spectrum can be written as ($\tau \ll 1$)

$$\alpha_x \simeq \frac{-\ln \tau}{-\ln \tau + \ln y} \tag{4.11}$$

where y is the Compton parameter defined in the previous Chapter 3 (eq[3.18] or eq[3.35]). Since the model fixes an amplification ratio $A \simeq 3$ the standard approximation of Comptonization (e.g. Rybicki & Lightman, 1979) implies $y \simeq 1$, which leads to a spectral index close to 1 and largely independent of τ. This result is of interest for understanding how the model works.

4.2.2 Solution of the balance equations

A detailed discussion of the solution of the balance equations is in HM93. Here I summarize the main results.

An important feature of the model is the difference between forward and backward scattering. As discussed in §[4.2.1], the ratio L_H/L_S, or equivalently $A-1$ (referring to the amplification factor), η and a can be expressed through rather complex formulae in terms of τ and Θ. The only other physical parameter entering the balance eq[4.8] is the black body temperature, T_{BB}, which however appears only implicitly, through the dependence of the Comptonized spectra. This dependence is very weak. We will therefore consider T_{BB} as a fixed parameter in the solutions.

It is worth to repeat that eq[4.8] contains only the ratio L_H/L_S, so that its solution is a relation between τ and Θ, which holds for any value of the actual luminosities L_H and L_S. Since the absolute value of the luminosity is arbitrary, we can scale the other physical parameters to be consistent with a chosen value of T_{BB}. Assuming that the absorbed fraction of the downward Compton luminosity, $(1-a)L_{dH}$, is simply reprocessed into black-body emission and that the cold phase is isothermal, the soft radiation temperature can be related to the physical parameters of the system, namely the mass of the central object, the characteristic dimensions of the emitting region and

the soft/hard luminosity of the source. For a central object of mass $M = M_8 10^8 M_\odot$ and an emitting region of dimension $R = r(2GM/c^2)$, the black body temperature is given by

$$kT_B B \simeq 50 \times M_8^{-0.25} \times r^{-0.5} \times [\eta(1-a)]^{0.25} \times (P_G/L_{Edd})^{0.25} \ \ [\mathrm{eV}] \qquad (4.12)$$

where L_{Edd} is the Eddington luminosity.

Assuming the X-rays to be produced inside $r = 7$ with critical luminosity and $\eta(1-a) \simeq 0.5$, $kT_{BB} \sim 50$ eV corresponds to $10^6 M_\odot$, while $kT_{BB} \sim 5$ eV corresponds to $10^{10} M_\odot$. For luminosities subcritical by a factor p the mass range is shifted down by the same factor. We therefore choose these two values of kT_{BB} as two representative extremes.

The solution of eq[4.8] for fixed kT_{BB} is obtained numerically, using a standard bracketing– bisection algorithm yielding $\Theta = \Theta(\tau)$. The results (for $f = 1$) are derived for the two values of the black body temperature discussed above, $kT_{BB} = 5$ eV and 50 eV, and for values of the optical depth τ ranging from 0.005 to 1.

The equilibrium temperatures are shown in Fig. 1 as a function of τ for the two cases. They range from 30 keV to 1.2 MeV and from 30 keV to 2 MeV, for $kT_{BB} = 5$ eV and 50 eV, respectively. The temperature obtained for the higher value of kT_{BB} is then slightly larger. This is due to the fact that the reflected luminosity is a larger fraction of the total luminosity, due to the higher minimum energy of the incident spectrum. As anticipated, the dependence on kT_{BB} is small.

It is interesting to compare the solution of eq[4.9] with the condition of a constant Compton parameter. The dashed line in Fig. 1 corresponds to the solution of the equation

$$(16\Theta^2 + 4\Theta)\tau = 0.6 \qquad (4.13)$$

For a slab like geometry the mean scattering probability for $\tau \ll 1$ is $\sim 2\tau$, so that the value of the Compton parameter is close to 1 for $\tau \lesssim 0.2$, while it tends to became lower as the optical depth is close to 1.

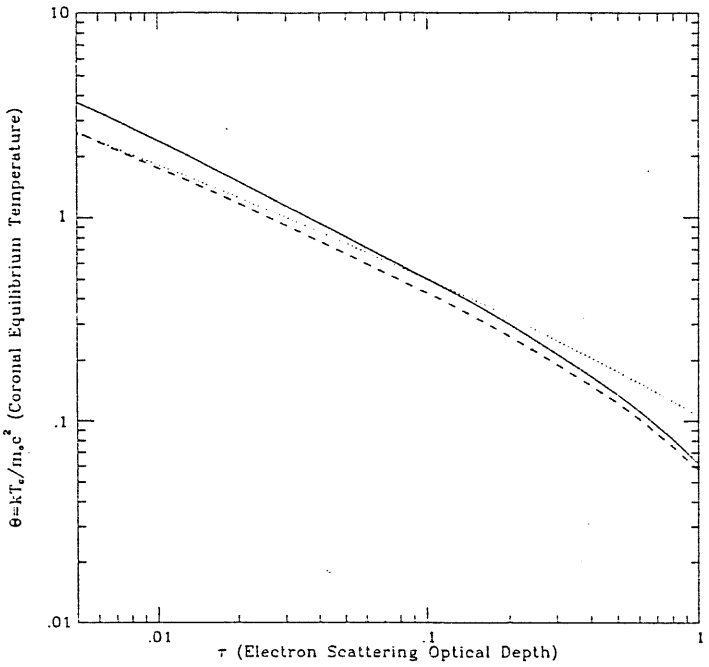

Fig. 1: Dimensionless equilibrium electron temperature Θ *of the hot phase vs. the electron scattering optical depth* τ*. The numerical solutions of the energy balance equation for* $kT_{BB} = 50$ *eV is represented as the solid line, while the dashed line is for* $kT_{BB} = 5$ *eV. The solution for a constant Compton parameter* $y = 0.6$ *is shown as a dotted line (from HM93).*

The values of the spectral index α_x are found to be in fairly agreement with observations for $\tau \lesssim 1$ (Fig. 2; see HM93 for a detailed discussion).

Note that for f significantly lower than 1, $A - 1$ is almost constant, since its value is driven by the constant f rather than by a and η (eq[4.8]). In this case however the amplification factor is smaller and the corresponding spectral indices would be larger than those reported in Fig. 2.

It is important to emphasize that the solutions discussed here depend only on the *total* value of τ and not on the origin of it. Therefore, even in the presence of $e^{\pm}$ pairs, the

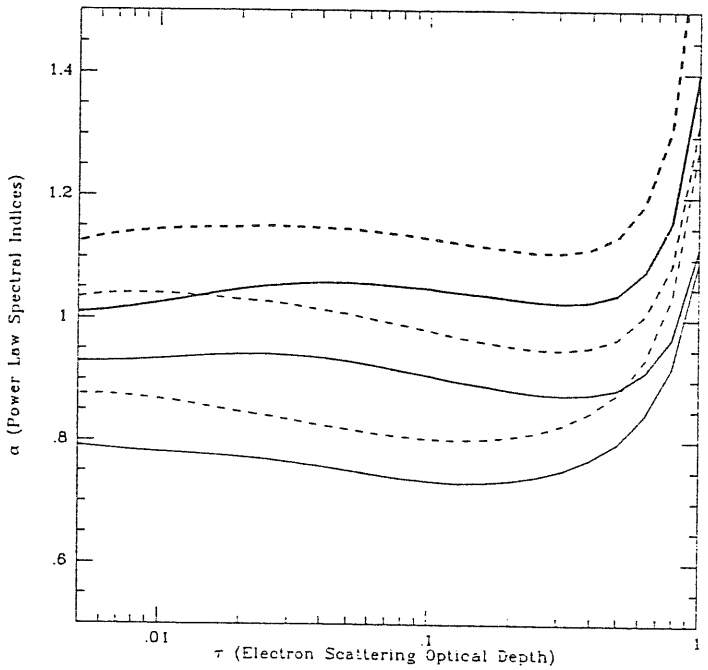

Fig. 2: Resulting spectral indices of the Comptonized component. Solid and dashed lines refer to solutions obtained with $kT_{bb} = 50$ eV and $kT_{BB} = 5$ eV, respectively. From top to the bottom, for each choice of the black body temperature: the average spectral index α_x, the mean index of the updriven Compton power law α_{up} and the spectral index α_{0deg} in the case of a face–on line of sight (from HM93).

solutions $\Theta(\tau)$ maintain their validity, but for each τ one should specify selfconsistently what are the corresponding values of $\tau_{e\pm}$ and τ_p. Clearly for low ℓ_h the contribution of pairs can be neglected and one has $\tau_p = \tau$. On the other hand, for high ℓ_h $\tau \gg \tau_p$ will yield a significantly lower temperature than computed in the absence of pairs. In order to find the constraints imposed by the presence of pairs we solved the pair balance equation as discussed in the previous Chapter. For fixed ℓ_h we derived the value of τ_p consistent with τ and Θ satisfying the balance equations.

Note that the mean energy of the soft photons can be related to the compactness

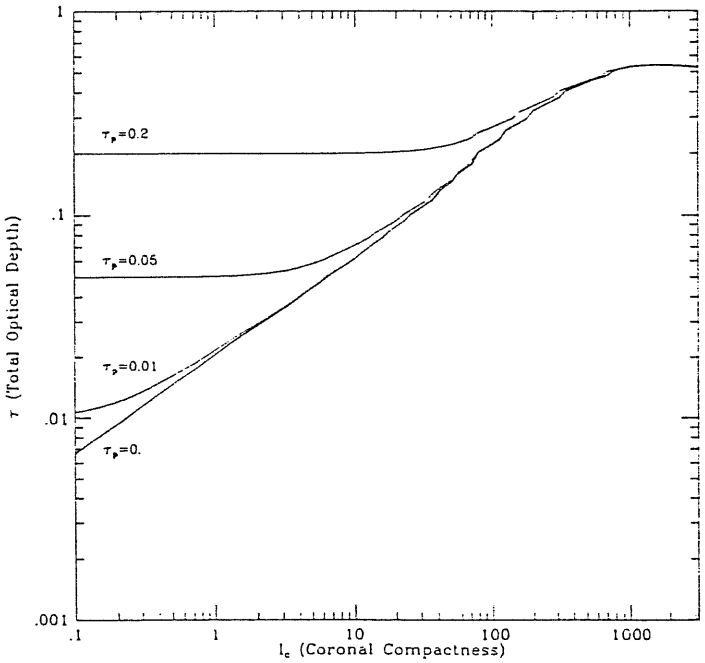

Fig. 3: Total optical depth τ as a function of the compactness ℓ_h and the original electron optical depth τ_p. The limiting curve is for a pure pair corona (from HM93).

through

$$kT_{BB} \simeq 5 \times M_8^{-0.25} \times h^{-0.25} \times [\eta(1-a)]^{0.25} \times \ell_h^{0.25} \quad [\mathrm{eV}] \tag{4.14}$$

We solved the equations with τ_p as parameter and ℓ_h as the independent variable, considering the variation of the black body temperature with compactness, according to eq[4.14]. This choice corresponds to a description in which the mass and size of the source are kept constant and the compactness varies due to a variation in luminosity. We consider a range of more than four orders of magnitude in compactness $10^{-1} < \ell_h < 3 \times 10^3$, corresponding to a variation of the black body temperature between 5 and 80 eV for $(M_8 h) \simeq 0.1$. Fig. 3 shows the total optical τ depth and Fig. 4 the equilibrium temperature Θ of the corona as a function of compactness ℓ_h for different choices of τ_p.

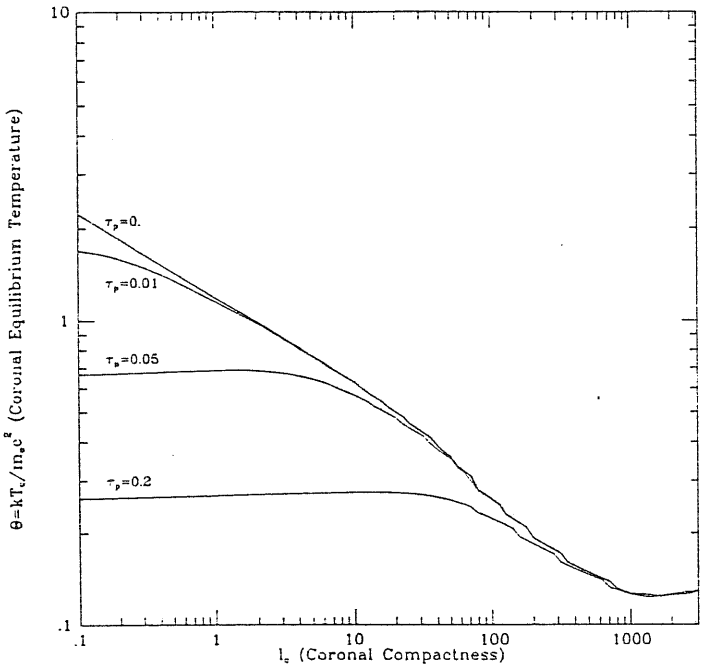

Fig. 4: The corresponding electron temperature according to the energy balance equation (from HM93).

For low ℓ_h pairs are not important and $\tau = \tau_p$ which may be taken as an independent parameter. This regime corresponds to the horizontal branches in Fig. 3 and Fig. 4. However in this regime free–free emission dominates over Compton cooling, and the equilibrium curves are different from those shown here (Svensson 1983).

For increasing compactness the opacity due to pairs becomes dominant and imposes an absolute lower limit to the optical depth and an absolute upper limit to the temperature. The limiting case corresponds to a pure pair plasma. Note that even for extremely high compactness, the total optical depth due to pairs is $\lesssim 0.5$. A different result was obtained by Z85 assuming a constant spectral index $\alpha_x = 0.7$. In the latter paper, for high compactness the optical depth was found to be $\gg 1$. In our case for low temperatures the radiation spectrum is steep ($\alpha_x \gtrsim 1.5$), and the number density

of Wien photons, which dominate the pair production for $\Theta \lesssim 0.2$, is low (see previous Chapter).

For moderately high compactness, $\ell_h \gtrsim 20$, the contribution of pairs alone yields optical depths larger than 0.1. Therefore the physical parameters of an optically thin corona are essentially determined by pair equilibrium.

4.2.3 Main results

The two phase model presented here can explain the canonical value of the spectral index observed in Seyfert galaxies, its roughly constant value during variation of the X–ray flux, the presence of a cut–off at 50–500 keV, as well as the reflection features observed below 20 keV.

The main result of the model is that the ratio between the IC luminosity from the optically thin corona and the soft thermal luminosity from the underlying opaque disk is fixed. This implies an almost constant Comptonization parameter of the order of 1. In our calculation we have found, for $\tau \lesssim 0.5$, $y = (16\Theta^2 + 4\Theta)\tau \simeq 0.6$. The energy spectrum of the IC component, averaged over positive angles, when approximated with a power law has, for a soft photon temperature of $kT_{BB} = 50$ eV, a spectral index $\alpha_x = 0.9 \pm 0.05$, largely independent of the optical depth of the hot corona. This is in close agreement with the average value found for Seyfert galaxies after deconvolution of the reflection hump (NP94). For $kT_{BB} = 5$ eV the spectrum of the IC component computed with the same approximation is only slightly steeper, $\alpha_x = 1.0 \pm 0.05$. For $\tau \sim 1$ the Comptonization parameter is sensibly lower and the spectrum is steeper, $\alpha_x \gtrsim 1.2$. Present observations argue against optically thick coronae [see, e.g., Zdziarski et al. 1994; NGC4151 ($\tau \simeq 3$) is probably peculiar, and can not be interpreted in the simple model presented here (see next §[4.4]).]

A more detailed computation of the expected spectra for different viewing angles, as appropriate for objects observed individually, and including the contribution of reflected

photons, yields a larger spread in the spectral shapes. In the X-ray band, the spectra are flatter for smaller angles and higher soft photon energy. This has been done in details in HM93. However the spectra shown in HM93 are computed using a rough approximation for the high energy cut–off. Detailed calculation using the formalism depicted in Chapter 2 are in progress at the time of writing this thesis (Done et al., in preparation).

We note that a reflection component is always present, but in different proportion with respect to the Comptonized component in the relevant energy range. These effects give rise to a diversity of predicted spectra which can account for the observed spectral index distributions of both, Seyfert galaxies and radio-quiet quasars, if the two classes have different kT_{BB}. In addition the thermal photon peak can be identified with the so called "soft excess" observed in several objects.

4.3 An example: Cygnus X–1

Recently Zdziarski et al. (1994) found that the high energy spectrum of IC 4329A can be well fit by the corona/disk model discussed here. The fitting parameters are $\Theta \simeq 0.5$ and $\tau \simeq 0.1$. In terms of the quasi–thermal model discussed in the previous Chapter, the fitting parameters are $\ell_h \simeq 70$ and $\ell_h/\ell_s \simeq 3.5$ which yields to a maximum electron Lorentz factor $\gamma_0 \simeq 3.5$. These results are one of the main support to the overall picture presented in this thesis.

Earlier, C.Done, G.Matt, A.Fabian and I analysed data of the GBH Cygnus X–1 (Haardt et al. 1993) in order to test the two phase model for a source with a good signal–to–noise ratio. In this section I summarize our main results.

4.3.1 Cygnus X–1 in brief

Cyg X–1 is the brightest of the Galactic non–transient black hole candidates, and its

X–ray spectrum has been well studied (see e.g. the review by Liang & Nolan 1984). It shows a hard power law in the 2–10 keV band, and excess emission at lower energies which is thought to arise from thermal emission from the accretion flow. The high energy cutoff in the spectrum at $\sim$ 100 keV suggests a thermal energy distribution of the X–ray emitting particles, leading to the widespread use of optically thick thermal Comptonization models to describe the X–ray spectrum in this and other black hole candidates.

4.3.2 Reflection features in GBHs

If X–rays illuminate an optically thick accretion flow, as expected if it forms an accretion disk, a Compton reflection spectrum is formed, whose signatures are a broad hump, peaking between 10–100 keV, a strong Fe K edge, and an associated Fe Kα emission line (Guilbert & Rees 1988; Lightman & White 1988). These spectral features also provide a diagnostic of the ionization state of the material, as the photoelectric opacity decreases with ionization, enhancing the low energy reflected flux (Lightman & White 1988), increasing the energy of the iron edge and line (e.g. Makishima 1986) and changing the line equivalent width (Ross & Fabian 1993; Matt et al. 1994).

The characteristic spectral features of reflection have been clearly seen in both AGNs, (e.g., Pounds et al. 1990; Matsuoka et al. 1990) and GBHs (Tanaka 1991; Ebisawa 1991; Done et al. 1992). While this reinforces the analogy between these two classes of objects (White et al. 1984), it also reveals some subtle differences. In AGNs the Fe Kα emission line (generally with an equivalent width, EW, of 100-200 eV: e.g. Nandra 1991) and reflected continuum are in general consistent with that predicted from a flat, solar abundance, cold X–ray illuminated disk (George & Fabian 1991; MPP). However, in Cyg X–1 the iron edge energy implies that the material is significantly ionized, while the (poorly determined) equivalent width of the line is about 50 eV, like in other Galactic black hole systems (Ebisawa 1991; Done et al. 1992;

Mitsuda 1992).

In summary, the detection of reflection signatures implies that there is an accretion disk in the system, while the higher energy data suggest IC scattering from a thermal electron distribution as the radiation mechanism for the underlying continuum. The low EW_α In such a physical picture the blackbody photons from the disk, the line and reflection continuum must all pass through the corona. This alters the theoretical predictions for both the shape and normalization of the reprocessed components in a manner which depends in particular on the Thomson depth of the corona, τ_T. In order that any reflected features are detectable at all implies that τ_T <1. This is significantly smaller that that predicted by fitting simple "Comptonization–only" models to the spectrum of Cyg X-1, where τ_T ~3 is typically found (e.g. Sunyaev & Titarchuk 1980). A corona with that Thomson depth would smear out any reflected features into invisibility.

We modelled the emergent spectra from an optically thin corona above an accretion disc, following the method depicted in Chapter 2 (Haardt 1993), and compared the results to archival data from Cyg X–1. We showed that our model is consistent with both 2–20 keV data, where reflection features are important, and higher energy data from OSSE and SIGMA. The aim of this was twofold: firstly to see if this well–defined physical picture is consistent with the data, and secondly to obtain observational limits on the optical depth and electron temperature. We showed that the two phase model is consistent with both 2–20 keV data, where reflection features are important, and higher energy data from OSSE and Sigma.

4.3.3 The model

The Comptonized spectrum (see Chapter 2) is a function of four main parameters: the vertical optical depth τ_T, the Maxwellian temperature of the corona T_e, the inclination angle $i = \cos^{-1}\mu$, and the black-body temperature T_{bb}. The relative normalization of

the soft and hard components is then completely determined by the optical depth and viewing angle. The Comptonized photons which are directed downward, i.e. back to the disk, are in part reflected by the cold layers and partly reprocessed.

Stringent limits on some of the system parameters can be set from the observed 2-20 keV spectra of Cyg X–1, due to the fact that the reflected component is actually observed in the spectrum (see Done et al. 1992 and references therein). This implies an *upper limit* on the optical depth (and consequently a *lower limit* on the coronal temperature, as τ and Θ are related through the slope of the power law) as a medium which is optically too thick would completely smear out the absorption edge in the reflection component. Similarly, the normalization of the reflection component sets an *upper limit* on Θ (and hence a *lower limit* on τ) as high electron temperatures enhance the anisotropy of the first order Compton scattering.

4.3.4 Result of model fits

We analysed in the context of the plane–parallel Comptonization model described above the EXOSAT GSPC spectra used by Done et al. (1992). Full details of the data are given in Done et al. (1992) and the same nomenclature is used to identify the spectra. The Comptonization model was computed over a five dimensional grid, with τ between 0.1-2 (16 values, logarithmic steps), Θ between 0.1-0.5 (11 values, logarithmic steps), $\mu = 0.866, 0.7, 0.5, 0.41$, $kT_{BB} = 0.1, 0.2, 0.3$ keV, and the disk ionization parameter ξ between 1-10^3 (7 values, logarithmic steps). As shown in table 1, the model gives an excellent description of the data over the 2–20 keV energy range. The iron line is neglected in these fits, as it is generally not significant in the individual datasets. This made the computation of the best fit spectrum more tractable. It has no significant effect on the derived parameters of the Compton corona, though it does affect the derived ionization parameter of the disk.

As expected both the temperature and the optical depth of the hot corona are well

Table 1

Fits to the Model

File	μ	kT_{BB} (eV)	kT_e (keV)	τ	χ^2/d.o.f.
08	$0.55^{+0.08}_{-0.06}$	218^{+13}_{-9}	$143.1^{+13.3}_{-8.2}$	$0.28^{+0.04}_{-0.04}$	144.8/137
09	$0.55^{+0.19}_{-0.04}$	220^{+12}_{-8}	$195.7^{+23.0}_{-38.8}$	$0.27^{+0.10}_{-0.05}$	125.5/106
10	$0.70^{+0.07}_{-0.17}$	211^{+30}_{-6}	$135.4^{+8.7}_{-9.7}$	$0.45^{+0.09}_{-0.07}$	98.3/118
13	$0.64^{+0.08}_{-0.13}$	207^{+16}_{-6}	$140.5^{+18.4}_{-13.3}$	$0.27^{+0.06}_{-0.04}$	211.8/205
14	$0.54^{+0.07}_{-0.06}$	210^{+8}_{-6}	$161.0^{+13.3}_{-13.3}$	$0.26^{+0.05}_{-0.06}$	108.9/127

the quoted errors are 90% confidence limits for a single parameter.

constrained, due to the presence of reflection. In Fig. 5 I show the *closed* confidence contours in τ and Θ. The correlation between τ and Θ is similar to that found in Comptonization models without reflection (Sunyaev & Titarchuk 1980) but the contours are closed as the data can distinguish between a flat spectrum with little reflection and a steep spectrum with a large amount of reflection. On the contrary, Θ and μ are largely uncorrelated (Fig. 6), showing that Θ is not dependent on the (poorly known) value of the inclination.

The mean coronal temperature is $kT_e \sim 150$ keV, determined to an accuracy of better than $\sim 15\%$ from individual spectra. This does vary, as expected from the different spectral indices measured for these data (Done et al. 1992). The limits on the optical depth are less stringent, with a dispersion about 10-20% in a single observation, but the mean of $\tau \sim 0.3$ is not consistent with all the observations. The two spectra where this variability is most apparent are Cyg09 and Cyg10. These have the flattest spectra of the sample (Done et al. 1992), and so require a larger Compton y parameter than the rest. For Cyg09 the data show substantial reflection so the increase in y is required to be mainly in kT_e, which increases to ~ 200 keV. However, for Cyg10 there

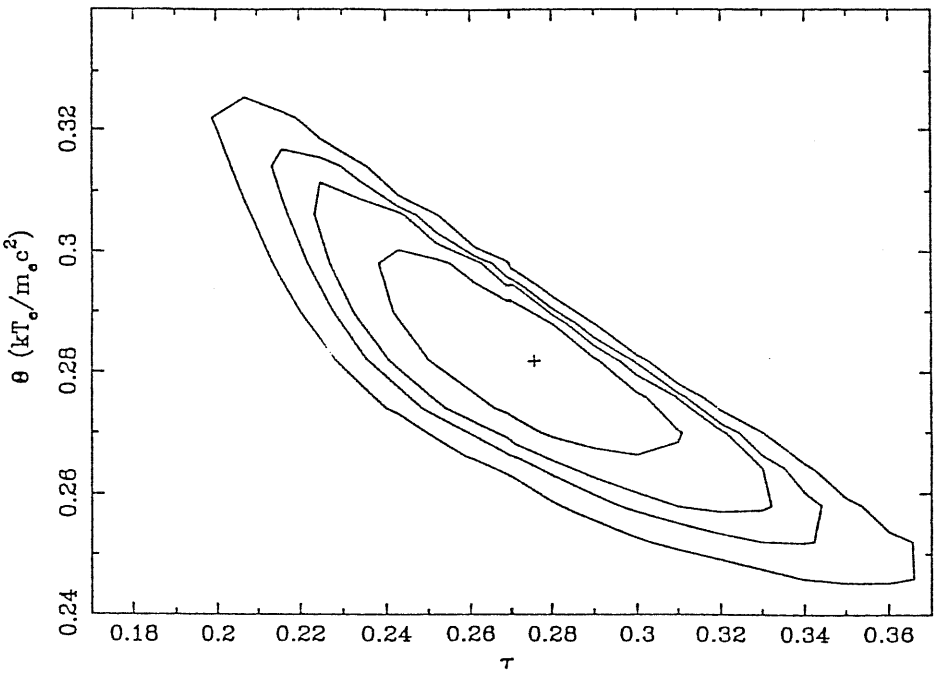

Fig. 5: Confidence contours (68%, 90%, 95% and 99% for two parameters) of the optical depth τ and the dimensionless electron temperature Θ for dataset Cyg08 (from Haardt et al. 1993).

is only a small amount of reflection present, so the data prefer an increase in y via an increase in τ to ~ 0.5.

The derived inclination angle of the system is consistent with a constant value, as required. The mean is for an inclination of 53 degrees, with a total range between 40–60 degrees. This is rather higher than that derived from photometry (Gies & Bolton 1986) and tends more towards the values obtained from polarimetry (Dolan & Tapia 1989). However the absolute inclination of the system may be quite different as relativistic corrections can change the amount of observed unscattered flux. Similarly, the blackbody temperature of ~ 200 eV, while it is consistent with a single value, does not necessarily describe the absolute temperature of the thermalized photons.

With our best fit parameters ($\tau = 0.3$, $\mu = 0.55$), and taking into account the spectral shape and the anisotropy of the continuum, we obtain EW$\sim$80 eV if cold matter is assumed, slightly greater than the observed one (Done et al. 1992). The ionization state of the disk derived by the fit is not sufficient to substantially change this value (Matt et al. 1993). However, ξ is not well determined from the fits, depending on details of the line modelling. It is therefore possible, as suggested by Ross & Fabian (1993), that the disk matter is highly ionized, and that the line intensity is further reduced by resonant trapping. This important point can only be clarified by measurements at higher energy–resolution, such as can be performed by ASCA.

Our results can be interpreted in the framework of the two phase model discussed in this Chapter. The model can be applied to black hole candidates changing only the temperature of the underlying accretion disk. All the $\Theta - \tau$ contour levels derived from the data agree within 3σ confidence with the theoretical relation linking the optical depth and the temperature of the hot corona, assuming a black body emission at 200 eV. This is an important check on the model, and supports this description of the system.

4.3.5 The γ–ray spectrum

Our spectral analysis carried out in the 2–20 keV band led to higher temperatures and lower optical depths than every other previously published fit. However we demonstrated that this apparent contradiction is a consequence of the common adoption of an optically thick corona without the reflected component.

The hard X/soft γ–ray spectrum of Cyg X–1 has been observed by many instruments, and the typical low state has been interpreted in terms of unsaturated Comptonization (Sunyaev & Titarchuk 1980) with temperatures between 30 and 80 keV, and optical depth $\sim 2 - 5$ (e.g. Sunyaev & Trumper 1979, Nolan et al. 1981, Perotti et al. 1986, Ubertini et al. 1991, Frontera & Dal Fiume 1992). This model assumes that the

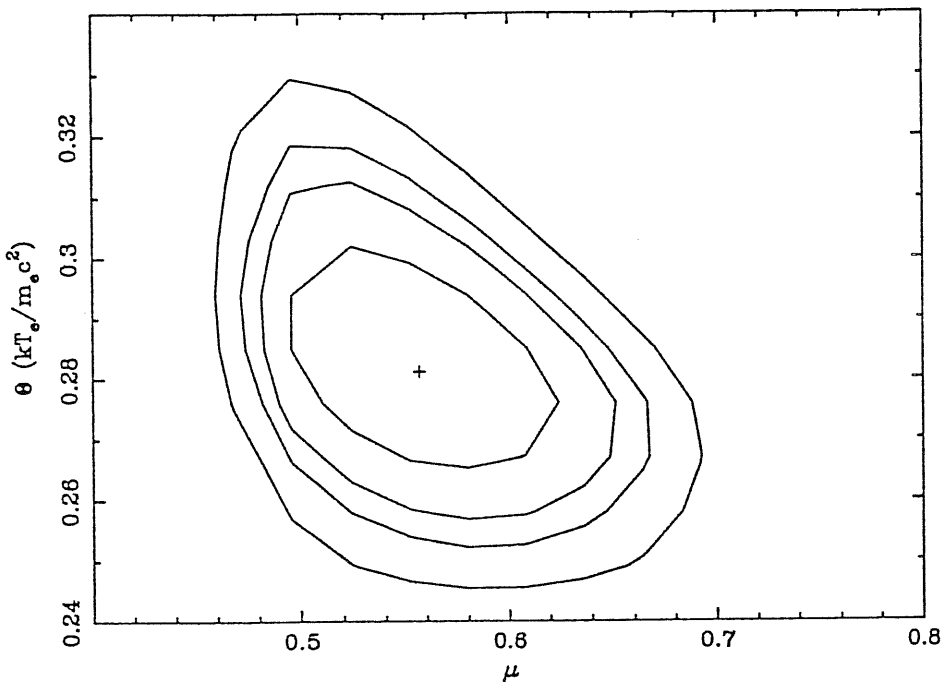

Fig. 6: Confidence contours (68%, 90%, 95% and 99% for two parameters) of the cosine of the inclination angle μ and the dimensionless electron temperature Θ for dataset Cyg08.

Comptonizing source is Thomson thick with $\tau \gtrsim 3$ so that Kompaneets equation can be solved in the diffusion approximation.

More recent, high quality data on Cyg X–1 from the SIGMA telescope onboard the GRANAT satellite (Salotti et al. 1992), and from the OSSE experiment on GRO (Grabelsky et al. 1993), again show a thermal cut-off near 200 keV. In the SIGMA observation the spectrum has been fitted with a Sunyaev & Titarchuk model, though the fit is extremely poor (reduced $\chi^2_\nu = 1.52$ for 44 d.o.f., i.e. with a less than 2% chance that the data are described by the model), with $kT_e = 62.3 \pm 4.5$ keV and $\tau = 2.02 \pm 0.13$. In the OSSE analysis the same model again does not provide an acceptable fit for two out of three observations.

In order to compute the predicted high energy spectrum, using the results described in the previous section, we performed a Monte Carlo simulation of the high energy spectrum. The proper Compton reflection component was added to the analytical spectrum at a level given by the mean reflection normalization determined by Done et al. (1992). A diagonal response matrix was constructed, simulating the typical energy resolution of present γ–ray detectors. The analytic spectrum was then convolved through this, with error bars given by the Poisson noise in each energy bin. This was made to correspond more closely with real high energy data by subtracting a null background with variance such that the spectrum contained no significant flux detections after 600 keV. This model spectrum was then fit by a Sunyaev & Titarchuk model. Quite remarkably, a single temperature model gave $kT_e = 63.6 \pm^{5}_{4.7}$ keV and $\tau = 2.04 \pm 0.13$, with a reduced $\chi^2_\nu = 1.65$ for 51 d.o.f., almost identical to the spectrum detected by SIGMA, and very similar to those detected by OSSE.

In Fig. 7 the direct and reflected contributions in our spectrum (but statistical fluctuations are not added, for clarity) are separately shown (dashed curves). It is worth noting that a two–temperature Comptonization model improves the quality of the fits for the OSSE data (Grabelsky et al. 1993). Fitting our simulated spectrum with a two temperature model gave an excellent fit ($\chi^2_\nu = 0.744$ for 48 d.o.f.), because the reflection hump mimics a lower temperature component. The reason for this difference in derived properties is that there is a physical difference between optically thick non relativistic spectra and optically thin relativistic spectra in the position and shape of the high energy turnover. A detailed discussion of this point can be found in Titarchuk (1994) and in Titarchuk & Mastichiadis (1994), where the authors show that the simple Sunyaev & Titarchuk model is inadequate in fitting data for $\tau < 3$ and/or $\Theta > 0.1$.

4.3.6 Conclusion

In Fig. 8 the Comptonized spectrum of Cyg X–1 according to our results is shown.

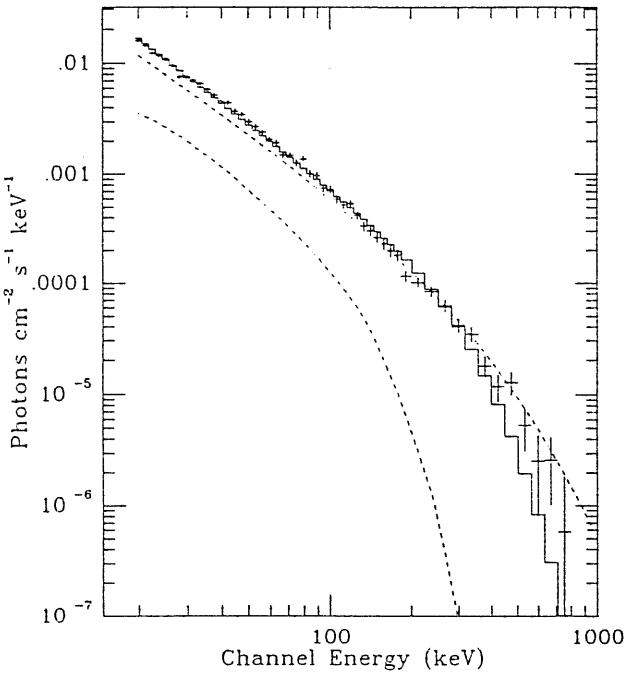

Fig. 7: The best fit single temperature Sunyaev-Titarchuk model ($kT_e = 63$ keV, $\tau = 2.0$) to the simulated Montecarlo spectrum from a plasma with $kT_e = 153$ keV and $\tau = 0.3$ and its reflection spectrum. The dashed curves represent the direct and reflected components in our spectra (but without fluctuations for clarity) (from Haardt et al. 1993).

The total spectrum (boldface line) is shown together the three contributions: the direct Comptonized emission, the (ionized) reflection component and the iron line emission.

We concluded that the X–ray emission from Cyg X–1 is likely to arise from an active thermal corona, extended above an accretion disk. The strong hard X–ray flux illuminates the disk, giving rise to a reflection spectrum, which is itself scattered in crossing the corona if a plane-parallel geometry, suggested by the low equivalent width of the iron line, applies. Since the details of the shape of the overall spectrum depend on the physical parameters of the corona, observations in the 2–20 keV range can be used to determine its optical depth and electron temperature.

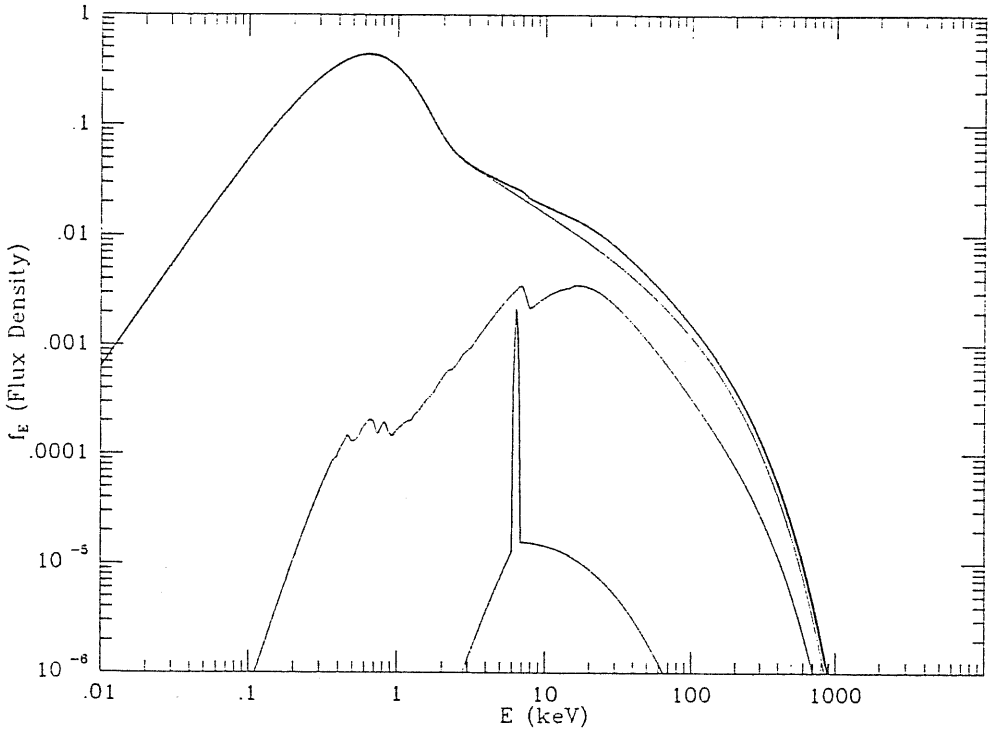

Fig. 8: The Comptonized spectrum of Cyg X–1 according to our results. The total spectrum (boldface line) is shown together the three contributions: the direct Comptonized emission, the (ionized) reflection component and the iron line emission.

4.4 X–rays from flaring coronae

We have seen that the main features of the high energy from AGNs and GBHs can be naturally explained in a thermal model assuming that the X–ray are produced in an active corona located above an accretion flow. In our model, the observed X–ray average spectrum can be reproduced if the Comptonized–to–soft luminosity ratio L_H/L_S is $\simeq 2$. In fact this leads to a Compton y parameter close to 1, and to a spectral index of the Comptonized spectrum $\alpha_x \simeq 1$. The condition $L_H/L_S \simeq 2$ means that the cooling of the corona is dominated by the reprocessed X–rays. This in turn was achieved by assuming that the *whole* gravitational power is released in the hot corona. This is a

strong constraint.

This is the theoretical motivation for the last part of this Chapter, where a new model is introduced. Beside there exist observational motivations. I would like to focus the reader attention on possible observational problems of the two phase model in the present version.

1) An implication of the OSSE observations is that the luminosity L_X, in the medium and hard X–ray range can be reliably estimated. If the "X–ray bolometric correction" established for the few galaxies detected by OSSE is adopted as a general property, the X–ray to UV flux ratios measured with ROSAT for a large sample of objects (Walter & Fink 1993) leads to an estimate of the X–ray luminosity in many cases definitely smaller than that in the UV bump, L_{UV}. Now in the two phase model the condition $L_H/L_S \simeq 2$ assumes that the soft emission L_S derives only from absorption and reprocessing of the high energy flux impinging on the disk. The model then predicts nearly equal UV and X–ray luminosities. As illustrated in HM93 the different angular distributions of the Comptonized photons with respect to the thermal ones can give rise to a UV flux larger than the X-ray one for viewing angles close to face on, but it seems difficult to achieve soft–to–hard ratios greater than 5.

2) Another prediction of the model is a tight correlation between the hard Comptonized photons (X–rays) and the soft photons from the thick layer (UV or soft X–rays for GBHs). For NGC 4151 and NGC 5548, the UV and X–ray fluxes simultaneously observed in different periods are indeed correlated, but variations (up to 30 %, Nandra et al. 1990) in X–rays on timescales of hours are not accompanied by similar variations in the UV. Furthermore, for large UV fluxes, the correlation between X–rays and UV breaks down (Perola et al. 1986, Clavel et al. 1992).

The two phase model is the simplest picture one can imagine. But if we think that the key ingredient of the model in order to work is the fact that the cooling is dominated by the preprocessed X–rays, we see that the same condition can be satisfied in a different

picture without imposing the condition $f = 1$. We have consider a modified picture, in which the active phase consists in a set of small scale hot spots or blobs, located over the disk surface, rather an extended corona. The first and obvious results is that the soft-to-hard luminosity ratio can be much higher than in the previous picture, as a large fraction of the disk emission does not need to cross the scattering region. But the most important result of the changed geometry is that we can have $L_H/L_S \sim 2$, and so we can have the right spectrum, without requiring the whole gravitational power to be dissipated in the hot phase. This is discussed in the following.

4.4.1 Structured corona: phenomenology

We maintain the assumption that the disk magnetic field can drain a fraction of the accretion power outside the accreting flow, but suppose that this power is dissipated in active localized blobs, which cover a small fraction of the total disk area. We assume that the accretion disk dissipates internally a fraction $(1 - f)$ of the accretion power Q [erg cm^{-2} s^{-1}], while the remaining fraction f is stored in magnetic field structures, which will lead to active blobs of individual size R_b. In principle f can be different in different locations of the disk, but for simplicity we will assume the same value throughout the disk. For the moment, assume also that the energy is stored in the magnetic field in a 'charge time' t_c and is released on a much shorter 'discharge time' t_d. The ratio t_d/t_c clearly coincides with the fraction of the disk area which is covered by active blobs at any time. The luminosity of a single blob will be

$$L_{blob} = [f\,Q\,\frac{t_c}{t_d}]\,\pi\,R_b^2 \tag{4.15}$$

Assuming that roughly half of the blob luminosity is intercepted and reprocessed locally by the underlying disk, the total luminosity crossing the blob is

$$L_{cool} = [Q_{disk} + Q_{rep}]\,\pi\,R_b^2 = \left[(1-f)Q + 0.5\,f\,C\,Q\,\frac{t_c}{t_d}\right]\,\pi\,R_b^2 \tag{4.16}$$

The parameter C indicates the fraction of reprocessed radiation which crosses the blob. Writing the Compton amplification factor as

$$(A-1) = L_{blob}/L_{cool} \tag{4.17}$$

we have that A is a function of three parameters, namely f, C and t_c/t_d. However in the limit $f \gg t_d/t_c$ we have

$$(A-1) \simeq 2/C \tag{4.18}$$

so that only C plays a role in determining the emitted spectrum. This condition corresponds to the disk emission per unit area below the blobs being dominated by the reprocessed radiation originally emitted by the blobs themselves. If t_d/t_c is small, we can obtain the 'right' α_x almost independently of the value of f: large UV luminosities are therefore possible even if the reprocessed radiation dominates the cooling of the blob. As the ratio of the disk to the *observed* blob emission is $2(1-f)/f$, in principle f can be derived from observations.

4.4.2 Estimate of the form factor

In the plane parallel limit $C = 1$ as the whole reprocessed flux is effective in cooling the corona. In order to estimate the value of C for different geometries, I assume that the blob is optically thin, i.e., the blob is formed by many isolated point–like sources illuminating the underlying accretion disk. I calculate the fraction of the luminosity emitted by the blob which is intercepted by the disk at any distance from the blob. Assuming that only the flux actually intercepted below the blob is effective in cooling the blob, I can estimate the value of C. Obviously a more detailed calculation should take into account the fact that any point of the underlying disk subtends the blob under a non-null solid angle. I make the assumption that the points of the disk which are not geometrically *under* the blob subtend the blob under a null solid angle, while the points

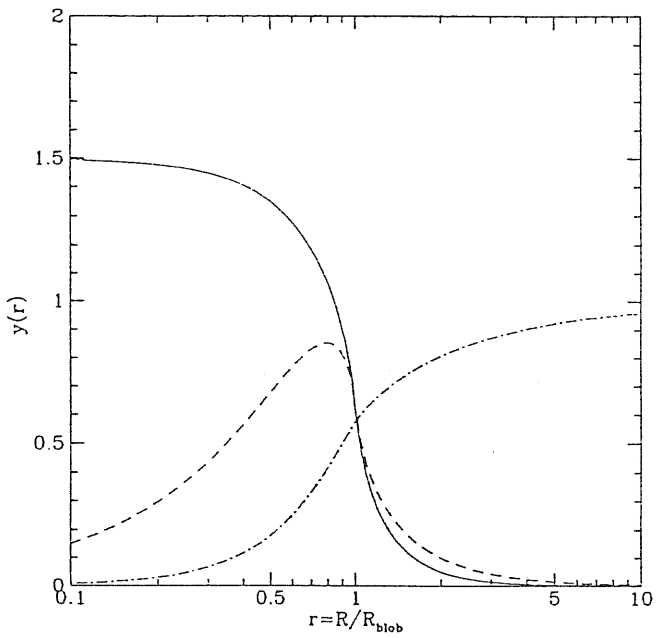

Fig. 9: The functions $s(r)$ (solid line), $rs(r)$ (dashed line) and $S(r)$ (long-short dashed line) are plotted versus $r = R/R_B$ for a semispherical blob.

which are geometrically under the blob subtend the blob under a $\Omega/2\pi = 1$ solid angle. This gives a rough estimate of C, but sufficient for our scope.

It is not difficult to demonstrate that for a semispherical blob the flux per unit area intercepted by the disk for $r \leq 1$ is

$$s(r) = 3\left[\sqrt{1-r^2} + \frac{1-r^3-(1+2r^2)\sqrt{1-r^2}}{3r^2}\right] + \frac{3}{\pi}\int_0^1 dh\, h \int_{|r-\sqrt{1-h^2}|}^{r+\sqrt{1-h^2}} dr' \frac{r'}{(r'^2+h^2)^{3/2}} \arccos[g(r',h)] \tag{4.19}$$

and that for $r \geq 1$ is

$$s(r) = \frac{3}{\pi}\int_0^1 dh\, h \int_{r-\sqrt{1-h^2}}^{r+\sqrt{1-h^2}} dr' \frac{r}{(r'^2+h^2)^{3/2}} \arccos[g(r',h)] \tag{4.20}$$

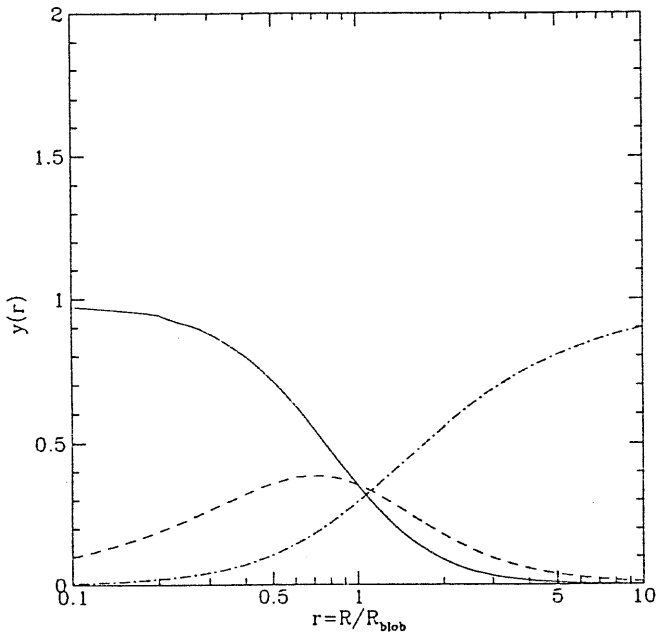

Fig. 10: Same as Fig. 9, but for a spherical blob.

The coordinates are measured in units of the blob radius.

The geometric function $g(r', h)$ is given by

$$g(r', h) = \frac{r^2 + r'^2 + h^2 - 1}{2rr'} \tag{4.21}$$

The function $s(r)$ is normalized so as

$$\int_0^\infty dr\, r s(r) = 1 \tag{4.22}$$

The limit for $r = 0$ is

$$s(0) = \frac{3}{2} \tag{4.23}$$

Another interesting case is a spherical blob located above the disk. For $r \leq 1$ we

have

$$s(r) = \frac{3}{2}\left[2\sqrt{1-r^2} - \int_{1-\sqrt{1-r^2}}^{1+\sqrt{1-r^2}} dh \frac{h}{\sqrt{r^2 - 2r\sqrt{2h-h^2}+2h}}\right] + \frac{3}{2\pi}\int_0^2 dh\, h \int_{|r-\sqrt{2h-h^2}|}^{r+\sqrt{2h-h^2}} dr' \frac{r'}{(r'^2+h^2)^{3/2}} \arccos[g(r',h)] \tag{4.24}$$

and

$$s(r) = \frac{3}{2\pi}\int_0^2 dh\, h \int_{r-\sqrt{2h-h^2}}^{r+\sqrt{2h-h^2}} dr' \frac{r'}{(r'^2+h^2)^{3/2}} \arccos[g(r',h)] \tag{4.25}$$

for $r \geq 1$.

The geometric function $g(r',h)$ for this case is given by

$$g(r',h) = \frac{r^2 + r'^2 + h^2 - 2h}{2rr'} \tag{4.26}$$

The function $s(r)$ is normalized as eq[4.22] and the limit for $r = 0$ is

$$s(0) = 1 \tag{4.27}$$

It is interesting to note that assuming that all the radiating flux comes from the center of the sphere one derives

$$s(r) = \frac{1}{(1+r^2)^{3/2}} \tag{4.28}$$

that turns out to be an exact solution of eq[4.24]–[4.25].

In Fig. 9 and Fig. 10 the functions $s(r)$, $rs(r)$ and the integral

$$S(r) = \int_0^r dr'\, r' s(r') \tag{4.29}$$

are plotted for semispherical and spherical geometry, respectively. It can be seen that $C \simeq 0.5$ is a good approximation for a blob with a height–to–radius ratio of order one.

As discussed in §[4.4.1] the actual value of α_x is determined by C. In the geometrically thin case as we have $C = 1$ we obtain the same results discussed in HM93. If

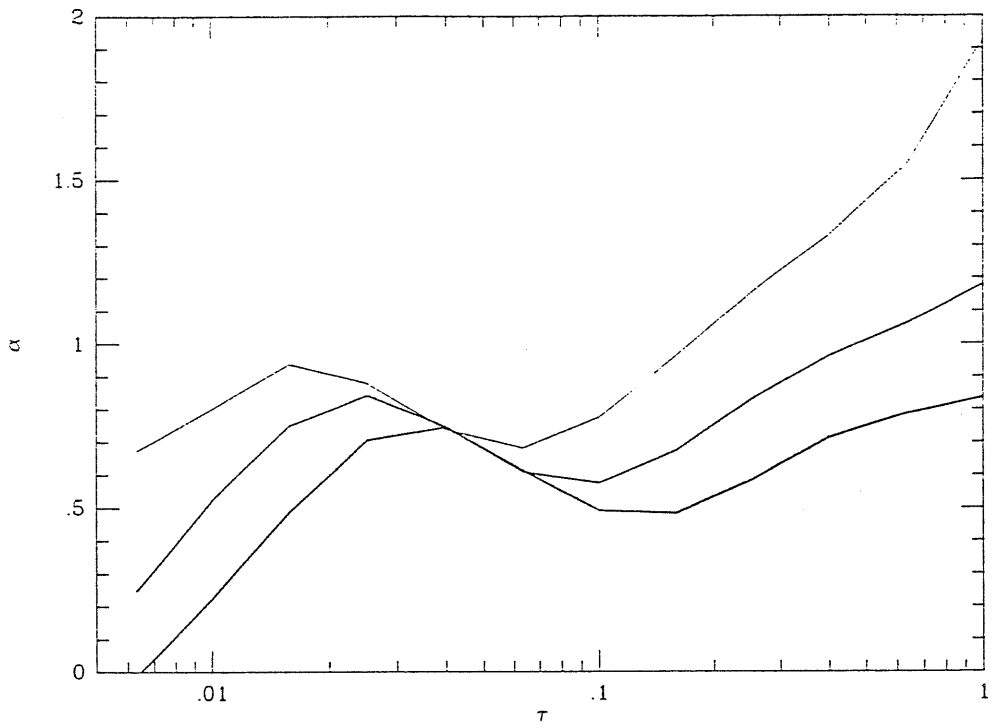

Fig. 11: Resulting spectral indices of the Comptonized component versus the blob optical depth. From bottom to the top the curves refer to solutions obtained with $C = 0.25$, 0.5, 1, fitting the spectra in the [2–20] keV range with a single power law. Reflection features are not included. A face–on line of sight is assumed.

the blobs have a height–to–radius ratio of the order of one or more, $C < 1$, the source is *photon starved*, and the corresponding power law spectral index is flatter.

To show this, I repeated the calculations of §[4.2] for $C = 0.5$ and $C = 0.25$ obtaining the Θ vs τ relation for these two cases. Then I calculated the Comptonized spectra as discussed in Chapter 2, and then I fit the [2–20]keV range of the direct spectrum (i.e., reflection features are not included) with a single power law. The results are shown in Fig. 11. For $C \gtrsim 0.25$ the spectral index α_x lies between 0.5 and 1, for $0.01 \lesssim \tau \lesssim 1$. The presence of the Compton reflection hump then further modifies the observed spectral shape.

4.4.3 Structured corona: a simple model

It was realized early on that the magnetic field can be amplified by differential rotation in accretion disks up to equipartition values and could then provide the basic viscosity and energy dissipation mechanisms. A discussion of the different ways in which this could occur is far beyond the scope of the present discussion (see for review, e.g. Hayvaerts 1990). Here I show that adopting the simple model of Galeev et al. (1979, hereafter GRV) we can derive plausible values for the parameters introduced phenomenologically in the previous section, i.e., the ratio t_d/t_c, the size R_b of the blobs, and how many blobs can be active at any time.

In the dynamo model of GRV, the disk differential rotation causes the azimuthal magnetic field B_ϕ to grow exponentially, because of a feedback mechanism linking the radial and vertical components of the magnetic field $\mathbf{B}$ to B_ϕ. The magnetic fields is amplified until its pressure equals the surrounding gas pressure, with a subsequent buoyancy of the magnetic flux tubes (see Stella & Rosner 1984). While reconnection of the magnetic field lines *within* the disk is ineffective in preventing the growth of the magnetic field, it probably occurs very rapidly in the much more tenuous coronal medium, transforming the stored energy in kinetic energy of fast particles.

Within the disk, in MHD approximation, the azimuthal magnetic field grows as

$$\frac{\partial B_\phi}{\partial t} = \frac{3v}{R} B_\phi \tag{4.30}$$

where the convection velocity v is $\approx \alpha^{1/3}\Omega z_0$. Here α is the parameter linking the stress tensor to the total disk pressure, $\Omega = \sqrt{GM/R^3}$ is the Keplerian angular frequency, and z_0 is the disk height scale. We then identify the charge time scale t_c with $R/3v$.

From the standard theory of accretion disk (Shakura & Sunyaev 1973), in the radiation pressure dominated region

$$z_0 \approx 9 R_s \mathcal{L} S(r) \tag{4.31}$$

where $\mathcal{L}$ is the total luminosity of the source in Eddington luminosity units, and

$$S(r) = 1 - \sqrt{3/r}$$

Again, R_s is the Schwarzschild radius $R_s \equiv 2GM/c^2$, and here I use $r \equiv R/R_s$. According to GRV, the scale size of the loops is

$$R_b \approx z_0/\alpha^{1/3} \tag{4.32}$$

Note that, since $z_0 \propto \mathcal{L}$, the compactness ℓ_h of a single loop ($\propto L/R_b$) is independent of the source luminosity.

With the above assumptions the charge time scale becomes

$$t_c \sim \frac{R}{3\alpha^{1/3}\Omega z_0} \sim 0.5\frac{r^{5/2}\,M_6}{\alpha^{1/3}\mathcal{L}\,S(r)} \quad \text{s} \tag{4.33}$$

where $M_6 \equiv M/10^6 M_\odot$. Note that in sources closer to the Eddington limit the magnetic field grows rapidly because of the high convection velocity ($v \propto z_0 \propto \mathcal{L}$).

The discharge time scale t_d depends on the microphysical processes operating in the dissipation of magnetic energy. We parameterize it as

$$t_d = a\left(\frac{R_b}{c}\right) \tag{4.34}$$

t_d is the maximum between the time needed to transfer the magnetic energy to the particles and the cooling time scale of the particles. Since the cooling time is very short (see below), the strongest constraint derives from the acceleration time scale which is highly uncertain, but should be $\sim R_b/v_{rec}$, where v_{rec} is the reconnection velocity. Theoretical estimates of v_{rec} range from $v_{rec} \sim v_A/\ln R_m$, where v_A is the Alfvèn velocity and R_m the magnetic Reynolds number for Petschek's type reconnection (Petschek 1964), to $v_{rec} \sim v_A$ (Priest & Forbes 1986).

A rough estimate of a can be derived from the ~ 10 sec duration of the impulsive phase of Solar flares during which particles are believed to be accelerated. Typical

solar values of R_b and v_A are $\sim 10^9$ cm and $\sim 6 \times 10^8$ cm/s respectively, so that the acceleration time is ~ 6 times the Alfvèn wave crossing time. Assuming that in the AGN rarefied coronal medium $v_A \sim c$, we obtain $a \sim 6$. The ratio t_c/t_d can then be written from eq[4.33] and eq[4.34] as

$$\frac{t_c}{t_d} \sim 3 \left(\frac{r}{5}\right)^{5/2} \left(\frac{10}{a}\right) \left(\frac{0.1}{\mathcal{L}}\right)^2 \left[\frac{1}{S(r)}\right]^2 \tag{4.35}$$

independent of viscosity and mass. At $r = 5$ we obtain $t_c/t_d \gtrsim 60$ (for $\mathcal{L} \lesssim 0.1$) which ensures that $Q_{rep} \gg Q_{disk}$ throughout the disk. The ratio t_c/t_d becomes of order unity in the innermost part of the disk ($5 \lesssim r \lesssim 12$) only for sources radiating close to the Eddington limit.

Since the cooling time of the accelerated particles is shorter than the time scale of the energy release in the loops (see below) we can think of the spectral evolution as a succession of stationary states. Particles may reach equilibrium as suggested in the previous Chapter (see also Ghisellini et al. 1993), by means of continuous re–acceleration of electron–positron pairs and Compton losses on the reprocessed photons. The resulting energy distribution would be quasi–thermal, with typical temperature of $300 \gtrsim kT \gtrsim 50$ keV for $10 \lesssim \ell_h \lesssim 100$. The energy input in the hot particles may fluctuate strongly on the time scale associated with the evolution of magnetic structures in the loop phase (minutes-hours for Seyferts), while keeping a constant average on medium time scales (days), determined by the constancy in the energy transport of the accretion flow.

Using the time scale estimates given above, the loop variability time scale should be of the order of minutes for a 10^6 solar mass object, and of milliseconds for a 10 solar mass object (for a detailed discussion of variability in corona models see, e.g., Pudritz 1981a,b; Pudritz & Fahlman 1982; and Abramowicz et al. 1991)

4.4.4 Number and luminosity of active loops

We assume that the dynamo process operates all over the disk. In a disk sector between

$R - R_b$ and $R + R_b$ the number of magnetic loops that are growing *within* the disk is

$$N_{grow} = \frac{4\pi R R_b}{\pi R_b^2} = 4R/R_b \tag{4.36}$$

and the number of active loops *above* the disk is

$$N_{act} = \frac{t_d}{t_c} N_{grow} \sim 12 a \alpha^{1/3} \frac{\Omega z_0}{c} \tag{4.37}$$

Transforming these two quantities into differentials we obtain the differential number of active loops:

$$\frac{dN_{act}}{dR} = \frac{2\pi R}{4\pi R R_b} N_{act}(R) \sim 6 a \alpha^{2/3} \Omega / c \tag{4.38}$$

Integrating from $3R_s$ to infinity, we then derive the total number of active loops at any time:

$$N_{tot} = \int_{3R_s}^{\infty} dR \, \frac{dN_{act}}{dR} \sim 2\sqrt{6} a \alpha^{2/3} \tag{4.39}$$

This number does not depend neither on the luminosity nor on the mass of the source.

According to Pringle (1981), observations of stellar accretion disks seem to require $\alpha \sim 0.1$. Setting $a = 10$ we find $N_{tot} \sim 10$. From simple Poissonian noise arguments, this is what is needed to explain X–ray fluctuations of a factor ~ 2 on short time scales, that are typically observed in AGNs and GBHs.

Finally the luminosity of a single blob located at r is estimated as

$$\begin{aligned} L_{blob} &= f Q(R) 2\pi R \frac{dR}{dN_{act}} \\ &\sim 1.2 \times 10^{43} M_6 \left(\frac{f}{0.2}\right) \left(\frac{10}{a}\right) \left(\frac{0.1}{\alpha}\right)^{2/3} \left(\frac{1}{r}\right)^{1/2} \mathcal{L} S(r) \quad \mathrm{erg\,s^{-1}} \end{aligned} \tag{4.40}$$

Since $S(r) = 1 - \sqrt{3/r}$, the most luminous blobs are those located at $r = 12$ (although the maximum of the coronal surface emissivity is at $r \simeq 5$) and can have 30% of the total luminosity emitted by the entire ensemble of loops.

From the above equation, the compactness parameter of the loops is

$$\ell_h \sim 50 \left(\frac{f}{0.2}\right) \left(\frac{10}{a}\right) \left(\frac{0.1}{\alpha}\right)^{1/3} \left(\frac{1}{r}\right)^{1/2} \tag{4.41}$$

In the most radiative part of the disk the blobs have $\ell_h \sim 30$. This should be considered as a *lower limit* of the actual compactness, since the acceleration region may be smaller than R_b, the value used in the derivation of eq[4.41].

The compactness ℓ_h is independent of the source luminosity and the mass of the central black hole. This may account for the remarkable similarity of the high energy spectra of AGNs and GBHs. Furthermore, the order of magnitude of the compactness parameter is consistent with observations (Done & Fabian 1990). In retrospect, since the Compton cooling time in a source of compactness ℓ_h is $\sim (R/c)/\ell_h$ our assumption that the cooling time is shorter than the acceleration time is justified.

Finally, we can estimate the magnetic field required to be consistent with observations, comparing the magnetic energy density with the gravitational available power. From

$$f \sim \frac{B^2}{8\pi} \frac{dN_{grow}}{dR} \frac{V_{loop}}{2\pi r Q(R) t_c} \tag{4.42}$$

where V_{loop} is the volume of a single loop, we estimate that, in order to have $f \simeq 0.2$ in a source radiating at 10% of the Eddington limit, the required (amplified) magnetic field is $B \sim 10^5$ G at $r = 5$.

4.4.5 Reprocessed radiation

The temperature of the thermal radiation below the loops will be generally higher than the temperature of the disk emission at the same radius producing a hotter thermal component superimposed to the multicolor disk emission. The flux per unit time per unit area of the reprocessed radiation below the loops is a factor t_c/t_d higher than that due to viscous dissipation in the disk. Using a black body approximation, the temperatures of the two components can be written as

$$kT_{disk} \sim 30\, M_6^{-1/4} (1-f)^{1/4} \left(\frac{5}{r}\right)^{3/4} \left(\frac{\mathcal{L}}{0.1}\right)^{1/4} S(r)^{1/4} \quad \text{eV} \tag{4.43}$$

and

$$kT_{rep} \sim 35\, M_6^{-1/4}\, f^{1/4} \left(\frac{10}{a}\right)^{1/4} \left(\frac{5}{r}\right)^{1/8} \left(\frac{0.1}{\mathcal{L}}\right)^{1/4} S(r)^{-1/4} \quad \text{eV} \tag{4.44}$$

In the innermost part of the accretion disk the reprocessed component can be $\approx 2-3$ times hotter than the disk temperature at the same radius. The reprocessed radiation temperature is a very weak function of the radius and is higher in low luminosity objects.

In Fig. 12 the disk temperature and the reprocessed radiation temperature are plotted against the distance from the central black hole, assuming $M_6 = 1$, $\mathcal{L} = 0.1$ and $f = 0.2$. With the adopted formulae the temperature of the reprocessed radiation diverges as r goes to 3. However the effective area of the blob goes to 0 rapidly, so that the net flux of the reprocessed radiation field correctly goes to 0 as r goes to 3.

The total thermal emission from the accreting flow is then formed by a multicolor spectrum as in the standard α–disk (Shakura & Sunyaev 1973) –with the difference that at each R the surface emissivity is a fraction $(1-f)$ of that of a standard disk– plus a hotter multicolor component with a much smoother radial dependence, i.e.,

$$F_{disk} \sim \frac{4\pi \cos i}{(hcD)^2} E^3 \int_{3r_s}^{\infty} dr \, \frac{r}{e^{E/kT_{\rm disk}(r)} - 1} \quad [\text{erg cm}^{-2}\ \text{sec}^{-1}\ \text{Hz}^{-1}] \tag{4.45}$$

and the hotter thermal component

$$F_{rep} \sim \frac{4\pi \cos i}{(hcD)^2} E^3 \int_{3r_s}^{\infty} dr \, \frac{t_d}{t_c} \frac{r}{e^{E/kT_{\rm rep}(r)} - 1} \quad [\text{erg cm}^{-2}\ \text{sec}^{-1}\ \text{Hz}^{-1}] \tag{4.46}$$

The latter can be identified with the soft excess observed in several AGNs. In eq[4.45] and eq[4.46] D is the distance of the source, and i the viewing angle of the accretion disk with respect to an observer.

4.4.6 Time averaged Comptonized spectrum

The emitted spectrum from the active loops depend on the dominant energy loss mechanism effective in cooling the hot particles. Comparing the energy losses due to cyclo-synchrotron and IC radiation, it can be shown that the cooling is dominated by the

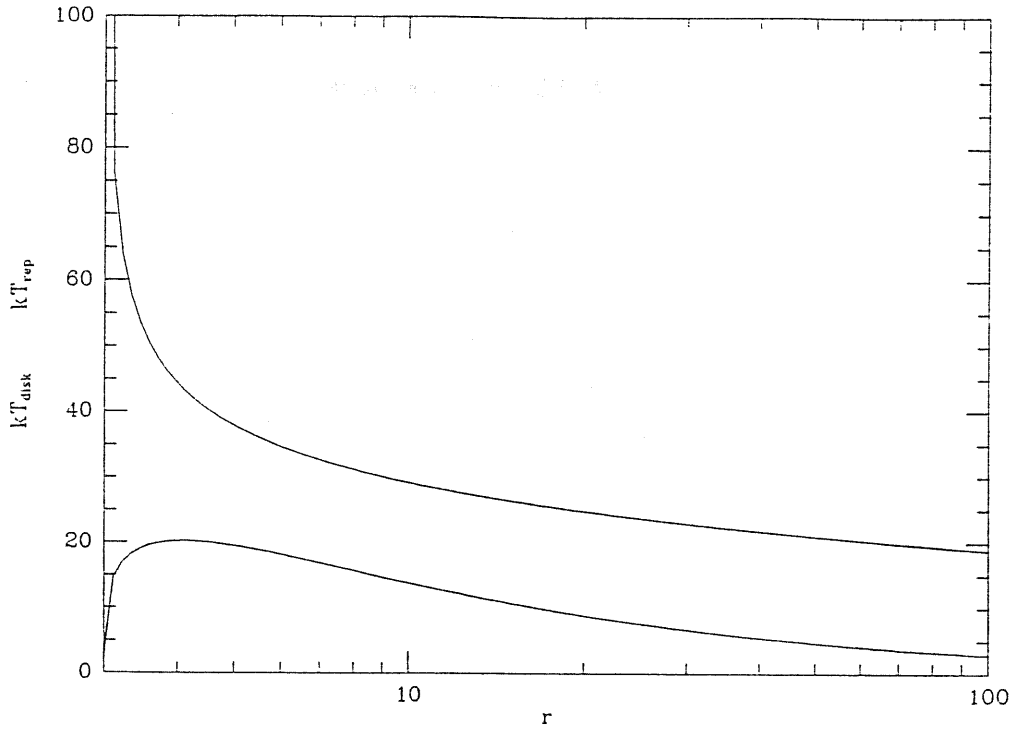

Fig. 12: The disk temperature and the reprocessed radiation temperature are plotted against r, assuming $M_6 = 1$, $\mathcal{L} = 0.1$ *and* $f = 0.2$. *Although the temperature of the reprocessed radiation diverges as r goes to 3, the effective area of the blob goes to 0 rapidly, so that the net flux of the reprocessed flux correctly goes to 0 as r goes to 3.*

latter mechanism, since the cyclo-synchrotron radiation is strongly self–absorbed. A further important source of energy losses could be the thermal conduction from the emerging loop to the lower cold gas. In the case of the accretion disk dynamo model proposed by GRV, assuming that the main source of soft photons is the accretion disk, Comptonization dominates the coronal energy balance for source luminosities greater than few percent of the Eddington limit. In our case the soft photon flux (below the loops) of reprocessed radiation is much greater than that due to the inner disk dissipation. We then conclude that for the typical conditions of AGNs and GBHs, IC radiation is likely to be the main cooling process for the blobs.

In order to estimate the average Comptonized spectrum I approximate eq[4.41] with

$$\ell_h(r) = 400\frac{f}{r^{1/2}} \tag{4.47}$$

Furthermore I approximate the $\ell_h - \Theta$ and $\ell_h - \tau$ curves of Fig. 3 and 4 as:

$$\begin{aligned} \Theta &= 1.20\ell_h^{-0.29} \quad & \tau &= 0.020\ell_h^{0.485} \\ \Theta &= 1.70\ell_h^{-0.41} \quad & \tau &= 0.016\ell_h^{0.560} \\ \Theta &= 0.78\ell_h^{-0.26} \quad & \tau &= 0.066\ell_h^{0.302} \\ \Theta &= 0.13 \quad & \tau &= 0.530 \end{aligned} \tag{4.48}$$

valid for $\ell_h < 20$, $20 < \ell_h < 200$, $200 < \ell_h < 1000$ and $\ell_h > 1000$, respectively. Combining the last two equations we find

$$\begin{aligned} \Theta &= 0.210f^{-0.29}r^{0.145} \quad & \tau &= 0.375f^{0.485}r^{-0.242} \\ \Theta &= 0.146f^{-0.41}r^{0.205} \quad & \tau &= 0.458f^{0.0.560}r^{-0.280} \\ \Theta &= 0.164f^{-0.26}r^{0.130} \quad & \tau &= 0.403f^{0.302}r^{-0.151} \end{aligned} \tag{4.49}$$

valid for $r > 400f^2$, $400f^2 > r > 4f^2$ and $4f^2 > r > 3$, respectively. Of course each of these limits, once that f is specified, has to be compared with 3. The above approximations assume $C = 1$.

Now from the number of blobs active at any radius, their luminosity, their temperature and optical depth, we can calculate the spectrum using the formalism for plane parallel geometry discussed in Chapter 2, summing the spectra produced by the different blobs. Two examples are shown in Fig. 13 and Fig. 14. The Compton reflection hump is not included. The two figures refer to a $10^6 M_\odot$ object radiating 0.1 of the Eddington luminosity. A face–on line of sight is assumed. The two cases differ in the assumed value of f: in the Fig. 13 I adopted $f = 0.99$, i.e., all the accretion luminosity is released in the active blobs, while in Fig. 14 f is 0.2, that is close to the average value of Seyfert 1 galaxies.

The total spectrum is shown together with the contributions from $3 < r < 5$, $5 < r < 10$, $10 < r < 20$ and $r > 20$. The different contributions can be identified by the

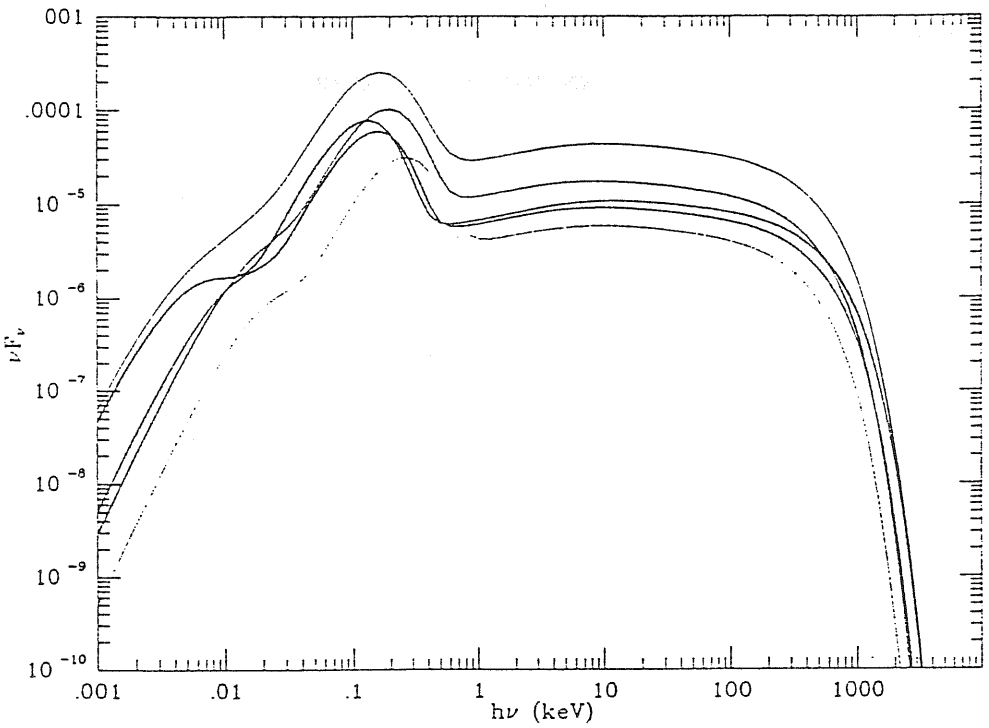

Fig. 13: The total spectrum from the "blobby disk" is shown together with the contributions from $3 < r < 5$, $5 < r < 10$, $10 < r < 20$ and $r > 20$. The different contributions can be identified by the decreasing black–body temperature as r increases. The Compton reflection hump is not included. The case is for a $10^6 M_\odot$ object radiating 0.1 of the Eddington luminosity. A value $f = 0.99$ is assumed.

decreasing black–body temperature as r increases. As can be seen, the power–law part of the spectrum is dominated by the radiation emitted between 5 and 10 Schwarzschild radii, while the cut–off is smoother than an exponential because of the superposition of many spectra of different temperatures. More detailed calculations, including the Compton reflection hump, the iron line emission, and frequency dependent variability analysis are in progress.

4.4.7 Correlated variability

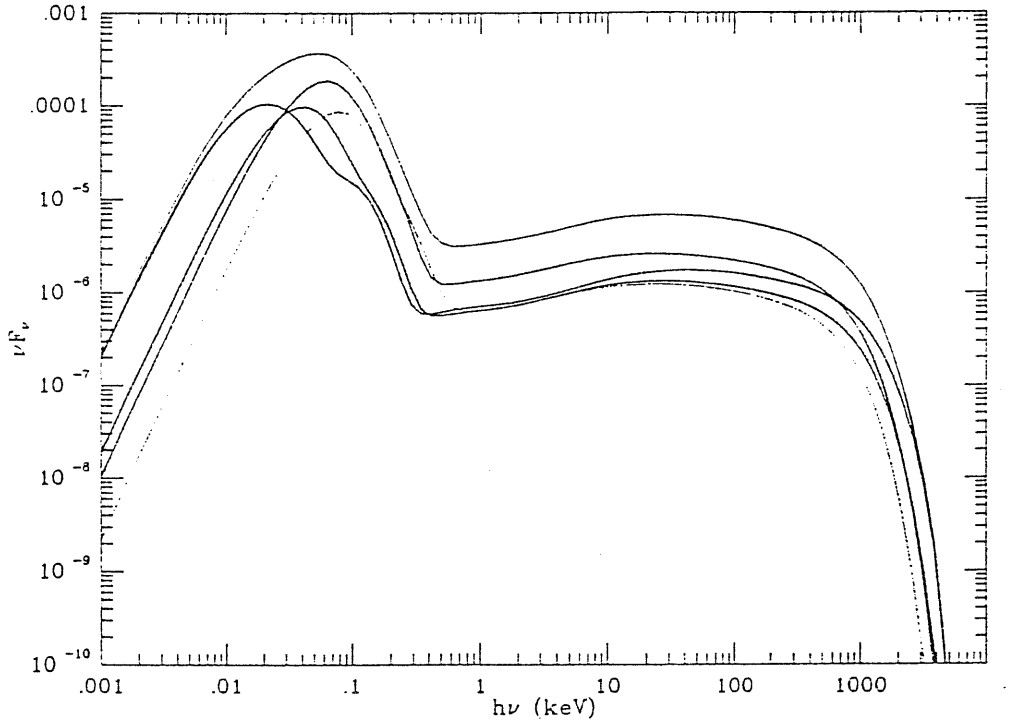

Fig. 14: Same as Fig. 13, but $f = 0.2$.

The model presented here includes three emission components: 1) the luminosity due to dissipation within the accretion disk which we generally call L_{UV} (although in GBHs it is mostly emitted in the soft X–ray band); 2) the upward Comptonized luminosity L_X extending from the medium to the hard X-ray range; 3) the reprocessed luminosity L_{rep} which comprises a thermal peak hotter than the direct disk emission and a Compton reflection hump at 10–100 keV (Lightman & White 1988).

The ratio of L_X to L_{UV} is determined by the fraction f of the total gravitational power stored in the magnetic field, while L_{rep} is *always* of the order of L_X. Observations of Seyfert galaxies suggest that the UV emission may be up to an order of magnitude larger than the X–ray emission (e.g. Walter & Fink 1993): in the present model this corresponds to $f = 0.2$. For $f = 0.2$ the high energy spectrum can have a spectral index

close to unity if $t_c/t_d \gg 5$, which is not a severe constraint.

The reprocessed component L_{rep} may be related to the variable hard UV component inferred in some Seyfert galaxies (e.g. NGC 4151) and/or to the so called "soft-excess" observed in the soft X–ray band (e.g. Yaqoob & Warwick 1991, Pounds et al. 1993, Walter et al. 1993). The soft excess luminosity relative to the the direct disk emission L_{UV} is determined by f.

The actual size scale and number of active regions and the associated variability time scales, estimated in §[4.4.3] and §[4.4.4] on the basis of the GRV model for the magnetic corona, are generally consistent with observations. In particular the number of blobs turns out to be ~ 10, independent of the luminosity of the source and of the mass of the central black hole. Short time scale variability can be associated with stochastic noise in the number of active blobs which can easily produce flux variability up to a factor 2. Since the size of the blobs scales with total luminosity L, the variability time scale turns out to be proportional to L.

L_X can fluctuate on the shortest timescales, and its fluctuation is associated with the blob size and the energy dissipation rate. L_{rep} must vary in a correlated fashion with L_X. However a smearing in time can result from the shape of the blobs which may illuminate a larger area than that intercepted by the blobs themselves ($C < 1$; §[4.4.2]). In addition there is a dilution introduced by the disk component L_{UV}.

In objects where the UV component is definitely more luminous than the X–ray component ($f \ll 1$) the dilution is expected to be important. In these cases we do not expect correlated variability on short time scales between the UV and the X–rays. However, the correlation could hold on medium time scales if the power dissipated in the disk varies and f is constant. On the other hand, we predict a substantial amount of UV flux correlated to the X–rays in sources where these two components have comparable luminosity. We note that in the two cases where the UV – X-ray correlation has been observed, NGC 5548 (Clavel et al. 1992) and NGC 4151 (Perola et al. 1986, 1994), the UV and X–ray fluxes are indeed comparable. It is therefore possible, pending an

estimate of the bolometric correction factors for the two bands (e.g. Perola and Piro 1994), that for these objects f is close to unity and therefore the reprocessed component is strong in the UV. The lack of short time variations in UV (Clavel et al. 1992) suggests that the reprocessing region is greater than the size of the blobs. This is consistent with a moderate photon starvness of the emitting blobs (i.e. $C < 1$), as required by the flatness of the [2–20] keV spectrum of these two objects [$\alpha_x \simeq 0.5$ for NGC 4151 (Yaqoob & Warwick 1991) and $\alpha_x \simeq 0.8$ for NGC 5548 (Nandra et al. 1991)].

Conclusion

"So far so good...so what?" – D.Mustaine

In this thesis we have seen that there are indications that the high energy emission from γ–ray weak AGNs may derive from inverse Compton scattering of soft photons over a thermal population of electrons and positrons. I have explained what the adjective "thermal" should mean, i.e., the average energy of the emitting particles is small as result of pair cascade. The soft photons are emitted as thermal radiation by a relatively cold accretion flow. I have given arguments supporting a picture in which magnetic reconnection could play a main role. The accretion disk corona should be considered as an ensemble of active small scale structures, each of them living for a time ~ 10 times longer than the light crossing time. This structured corona can account for the main spectral features, and for the observed light curves.

Those were the good news. What about the bad ones? As usual for theoreticians they come from observations. A good example is a recent analysis of Seyfert 2 GINGA spectra. It seems that type 2 objects have an intrinsic [2–20] keV spectrum much flatter that the canonical $\alpha_x \simeq 1$ observed in type 1 objects (Done 1994, Zdziarski 1994; private communications). This is of course against the unified scheme. Anisotropic Compton emission would give rise to the opposite result, the spectra of Seyfert 2 being steeper than those of Seyfert 1 (see Haardt 1993) [but a central X–ray region illuminated by soft UV photons from the outer part of the disk, as in the two temperature model of Shapiro et al. (1976), may work in the right way].

I did not included theoretical problems into the "bad news" record. The main theoretical problem is probably the physics of the active corona. The phenomenological toy model depicted here simply indicates a possible direction of research. The problem of a self–consistent description of a corona formed by reconnecting flux tubes is complex, and several high–tech models have been developed in the past for the Solar corona case. Nevertheless magnetic reconnection in AGNs and GBHs is still a sort of "black magic" invoked shaking the hands when all else fails. In the next future perhaps plasma physics people will be able to construct self–consistent accretion disk corona models. A first step could be the recent paper by Svensson & Zdziarski (1994). From a computational point of view, the massive use of parallel machines will be, sooner or later, inevitable.

On a more phenomenological ground, several aspects of the model discussed in Chapter 4 can be investigated in more detail. For example analysis of the variability pattern of the "blobby disk" will be the next step I aim to pursuit. The theoretical light curves and spectral correlations will be compared with observations, as it has been done by Grandi et al. (1994) for the non–thermal pair reflection model.

In conclusion, the conclusion of this thesis can not be different from the standard clichè: a lot of work has been done, much more has to be done. The very next future will be extremely exciting, expecially from the observational point of view, as the forthcoming ASCA results are going to greatly improve our knowledge, and maybe our understanding [or misunderstanding. I still remember what G.Stewart said in Varenna (october 1990) concluding his talk about the at that time recent GINGA observations of AGNs: "The more I know, the less I understand". It was the first workshop I attended. Naively "So why should I know?" was what I thought].

References

Abramowicz M.A. et al., 1990, A&A, 245, 454

Antonucci R.R., 1993, ARA&A, 31, 473

Antonucci R.R., Miller J.S., 1985, ApJ, 297, 621

Awaki H. et al., 1990, Nat, 346, 544

Awaki H. et al., 1991, PASJ, 43, 195

Balucinska M., Hasinger G., 1991, A&A, 241, 439

Band D.L. et al., 1990, ApJ, 262, 90

Barr P., Mushotzky R.F., 1986, Nat, 320, 421

Basko M.M., 1978, ApJ, 223, 268

Bisnovatyi-Kogan G.S., Zel'dovich Ya.B., Sunyaev R.A., 1971, Astr. Zh., 48, 24 (Soviet Astr.–AJ, 15, 17)

Branduardi–Rymont G., 1986, in Mason K.O., Watson M.G., White N.E. eds, The Physics of Accretion onto Compact Objects. Springer-Verlag: Berlin, p.407

Brown J.C., McLean I.S., 1977, A&A, 57, 141

Cameron R.A. et al., 1993, in Gehrels N. et al. eds, Proceedings of the Compton symposium, St. Louis, p. 478

Cavaliere A., 1982, in Plsama Astrophysics, SP–161, ESA, p.97.

Celotti A., Fabian A.C., Rees M.J., 1992, MNRAS, 255, 419

Chandrasekhar S., 1960, Radiative Transfer. Dover, New York

Clavel J. et al., 1992, ApJ, 393, 113

Comastri A. et al., 1992, ApJ, 384, 62

Coppi, P.S., Blandford, R.D. 1990, MNRAS, 245, 453

Coppi P.S., Zdziarski A. A., 1992, ApJ, 398, L37

Czerny B., Zycki P., 1994, ApJ, in press

Dolan J.F., Tapia S., 1989, ApJ, 344, 830

Done C., Fabian A. C., 1989, MNRAS, 240, 81

Done C., Ghisellini G., Fabian A.C., 1990, MNRAS 245, 1

Done C. et al., 1992, ApJ, 395, 275

Ebisawa K., 1991, PhD thesis, University of Tokyo, Japan

Fabian A.C. et al., 1989, MNRAS, 238, 729

Fabian A.C. et al., 1993, ApJ, 416, L57

Field G.B., Rogers R.D., 1992, in Holt S.S., Neff S.G., Urry C.M. eds, Proc. of Conf., Testing the AGN Paradigm. AIP: New York, p. 329

Field G.B., Rogers R.D., 1993, ApJ, 403, 94

Fiore F. et al., 1992, A&A, 262, 37

Fiore F. et al., 1993, ApJ, 415, 129

Frontera F., Dal Fiume D., 1992, in Koyama K., Kunieda H. eds, Proc. of Conf., Frontiers of X–ray Astronomy. Universal Academy Press: Tokyo, p. 311

Galeev A.A., Rosner R., Vaiana G.S., 1979, ApJ, 229, 318 (GRV)

Gautschi W., Cahill W.F., 1970, in M. Abramowitz and I. A. Stegun eds, Handbook of Mathematical Functions: nineth edition. Dover: New York, p.227

George I.M., Fabian A.C., 1991, MNRAS, 249, 352

Ghisellini G., 1987, PhD thesis, ISAS/SISSA, Italy

Ghisellini G. et al., 1991, MNRAS, 248, 14

Ghisellini G., Haardt F., Fabian A.C., 1993, MNRAS, 263, L9

Ghisellini G., Haardt F., Matt G., 1994, MNRAS, 267, 743

Ghisellini G., Haardt F., 1994, ApJ, 429, L53

Gies D.R., Bolton C.T., 1986, ApJ, 304, 371

Grabelsky D.A. et al., 1993, in the Proc. of the First Compton Observatory Symposium, St. Louis, October 1992

Grandi P. et al., 1992, ApJS, 82, 93

Grandi P., Urry C.M., Done C., 1994, ApJ, 428, 599

Grebenev S. et al., 1993, A&AS, 97, 281

Grindlay J.E., Luke M., 1990, in Gorestein P., Zombeck M. eds, IAU Colloq. 115. Kluwer: Dordrecht, p. 276

Guilbert P.W., Fabian A.C., Stepney S., 1982, MNRAS, 199, 19P

Guilbert P.W,. Rees M.J., 1988, MNRAS, 233, 475

Haardt F., Maraschi L., 1991, ApJ, 380, L51

Haardt F. et al., 1993, ApJ, 411, L95

Haardt F., Maraschi L., 1993, ApJ, 413, 507 (HM93)

Haardt F., 1993, ApJ, 413, 680

Haardt F., Matt G., 1993, MNRAS, 261, 346

Haardt F., Maraschi L., Ghisellini G., 1994, ApJ, in press

Halpern J.P., 1982, PhD thesis, Harvard Univ., USA

Halpern J.P., 1985, ApJ, 290, 130

Haniff C.A., Ward M.J., Wilson A.S., 1991, ApJ, 368, 167

Herterich K., 1974, Nat, 250, 472

Heyvaerts J., 1990, in Bertout et al. eds, Proceedings of 6th IAP Astrophysical Meeting / IAU coll. Edition Frontieres, p129

Hua X.-M., Lingenfelter R.E., 1992, ApJ, 397, 591

Iwasawa K. et al., 1993, ApJ, 409, 155

Jelley J.V., 1966, Nat, 211, 472

Johnson W.N. et al., 1993, A&AS, 97, 21

Jones F.C., 1968, Phys. Rev., 167, 1159

Jourdain E. et al., 1992, A&A, 256, L38

Kii T. et al., 1991, ApJ, 367, 455

Kii T. et al., 1992, in Koyama K., Kunieda H. eds, Proc. of Conf., Frontiers of X–ray Astronomy. Universal Academy Press: Tokyo, p.577

Kojima Y., 1991, MNRAS, 20, 629

Kouveliotu C. et al., 1992a, IAU circ No.5592

Kouveliotu C. et al., 1992b, IAU circ No.5608

Koyama K. et al. 1989, PASJ, 41, 731

Krolik J.H., Begelman M.C., 1988, ApJ, 329, 702

Krolik J.H., Kallman T.R., 1987, ApJ, 320, L5

Krolik J.H., Madau P., Zycki P., 1994, ApJ, 420, L57

Kunieda H. et al., 1990, Nat, 345, 786

Kunieda H. et al., 1992, ApJ, 384, 482

Laor A., 1991, ApJ, 376, 90

Lawrence A., Elvis M., 1982, ApJ, 256, 410

Lawson A.J. et al., 1992, MNRAS, 259, 743

Letho H.J., Czerny B., McHardy I.M., 1992, MNRAS, 261, 125

Liang E.P., Nolan P.L., 1984, Space Sci. Rev., 38, 353

Lightman, A.P. 1982, ApJ, 253, 842

Lightman A.P., White T.R., 1988, ApJ, 335, 57

Lin Y.C. et al., 1993, ApJ, 416, L53

Madau P., Ghisellini G., Fabian A.C, 1993, ApJ, 410, L10

Madau P., Ghisellini G., Fabian A.C, 1994, MNRAS, in press

Madjeski G. et al., 1994, ApJ, submitted

Makishima K., 1986, in Mason K.O. et al. eds, The Physics of Accretion onto Compact Objects. Springer-Verlag, Berlin, p. 249

Maisack M., Yaqoob T., 1991, A&A, 249, 25

Maisack M. et al., 1993, ApJ, 407, L61

Maraschi L. et al., 1991, ApJ, 368, 138

Marshall F.E., Levine A.M., Primini F.A., 1981, Nat, 293, 275

Marshall F.E. et al., 1992, ApJ, 405, 16

Matsuoka M. et al., 1990, ApJ, 361, 440

Matt G., Perola G.C., Piro L., 1991, A&A, 247, 25 (MPP)

Matt G. et al., 1992, A&A, 257, 63 (Erratum in A&A, 263, 453)

Matt G., Perola G.C., Stella L., 1993, A&A, 267, 643

Matt G., Fabian A.C., Ross R., 1993, MNRAS, 262, 179

Matt G., 1993, MNRAS, 260, 663

Matt G., Fabian A.C., 1993, MNRAS, 267, 187

McDowell J.C., 1992, ApJ, 384, 62

McHardy I.M., Czerny B., 1987, Nat, 325, 696

McHardy I.M., 1988, M.S.A.It., 59, 239

McHardy I.M., 1989, in Hunt J., Battrick B. eds, Proc. of 23rd ESLAB Sypm., Two Topics in X-Ray Astronomy. ESA SP-296, p. 1111

McMaster W.H., 1961, Rev. Mod. Phys., 33, 8

Miller J.S., Goodrich R.W., 1990, ApJ, 355, 456

Miller J.S., Goodrich R.W., Mathews W.G., 1991, ApJ, 378, 47

Miller J.S., 1993, in "The Physics of Active Galactic Nuclei", Canberra, July 1993, in press

Mitsuda K., 1992, in Koyama K., Kunieda H. eds, Proc. of Conf., Frontiers of X–ray Astronomy. Universal Academy Press: Tokyo, p115

Monier R., Halpern J.P., 1987, ApJ, 315, L17

Morini M., 1986, ApJ, 307, 486

Morisawa K. et al., 1990, A&A, 236, 299

Morrison R., McCammon D., 1983, ApJ, 270, 119

Mulchaey J.S., Mushotzky R.F., Weaver K.A., 1992, ApJ, 390, L69

Mulchaey J.S. et al., 1993, ApJ, 414, 144

Mushotzky R.F., 1984, Adv.Sp.Res., 3, 157

Mushotzky R.F., Done C., Pounds K.A., 1993, ARA&A, 31, 717

Nagirner D.I., Poutanen J., 1994, Ast.Sp.Phys.Rev., 9, 1

Nandra K. et al., 1989, MNRAS, 236, 39P

Nandra K., Pounds K.A., Stewart G.C., 1990, MNRAS, 242, 660

Nandra K., 1991, PhD thesis, Leicester University, UK

Nandra K. et al., 1991, MNRAS, 248, 760

Nandra K., Pounds K.A., 1992, Nat, 359, 215

Nandra K. et al., 1993, MNRAS, 260, 504

Nandra K., Pounds K.A., 1994, MNRAS, 268, 405 (NP94)

Nishimura J., Mitsuda K., Itoh M., 1986, PASJ, 38, 819

Nolan P.L. et al. 1981, Nat, 293, 275

Padovani P., 1989, A&A, 209, 27

Padovani P., Rafanelli P., 1988, A&A, 205, 53

Perola G.C. et al., 1986, ApJ, 306, 508

Perola G.C., Piro L., 1994, A&A, 281, 7

Perotti F. et al., 1986, ApJ, 300, 297

Petschek H.E., 1964, AAS–NASA Symposium on the physics of solar flares, NASA Special Publ. No. 50, p.425

Philips K. C., Meszaros P., 1985, ApJ, 310, 284

Piro L., Yamauchi L., Matsuoka M., 1990, ApJ, 360, L35

Pogge R.W., 1989, ApJ, 345, 730

Pounds K.A., McHardy I.M., 1988, in Tanaka Y. eds, Proc. of Conf., Physics of Neutron Stars and Black Holes. Universal Academy Press: Tokyo, p.285

Pounds K.A. et al., 1989, MNRAS, 250, 769

Pounds K.A., Nandra K., Stewart G.C., George I.M., Fabian A.C. , 1990, Nat, 344, 132

Pounds K.A., Nandra K., Stewart G.C., 1992, in Brinkmann W., Truper J. eds, Proc. of Conf., X-Ray Emission from AGN and the Cosmic XRBG. MPE report 235: Garching, p. 1

Pounds K.A. et al., 1994, MNRAS, 267, 193

Poutanen J., 1994, PhD thesis, Helsinki University, Finland

Pozdnyakov L.A., Sobol' I.M., Sunyaev R.A., 1983, Ap. Space Sc. Rev., Vol. 2, p. 189

Priest E.R., Forbes T.G., 1986, J.Geophys.Res., 91, 5579

Pringle J.E., 1981, ARA&R, 19, 137

Pudritz R.E., 1981a, MNRAS, 195, 881

Pudritz R.E., 1981b, MNRAS, 195, 897

Pudritz R.E., Fahlman G.G., 1982, MNRAS, 198, 689

Ross R.R., Fabian A.C., Mineshige S., 1992, MNRAS, 258, 189

Ross R.R., Fabian A.C., 1992, MNRAS, 261, 74

Rybicki G.B., Lightman A.P., 1979, Radiative Processes in Astrophysics. Wiley, New York

Salotti L. et al., 1992, A&A, 253, 145

Setti G., Woltjer L., 1989, A&A, 224, L21

Shakura N.I., Sunyaev R.A., 1973, A&A, 24, 337

Shapiro S.L., Lightman A.P., Eardly D.M., 1976, ApJ, 204, 187

Smith D.A., Done C., Pounds K.A., 1993, MNRAS, 263, 54

Spitzer L., 1956, Physics of Fully Ionized Gases. Wiley, New York

Stella L., Rosner R., 1984, ApJ, 277, 312

Stepney S., 1983, MNRAS 202, 467

Sunyaev R.A., Titarchuk L.G., 1980, A&A, 86, 121

Sunyaev R.A., Titarchuk L.G., 1985, A&A, 142, 374

Sunyaev R.A., Trumper J., 1979, Nat, 279, 506

Sunyaev R.A. et al., 1991, Sov. Astron. Lett., 17, 409

Svensson R., 1982a, ApJ, 258, 321

Svensson R., 1982b, ApJ, 258, 335

Svensson R., 1983, ApJ, 270, 300

Svensson R., 1984, MNRAS, 209, 175

Svensson R., 1986, in Mihalas D. & Winkler K–H. eds, IAU Colloq. 89, Radiation Hydrodynamics in Stars and Compact Objects. Springer: New York, p325

Svensson R., 1987, MNRAS, 227, 403

Svensson R., 1992, in Brinkmann B., Trümper J., eds, X–Ray Emission from Active Galactic Nuclei and the Cosmic X–ray Background. (MPE report 235), p103

Svensson R., 1994, ApJS, 92, 585

Svensson R., Zdziarski A.A., 1994, ApJ, in press

Sviron R., Tsuruta S., 1993, ApJ, 402, 420

Tadhunter C., Tsvetanov Z., 1989, Nat, 341, 422

Tanaka Y., 1991, in Treves A. et al. eds, Proc. of Diagnostics in X–ray Sources. Springer–Verlag: Berlin, p80

Tanaka Y., 1993, in Active Galactic Nuclei across the Electromagnetic Spectrum, IAU Symposium 159, in press

Titarchuk L.A., 1994, ApJ, in press

Titarchuk L.A., Mastichiadis A., 1994, ApJ, in press

Tran H.D., Miller J.S., Kay L.E., 1992, ApJ, 397, 452

Turner T.J., Pounds K.A., 1989, MNRAS, 240, 833

Turner T.J. et al., 1990, ApJ 381, 85

Turner T.J., George, I.M., Mushotzky, R.F., 1993b, ApJ, 412, 72

Ueda Y., Ebisawa K., Done C., 1994, PASJ, 46, 107

Ubertini P., 1991, ApJ, 366, 544

Urry C.M. et al., 1989, in Hunt J., Battrick B. eds, Proc. of 23rd ESLAB Sypm., Two Topics in X-Ray Astronomy. ESA SP-296, p. 789

Vikhlinin A. et al., 1992a, IAU circ. No.5576

Vikhlinin A. et al., 1992b, IAU circ. No.5608

Walter R., Courvoisier T.J.-L., 1992, A&A, 258, 255

Walter R., Fink H.H., 1993, A&A, 274, 105

Walter R. et al., 1994, A&A, submitted

Wandel A., Mushotzky R.F., 1986, ApJ, 301, L61

Weaver K.A. et al., 1992, ApJ, 401, L11

White N.E., Fabian A.C., Mushotzky R.F., 1984, A&A, 133, L9

White T.R., Lightman A.P., Zdziarski A.A., 1989, ApJ, 331, 939

Williams O.R. et al., 1992, ApJ, 389, 157

Wilson A.S., 1992, in Duschl W.J., Wagner S.J. eds, Proc. of Conf., Physics of Active Galactic Nuclei. Springer–Verlag: Berlin, p. 307

Wilson A.S., Elvis M., Lawrence A., Bland–Hawthorn J. 1992, ApJ, 391, L75

Yakoob T., Warwick R.S., 1991, MNRAS, 248, 773

Yakoob T. et al., 1993, MNRAS, 262, 435

Zamorani G. et al., 1984, ApJ, 278, 28

Zdziarski A.A., 1985, ApJ, 289, 514 (Z85)

Zdziarski A.A. et al., 1990, ApJ, 363, L1

Zdziarski A.A., Lightman A.P., Maciolek–Niedzwiecki A., 1993, ApJ, 414, L93

Zdziarski A.A., Zycki P.T., Krolik J.H., 1993, ApJ, 414, L81

Zdziarski A.A. et al., 1994, MNRAS, in press